River mouth hydrodynamics: the role of the outlet geometry and transient tidal and river discharge conditions on the jet structure

Antonio Ruiz-Reina[1], Alejandro López-Ruiz[2], and Miguel Ortega-Sánchez[3]

[1]Departamento de Ingeniería Aeroespacial y Mecánica de Fluidos, Universidad de Sevilla
[2]Departamento de Ingeniería Aeroespacial y Mecánica de Fluidos, Universidad of Sevilla
[3]University of Granada

July 11, 2024

Abstract

The hydrodynamics of river mouths are the result of a complex interaction between river flow, tidal conditions and outlet geometry. This complex interaction of factors shapes the jet that flows onto the continental shelf and influences the dynamics of these areas. To gain insight into the response of the jet to different outlet and nearshore geometries and changing river discharge and tidal conditions, the hydrodynamics of idealised river mouths are simulated numerically. Compared to previous work, the model includes transient river discharge and tidal conditions and more realistic nearshore geometries. Comparison with classical jet theory indicates that the model adequately simulates jet hydrodynamics. The results show that both the outlet geometry and the transient river discharge and tidal conditions have a significant influence on the jet structure and evolution along the nearshore. For constant river discharge and water level conditions, the results indicate that the nearshore profile plays a key role in determining the expansion or contraction of the jet. The momentum balance shows that the jet behaviour is related to the momentum transport and the barotropic terms. In cases where the river discharge and tidal conditions are transient, the jet alternates between a structure with two velocity maxima at the edges or a single peak in the centre during the tidal cycle. This alternation occurs as a function of the time along the tidal phase and the time lag between the tidal conditions and the river hydrograph. The morphodynamic consequences of these two different jet structures are also discussed.

River mouth hydrodynamics: the role of the outlet geometry and transient tidal and river discharge conditions on the jet structure

Antonio Ruiz-Reina[1], Alejandro López-Ruiz[1], Miguel Ortega-Sánchez[2]

[1]Departamento de Ingeniería Aeroespacial y Mecánica de Fluidos, Universidad de Sevilla, Camino de los Descubrimientos s/n, 41092, Seville, Spain
[2]Andalusian Institute for Earth System Research, University of Granada, Avda. del Mediterráneo, s/n, 18006, Granada, Spain

Key Points:

- Different outlet dimensions and nearshore depth profiles are tested
- Jet contraction is obtained for non-horizontal nearshore profiles
- Jet structure determined by tidal conditions and outlet geometry

Corresponding author: Alejandro López-Ruiz, `alopez50@us.es`

Abstract

The hydrodynamics of river mouths are the result of a complex interaction between river flow, tidal conditions and outlet geometry. This complex interaction of factors shapes the jet that flows onto the continental shelf and influences the dynamics of these areas. To gain insight into the response of the jet to different outlet and nearshore geometries and changing river discharge and tidal conditions, the hydrodynamics of idealised river mouths are simulated numerically. Compared to previous work, the model includes transient river discharge and tidal conditions and more realistic nearshore geometries. Comparison with classical jet theory indicates that the model adequately simulates jet hydrodynamics. The results show that both the outlet geometry and the transient river discharge and tidal conditions have a significant influence on the jet structure and evolution along the nearshore. For constant river discharge and water level conditions, the results indicate that the nearshore profile plays a key role in determining the expansion or contraction of the jet. The momentum balance shows that the jet behaviour is related to the momentum transport and the barotropic terms. In cases where the river discharge and tidal conditions are transient, the jet alternates between a structure with two velocity maxima at the edges or a single peak in the centre during the tidal cycle. This alternation occurs as a function of the time along the tidal phase and the time lag between the tidal conditions and the river hydrograph. The morphodynamic consequences of these two different jet structures are also discussed.

Plain Language Summary

The dynamics of river mouths are determined by a very complex interaction between the hydrological characteristics of the basin, the shape of the mouth and continental shelf, and the tidal and other marine conditions. Although these dynamics have been extensively studied for very simple mouth geometries and constant river discharge in the absence of sea level variations, the role of both the geometric parameters of these systems and tidally driven temporal variations in discharge and sea level have not been systematically analysed. This manuscript analyses, using a process-based numerical model, the role played by all these factors in the structure of the jet stream generated at the river mouths. The focus is on small basin river mouths, where the temporal variations in river discharge have a duration similar to that of the tidal period. The results show that the jet structure is mainly determined by the geometry of the continental shelf. In addition, the tides play an important role, as the jet structure varies significantly during the tidal cycle. The morphodynamic implications of the results are also discussed throughout the manuscript.

1 Introduction

River mouths and deltas are areas of significant ecological and socio-economic interest, containing some of the world's most valuable ecosystems and densely populated areas (Lamb et al., 2012). This has led to the development of important industrial and agricultural areas, which often require inland waterways along the river courses that feed these mouths. The processes of transport and mixing of nutrients, salinity and sediments in these environments are of great importance for the biogeochemical evolution of many riverine and marine ecosystems, as well as for the formation of morphologies such as bars and deltas. The development of these features generally follows sediment deposition, which can occur through natural levee growth and channel elongation, or through deposition and vertical aggradation of estuarine bars (Fagherazzi et al., 2015). Furthermore, both river mouths and deltas are susceptible to extreme flooding events caused by river discharge, storm surge or a combination of both (Romero-Martín et al., 2024). The management of these extreme events is becoming increasingly challenging due to changes in their frequency and intensity caused by climate change (Fernandino et al., 2018). Consequently, improving knowledge of the dynamics of river mouths is of fundamental importance from both an environmental and socio-economic perspective.

The hydrodynamics of the river mouth is dominated by a confined turbulent jet that flows into a basin where waves, storm surges and astronomical tides can modify the shape and intensity with which this jet spreads laterally and reduces its seaward velocity. The geometry of the outlet and nearshore region also play a key role in the evolution of this jet, influencing both the flow structure at the outlet and the propagation velocity once it enters the shelf. Consequently, the interaction between hydrodynamics and sediment is a feedback process in which the jet structure determines the sediment deposition, which in turn determines the morphology with the formation of features such as bars, which are crucial for the development of deltas.

To characterise jet hydrodynamics, authors such as Abramovich and Schindel (1963) and Özsoy and Ünlüata (1982) developed time-averaged solutions of the integral jet theory, in which the jet structure is divided into two zones: (1) the zone of flow establishment (ZOFE) near the outlet, where the flow leaves the channel and expands abruptly; and (2) the zone of established flow (ZOEF) far from the outlet, where the flow is stable and similarity hypotheses can be applied (Ortega-Sánchez et al., 2008). From these pioneering works, this theory has been refined to describe a transition zone between the ZOFE and the ZOEF (Ortega-Sánchez et al., 2008), although in the last 15 years the focus has been on the use of process-based models to analyse the effects of jet hydrodynamics on bar development, analysing the effects of sediment size (Edmonds & Slingerland, 2007), levee formation (Rowland et al., 2010), human activities (Anthony et al., 2014; Fan et al., 2006; Besset et al., 2019), bed roughness (Canestrelli et al., 2014) or the presence of vegetation (Nardin et al., 2016; Lera et al., 2019).

In most of these works, simplified outlet geometries were defined using lower channel width-to-outlet depth ratios (Canestrelli et al., 2014). Furthermore, numerous studies have considered channels with no slope or very gentle slopes flowing into horizontal basins (Edmonds & Slingerland, 2007; Leonardi et al., 2015; Nardin et al., 2016). Jiménez-Robles et al. (2016) analysed the influence of shelf slope on jet hydrodynamics, defining the shelf as a surface with a constant slope. Their results show that this slope plays a very important role in the jet structure, and therefore in the formation of bars and their final geometry. Shortly afterwards, Jiménez-Robles and Ortega-Sánchez (2018) also analysed the role of the river-shelf orientation.

Regarding the main fluvial and marine drivers, most of these studies consider constant river discharge conditions and neglect the effect of astronomical tides, storm surges and waves. However, works such as Nardin and Fagherazzi (2012) and Nardin et al. (2013) have analysed the role of waves in the formation and evolution of estuarine bars, concluding that waves play an important role in the timing of bar evolution as well as in their final geometry. Leonardi et al. (2015) focused on the influence of tides in a simplified geometry with a horizontal bottom. They considered two scenarios: one with a constant river discharge (river-dominated) and the other with oscillating discharge (tidal-dominated). In both cases, the impact of the ebb/flood cycles in the channel was replicated. The results obtained show that in the river-dominated case the tide has a wave-like dispersive effect, whereas in the tide-dominated case the effect varies considerably depending on the tidal range and river discharge. More recently, Ruiz-Reina and López-Ruiz (2021) analysed the short-term evolution of the mouth bar during extreme river discharge events, focusing on the role of the phase difference between the peak discharge and the tidal level. In this case, an equilibrium beach profile was used for the nearshore geometry. Their results showed that this phase plays a key role in the final geometry of the river mouth bar developed during the discharge events. Nevertheless, the hydrodynamics and jet structure were not analysed, nor was the role of the outlet geometry.

This literature review suggests that the interactions between fluvial discharge and marine drivers are very complex, although they are crucial for the management of river mouths and deltas. Furthermore, despite all the recent advances described above, there are still important aspects to be analysed in order to describe the jet structure at outlets. In particular, the impact of more realistic geometries, both in terms of outlet dimensions and platform shape, on the hydrodynamics described for simpler geometries remains to be further explored. Additionally, the combined effect of the astronomical tide and the role of the time lag between tidal and flow conditions in short river discharge events (time scale similar to that of the tide) remains to be determined.

The main objective of this work is twofold: on the one hand, to analyse the effect of mouth characteristics (ratio of outlet depth to channel width) and nearshore geometry on the jet structure; on the other hand, to analyse the effect of tides and short fluvial discharge pulses on the jet geometry, where their phase difference with the astronomical tide can influence the jet hydrodynamics. To achieve this goal, a process-based numerical model will be used on idealised but realistic geometries, maintaining the channel and platform slopes, as well as the outlet shapes commonly observed in small river mouths with high seasonal variability and relatively high slopes due to their proximity to mountain ranges. This proximity, which limits the size of the hydrological basins, also causes the fluvial discharge pulses to be short and may have the same time scale as the astronomical tides (Ruiz-Reina et al., 2020; Ruiz-Reina, 2021; Ruiz-Reina & López-Ruiz, 2021). The manuscript is structured as follows: Section 2 outlines the theoretical basis of jet hydrodynamics and how it can be adapted to more complex but more realistic profiles (dynamic equilibrium profile). Section 3 describes the methodology used, while the results obtained are presented and discussed in Sections 4 and 5, respectively. Finally, the main conclusions are presented in section 6.

2 Theoretical framework

Jet theory has been used extensively in recent decades to describe the jet that develops when a river discharges into a still water basin, with fluvial forces dominating over marine forces (Wright, 1977). In particular, the dominant primary force is a combination of inertia and turbulent bed friction, i.e. a river discharges into a still body of water with the same density as the incoming river (Fagherazzi et al., 2015), and no buoyancy effects are considered. At river mouths, the flow can be described by the shallow water equations (Özsoy & Ünlüata, 1982; Leonardi et al., 2013) due to the larger ratio of channel width to outlet depth ($W/h_0 > 4$, see figure 1). The hydrodynamics of such a turbulent jet, also called a shallow bounded plane jet (Fagherazzi et al., 2015), can be divided into two zones: (1) a zone of flow establishment (ZOFE), in the vicinity of the outlet, characterised by a core of constant velocity and rapid momentum dissipation; and (2) the zone of established flow (ZOEF), where the entire jet is dominated by the turbulent eddies and the centreline velocity decreases with a Gaussian transverse distribution of the velocity profile (Özsoy & Ünlüata, 1982; Jirka & Giger, 1992).

Nevertheless, subsequent works (Ortega-Sánchez et al., 2008) contributed to this theory, incorporating an additional zone between the ZOFE and ZOEF regions, in order to explain that the transition between them requires a certain length to occur. Although it has not yet been subjected to a comprehensive research, this transitional zone appears to be primarily dependent on the friction and the longitudinal changes of the bathymetry and momentum balance. Therefore, based on the streamwise velocity and the jet structure, three theoretical regions can be considered: i) ZOFE, with constant velocity along the jet axis; ii) ZOT (zone of transition), with decreasing velocity along the centre line and iii) ZOEF, with a Gaussian transversal velocity distribution, which can be approximated with sufficient accuracy for the purposes of this work by the following expression (see figure 1 for the definition of the variables) (Giger et al., 1991), with

$A = -\ln(0.5) = 0.693$:

$$\frac{u(x,y)}{u_c(x)} = e^{-A\zeta^2} \tag{1}$$

Regarding the ZOFE and ZOEF regions, an extensive body of work has been developed for an integral plane jet theory assumed to be incompressible, stationary, depth-constant and frictionless (Jiménez-Robles et al., 2016). A more complex analysis was developed by Özsoy and Ünlüata (1982) for ebbing flows at microtidal inlets, incorporating the effects of bottom friction to analytically solve the depth-averaged equations of motion under the assumptions of quasi-steadiness and self-similarity. The equations of motion (mass and along channel momentum balance) for the jet are (Özsoy & Ünlüata, 1982):

$$\frac{\partial(hu)}{\partial x} + \frac{\partial(hv)}{\partial y} = 0 \tag{2}$$

$$\frac{\partial(hu^2)}{\partial x} + \frac{\partial(huv)}{\partial y} = -\frac{f}{8}u^2 + \frac{1}{\rho}\frac{F_{xy}}{\partial y} \tag{3}$$

where h is the water depth, u and v are the depth-averaged velocity components in the x and y directions (figure 1), ρ is the water density, F_{xy} is the depth-integrated turbulent shear stress, and f is the friction factor, which can be expressed as a function of the Chezy number ($f = 8g/C_z^2$). To solve equations 2 and 3 along the channel centreline ($y = 0$, figure 1) and obtain $u_c(x) = u(x,0)$, the velocity distribution $u(x,y)$ is assumed to be self-similar with respect to the normalised coordinate $\zeta = y/b(x)$, where $b(x)$ is the half-width of the jet, which facilitates the integration of the equations of motion. According to Abramovich and Schindel (1963), the velocity field is parameterised as follows, where $F(\zeta) = u(x,y)/u_c(x)$:

$$F(\zeta) = \begin{cases} 0 & 1 < \overline{\zeta} \\ \left(1 - \overline{\zeta}^{1.5}\right)^2 & 0 < \overline{\zeta} < 1; \quad \overline{\zeta} = \dfrac{\zeta - r/b}{1 - r/b} \\ 1 & \overline{\zeta} < 0 \end{cases} \tag{4}$$

where $r(x)$ is the core width which vanishes at $x = x_s$, the boundary between ZOFE and ZOEF. The integration of equations 2 and 3 is based on the assumption that $u(x,y)$ and F_{xy} decrease as y increases, but with consideration of a lateral entrainment velocity $v_e = v(x,y)|_{y\to\infty} = au_c$, where a is the entrainment coefficient. When the following normalised variables are introduced (Özsoy & Ünlüata, 1982):

$$\xi = \frac{x}{b_0}; \quad \mu = \frac{fb_0}{8h_0}; \quad H(\xi) = \frac{h}{h_0}; \quad R(\xi) = \frac{r}{b_0}; \quad B(\xi) = \frac{b}{b_0}; \quad U(\xi) = \frac{u_c}{u_0}; \tag{5}$$

two ordinary differential equations are obtained for both regions:

$$\frac{d}{d\xi}(I_1 HBU) = aHU \tag{6}$$

$$\frac{d}{d\xi}(I_2 HBU^2) = -\mu I_2 BU^2 \tag{7}$$

where b_0, h_0, and u_0 are respectively the half-width, depth and velocity at the outlet. The non-dimensional flow establishment distance is expressed as ξ_s.

From this point on, the analysis and subsequent comparisons are limited to the solution for the streamwise velocity along the axis in the ZOEF region. Consequently, the numerical constants I_1 and I_2 can be obtained as 0.450 and 0.316 (Özsoy & Ünlüata, 1982), respectively, after integrating $F^n(\xi)$ between 0 and 1 ($n = 1, 2$). The solution

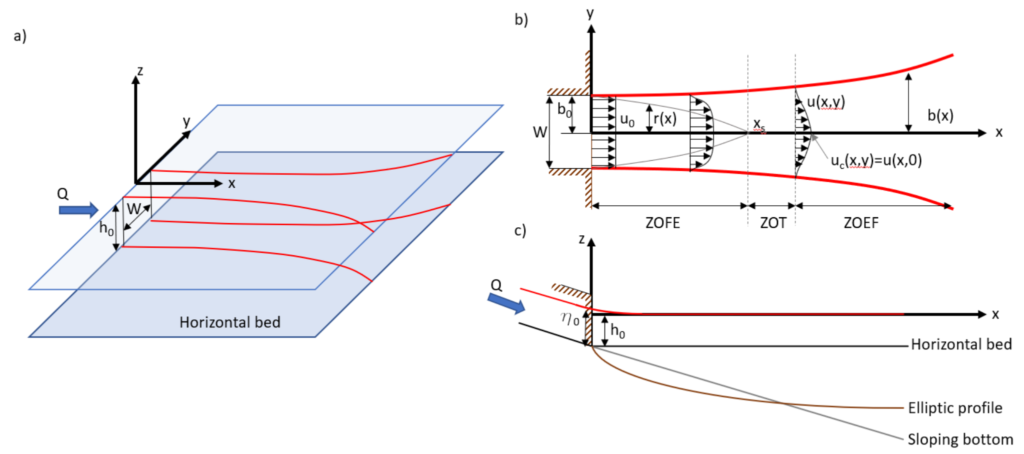

Figure 1. a) Definition sketch of a horizontal bounded jet. b) Zone of Flow Establishment (ZOFE), Zone of Established Flow (ZOEF) and Zone of Transition (ZOT). Q is the river discharge, h_0 is the outlet depth, η_0 is the water level at the outlet, W is the mouth width, b_0 is the mouth half-width, u_0 is the mean outlet velocity, $u_c(x)$ is the jet velocity along the axis, $u(x, y)$ is the streamwise velocity, $b(x)$ is the jet half-width, and x_s is the flow establishment distance. Panel c) shows the three considered nearshore profiles.

of the ODE system for this ZOEF region (equations 6 and 7), and hence the jet structure, is strongly dependent on the nearshore profile geometry $H(\xi)$. Previous works mainly analysed turbulent jet hydrodynamics for horizontal beds, where $H = 1$ (Edmonds & Slingerland, 2007; Nardin & Fagherazzi, 2012; Leonardi et al., 2015), or for sloping beds with constant slope m, where $H = 1 + \nu\xi$ and $\nu = mb_0/h_0$ (Jiménez-Robles et al., 2016). However, these are simplified geometries of the nearshore profile that in nature presents a variable slope with a cross-shore variations of the water depth that can be described by its equilibrium shape $h(x) = Ax^{2/3}$ (Dean & Dalrymple, 2004), where A is the profile scale factor, a dimensional parameter that mainly depends on the sediment size. This elliptical profile, after non-dimensionalisation, is expressed as $H = 1+k\xi^{2/3}$, where $k = Ab_0^{2/3}/h_0$. The solution of the ODE system for the ZOEF region using a finite difference scheme described in the Supporting Information is implemented to obtain u_c for the three geometries described above. These results are used to validate the simulations performed with the depth-averaged 2D hydrodynamic model for steady-state conditions (still water level and constant river discharge) shown in section 4.1.

3 Material and methods

3.1 Physical scenarios

The physical scenario in which the numerical model was implemented represents a straight channel flowing into a basin representing the continental shelf. To analyse the role of the mouth geometry on the jet structure, three parameters were varied: (1) the width of the channel W; (2) the depth of the channel at the outlet with respect to the mean sea level (hereafter MSL) h_0; and (3) the geometry of the continental shelf.

The channel geometry was defined with a rectangular cross section perpendicular to the shoreline orientation. This channel has a width of $W_i = (100, 200, 500)$ m and a longitudinal slope of $S_s = 0.002$. The lateral edges of the section are vertical walls with a height greater than 4 m at each section to prevent overtopping and to ensure mass conservation between the upstream boundary condition and the mouth. The depth of the outlet is h_{0i}=(1, 3) m. The length of the channel is 2.5 km, which ensures that the tidal excursion can be simulated correctly while avoiding the numerical effects of the upstream boundary condition (figure 2).

The shoreline is straight and the geometry of the beach profile was defined as (1) a horizontal bottom with depth h_{0i}; (2) a bottom with constant slope $S = 0.05$; and (3) a bottom with the equilibrium elliptical shape defined by Dean and Dalrymple (2004) (see Ruiz-Reina and López-Ruiz (2021) for further details). This elliptical shape is concave and therefore more realistic in the shallower part of the continental shelf. Finally, the platform is extended to the offshore boundary of the domain (figure 2) with maximum depths above 50 m. The combination of W_i, h_{0i} and platform geometries configures a set of 18 physical scenarios (see table 3.3).

3.2 Model description

The numerical model implemented to solve the hydrodynamics of the jet is Delft3D (Lesser et al., 2004), which is widely used to analyse the hydrodynamics of river mouths (Edmonds & Slingerland, 2007; Nardin & Fagherazzi, 2012; Nardin et al., 2013; Nienhuis et al., 2016; Boudet et al., 2017; van de Lageweg & Feldman, 2018; Gao et al., 2019). This model is capable of solving transient flows using the shallow water equations. In this case, buoyancy, ocean waves, Coriolis and wind effects are neglected using a depth-averaged version of the model in agreement with previous theoretical, experimental and numerical works (Lamb et al., 2012; Jiménez-Robles et al., 2016).

The model solves the shallow water equations for unsteady, incompressible, turbulent flow using a finite difference scheme. The continuity and horizontal momentum equations are:

$$\frac{\partial \eta}{\partial t} + \frac{\partial hu}{\partial x} + \frac{\partial hv}{\partial y} = S \tag{8}$$

$$\frac{\partial u}{\partial t} + u\frac{\partial u}{\partial x} + v\frac{\partial u}{\partial y} = -g\frac{\partial \eta}{\partial x} + M_x + g\frac{u\sqrt{u^2+v^2}}{C_{z,u}^2 h} + \epsilon_H\left(\frac{\partial^2 u}{\partial x^2} + \frac{\partial^2 u}{\partial y^2}\right) \tag{9}$$

$$\frac{\partial v}{\partial t} + u\frac{\partial v}{\partial x} + v\frac{\partial v}{\partial y} = -g\frac{\partial \eta}{\partial y} + M_y + g\frac{v\sqrt{u^2+v^2}}{C_{z,v}^2 h} + \epsilon_H\left(\frac{\partial^2 v}{\partial x^2} + \frac{\partial^2 v}{\partial y^2}\right) \tag{10}$$

where η is the water level with respect to MSL, t is time, S represents the sources/sinks of water, and g stands for the gravitational acceleration. $C_{f,u}$ and $C_{f,y}$ are the Chézy roughness coefficients in the x and y directions, respectively. The left-hand side terms in equations 9 and 10 represent the local acceleration and the advective (momentum transport) terms, whereas the first, second, third and fourth terms in the right-hand side represent the pressure gradient acceleration (barotropic), the external sources or sinks of momentum, friction and horizontal Reynolds stresses, respectively, where ϵ_H is the horizontal eddy viscosity. For a detailed description of the model the reader is referred to Lesser et al. (2004) and Ruiz-Reina and López-Ruiz (2021).

3.3 Model setup and numerical scenarios

The physical scenarios described in Section 3.1 were implemented using a regular grid of quadrangular cells aligned with the channel axis and the shoreline. To improve the efficiency of the simulations, the cell size varies from 100×100 m^2 at the offshore boundary to 10×10 m^2 at the outlet and the river channel. This grid was previously used by Ruiz-Reina and López-Ruiz (2021), where a sensitivity analysis was conducted

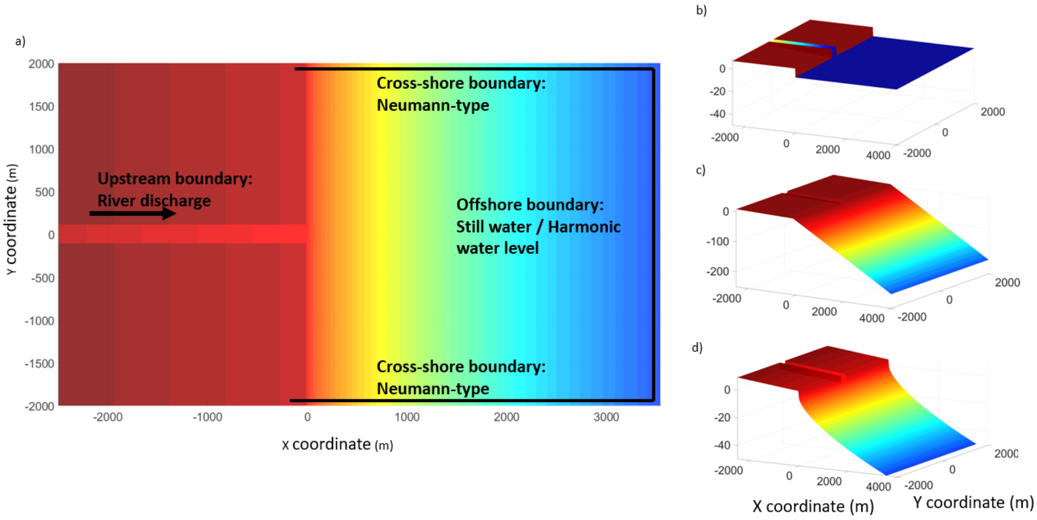

Figure 2. Physical scenarios: a) Plan view of the domain and boundary conditions used; and 3D plots including the bathymetry and the river channel for b) horizontal bottom, c) sloping bottom and d) elliptical profile.

to ascertain the optimal cell size. In order to meet the stability and accuracy requirements of the numerical scheme, a time step of 1.5 s was used. As in Ruiz-Reina and López-Ruiz (2021), constant coefficients were used for the bed roughness ($C_z = 55$) and the background horizontal eddy viscosity ($\epsilon_H^{back} = 1$ m^2/s) over the computational grid.

Three types of open boundaries were defined (figure 2): (1) the offshore boundary, with water level conditions; (2) the upstream boundary, located in the very upstream part of the channel, with river discharge conditions; and (3) two cross-shore boundaries, where Neumann-type conditions were used, imposing a zero water level gradient in the direction perpendicular to the boundary (Roelvink & Walstra, 2004).

Depending on the upstream and offshore boundary conditions, three types of simulations were defined. The first (Type 1, table 3.3) uses constant river discharge and no tides to analyse the role of the outlet and nearshore geometry in the jet structure under conditions equivalent to those used to define the plane-turbulent jet theory described in section 2. In this case, the offshore boundary condition is set to $\eta = 0$ throughout simulation. The river discharge is defined with a constant discharge rate per unit channel width $q = Q_i/W_i = 2.5$ m^2/s. As there are three values of W_i among the defined physical scenarios, three discharge values $Q_i = (250, 500, 1250)$ m^3/s were used. Keeping q constant allows the effect of channel geometry and W/h_0 ratio to be analysed without the results being affected by the different averaged velocities at the outlet section.

The second type of simulation (Type 2, table 3.3) is used to assess the impact of the tide and how it modifies the jet structure. In this case, the river discharge conditions are maintained, but at the offshore boundary the water level varies with the astronomical forcing defined by a single semi-diurnal harmonic with an amplitude of 1 m. Finally, in the third type of simulation (Type 3, table 3.3), the role of the river discharge pulses in the jet structure is analysed by defining different hydrographs at the upstream boundary, while at the offshore boundary the conditions defined for Type 2 simulations are maintained. The hydrographs were defined using the SCS (US Soil Conservation Service) method for the Chow et al. (1988) shape with a duration of 18 hours, corresponding to one and a half complete tidal cycles, and a peak discharge of $q_p = 2.5$ m^2/s. According to (Ruiz-

Type	Id	Profile	W (m)	h_0 (m)	Q_p (m^3/s)	Offshore	ϕ (rad)
1	111 121 151	Horizontal	100 200 500	1.0	250 (C) 500 (C) 1250 (C)	Still water	-
1	211 221 251	Sloping	100 200 500	1.0	250 (C) 500 (C) 1250 (C)	Still water	-
1	311 321 351	Elliptical	100 200 500	1.0	250 (C) 500 (C) 1250 (C)	Still water	-
1	113 123 153	Horizontal	100 200 500	3.0	250 (C) 500 (C) 1250 (C)	Still water	-
1	213 223 253	Sloping	100 200 500	3.0	250 (C) 500 (C) 1250 (C)	Still water	-
1	313 323 353	Elliptical	100 200 500	3.0	250 (C) 500 (C) 1250 (C)	Still water	-
2	221-T 321-T 223-T 323-T	Sloping Elliptical Sloping Elliptical	200	1.0 1.0 3.0 3.0	500 (C)	Tide	-
3	321-HT 321-ET 321-LT 321-FT	Elliptical	200	1.0	500 (hyd)	Tide	0 $\pi/2$ π $3\pi/2$

Table 1. Numerical scenarios: main characteristics. For the river discharge conditions, C means constant discharge whereas hyd means variable discharge (hydrograph)

Reina & López-Ruiz, 2021), the base time of the hydrographs was the same regardless of the peak discharge value. Furthermore, to analyse the importance of the phase between the peak discharge at the upstream boundary and the tide at the offshore boundary, the beginning of the hydrograph was defined at 4 different times, corresponding to the peak discharge at high tide, MSL to low tide (ebb tide), low tide and MSL to high tide (flood tide). The combination of such different boundary conditions and physical scenarios results in a total of 26 simulations (table 3.3). The total duration of each simulation is 48 hours, including an initial minimum spin-up interval of 24 hours to limit the effects of the prescribed still water initial conditions.

4 Results

4.1 Still water and constant discharge: analysis of the influence of outlet geometry and nearshore profile

4.1.1 Comparison to jet theory

The numerical modelling was validated by comparing its results in the ZOEF region with those obtained with the numerical solution of the Özsoy and Ünlüata (1982) equations (jet theory) for Type 1 simulations (Table 3.3), assuming entrainment coefficients similar to those used by Jiménez-Robles et al. (2016). A first examination of each simulation (figure 3) shows that the centreline velocity begins to decrease as soon as the jet enters the nearshore region. This observation is consistent with the results of Jiménez-Robles et al. (2016) and Nardin et al. (2013), who claimed that the ZOFE region can be neglected in such cases. Consequently, for each simulation, there exists an initial length of decreasing velocity and changing jet structure from the edges to the axis, which can be considered as an evidence of the existence of a transition region (ZOT).

The first row in figure 3 shows the results of the simulations performed with $h_0 =$ 1 m. For those with a horizontal bottom geometry, it can be observed that there is a poor fit between the model results and the values predicted by the jet theory, especially for larger widths (W). These differences may be due to the decrease in the predicted role of friction as W/h_0 increases. In fact, it has been found that by reducing the parameter μ (eq. 5) in the Özsoy and Ünlüata (1982) equations by a certain percentage (85%, 70%, 40% for $W = [100, 200, 500]$ m, respectively) both results converge.

In the case of sloping bottom simulations there are notable differences with respect to those with a horizontal bed. For cases with $h_0 = 1$ m, the velocity profile obtained with the numerical model has a local maximum at about $\xi = 2.0$, from which the velocities decrease, highlighting the development of the ZOT in the initial part of the jet as it enters the nearshore. This maximum is related to the length of transition required for the jet to fully develop as a consequence of the balance between jet contraction and its energy dissipation as it advances along the nearshore profile, as shown in the next section. This shape of the velocity profile is more pronounced for simulations with $W =$ $(200, 500)$ m, showing the influence of W on the jet structure in the ZOT region. In comparison with the jet theory solutions, a good fit can be observed from $\xi = 4.0$. The simulations with sloping bottom and $h_0 = 3$ m agree with these results, although in these cases the velocity profile is constantly decreasing for $W = 100$ m, while it shows a slight increase for $W = 200$ m, and for $W = 500$ m a relative maximum of the velocity is observed in the vicinity of $\xi = 1.5$.

The elliptical profile simulations show velocities very similar to the previous sloping bottom results, with a local maximum velocity observed at $\xi = 1.5-2.5$. The similarity of these results shows that the variable slope of the elliptical nearshore profile does not affect the shape of the velocity profile at distances close to the outlet. However, it can be observed that u_c/u_0 is higher for the elliptical profile simulations than for those with a sloping bottom.

Regarding the simulations with $h_0 = 3$ m and horizontal geometry, the μ parameter has to be reduced less in the theoretical results to obtain a good fit (about 80% for $W = 500$ m), highlighting a more relevant role of the bottom friction. On the other hand, for the sloping and elliptical bottom profiles the fit between the numerical models and the jet theory is particularly good from $\xi = 4.0-5.0$ offshore. Therefore, for the W/h_0 ratios for which the jet theory solution was developed, the numerical model satisfactorily reproduces the jet behaviour that has been extensively analysed in the literature (Abramovich & Schindel, 1963; Özsoy & Ünlüata, 1982; Jirka & Giger, 1992; Fagherazzi et al., 2015).

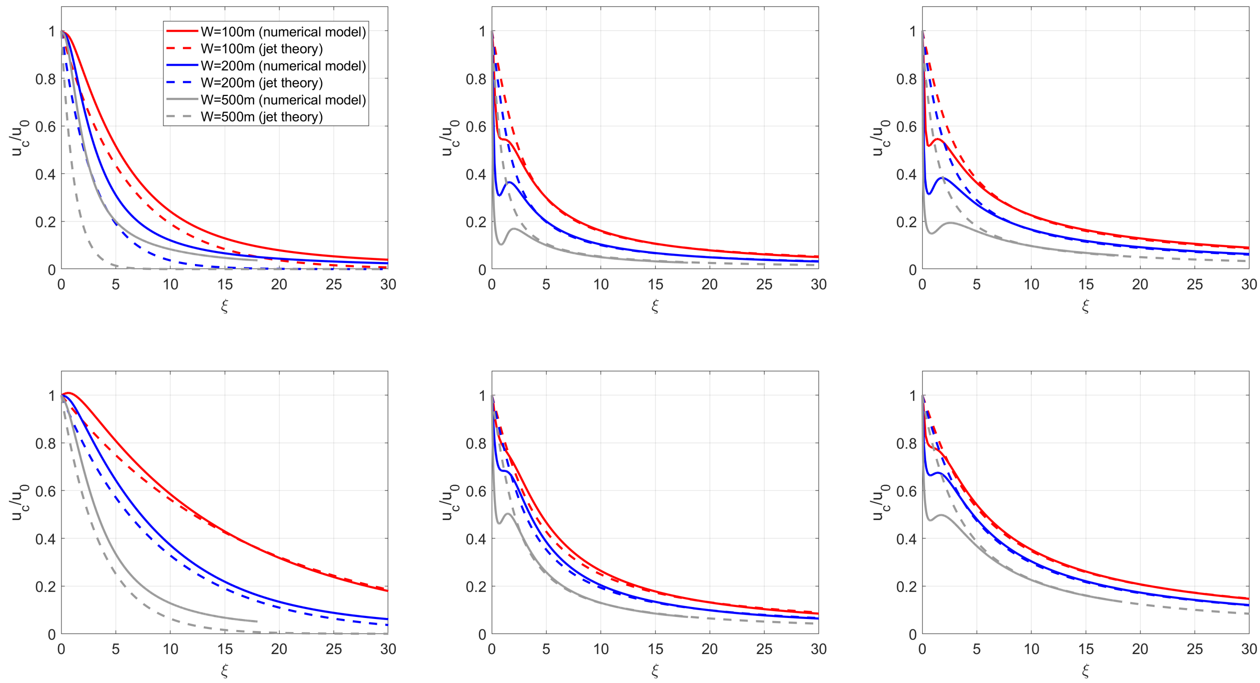

Figure 3. Velocity profiles obtained with the numerical model (solid line) and the jet theory (dashed line) for $h_0 = 1$ m (first row) and $h_0 = 3$ m (second row) and the horizontal, sloping and elliptical profiles (first, second and third columns, respectively). The X axis represents the non-dimensional distance to the outlet, whereas the Y axis represent the non-dimensional streamwise velocity.

Considering the above results, the numerical model is a valuable and reliable tool for the analysis of the jet structure and the hydrodynamics of the river mouth. However, its applicability goes beyond that of jet theory, as it can be extended to more complex and realistic geometries with higher W/h_0 ratios. Furthermore, the results presented in figure 3 show that the varying local maximum observed in the velocity profile is associated with the transition of the jet hydrodynamics to full development.

4.1.2 Streamwise velocity of the jet

Figure 4 illustrates the depth-averaged velocity contours in the vicinity of the outlet for the 18 numerical experiments with a constant river discharge (Type 1). In this figure, the distances from the outlet are not non-dimensional to show the velocity isolines in a more realistic way. The results show that the profile geometry controls the shape of the jet: while the horizontal bed shows an expanding jet throughout the domain with velocity contours extending away from the jet axis, the sloping and elliptical profiles show a jet that contracts near the outlet until it begins to expand at a certain distance. This phenomenon was already identified by Özsoy and Ünlüata (1982), who pointed out that with increasing depth the jet contracts due to mass conservation. The numerical results demonstrate the same behaviour for more complex geometries. Consequently, the impact of a nearshore environment with increasing depth is to suppress the expansion of the jet due to bottom friction, which becomes less dominant.

For $h_0 = 1$ m and horizontal bed the jet is wider because bottom friction dominates. In contrast, for $h_0 = 3$ m, the effect of bottom friction diminishes and the jet

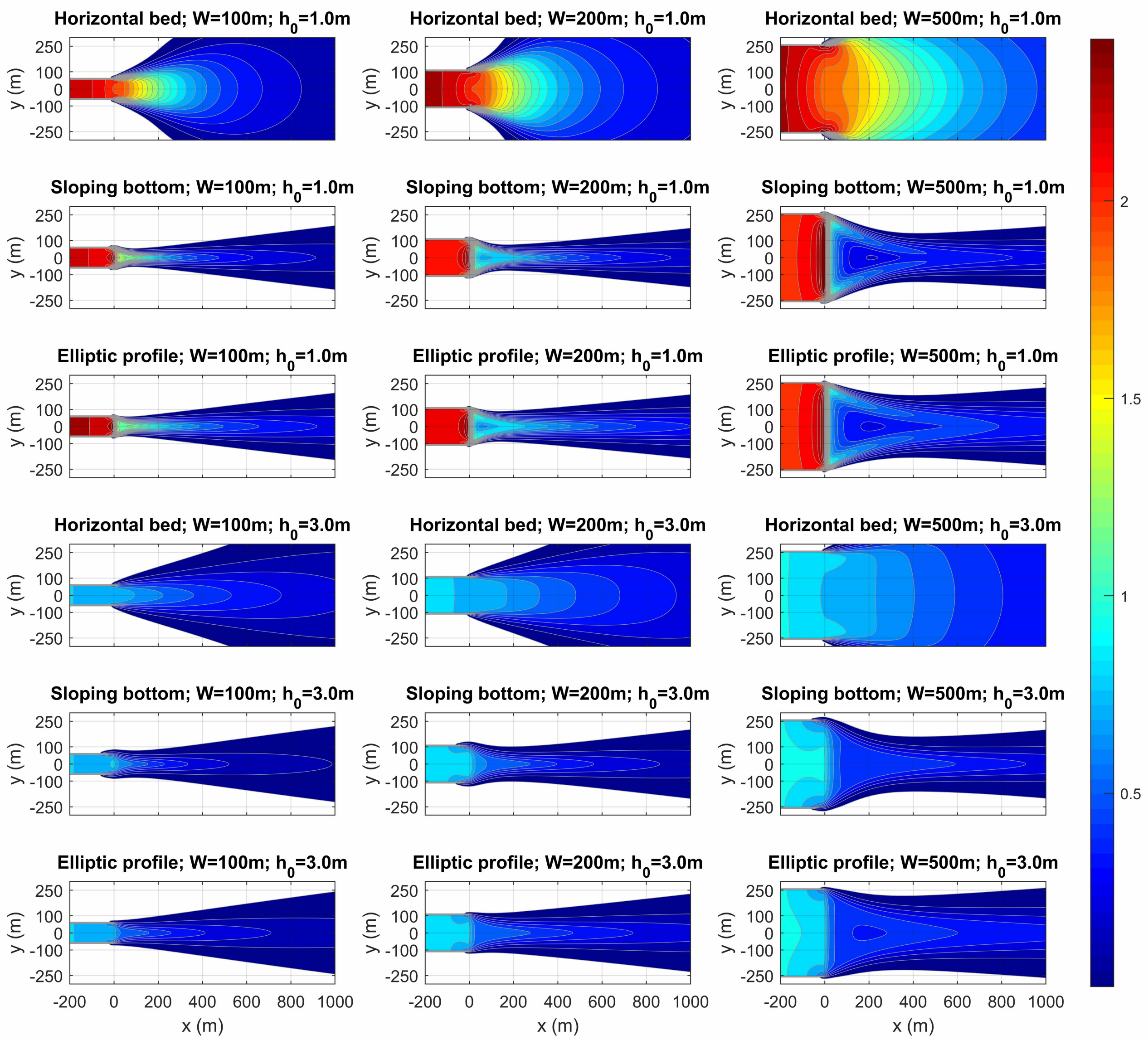

Figure 4. Streamwise velocity isolines for simulations with constant discharge and still water in the nearshore region (Type 1 in Table 3.3).

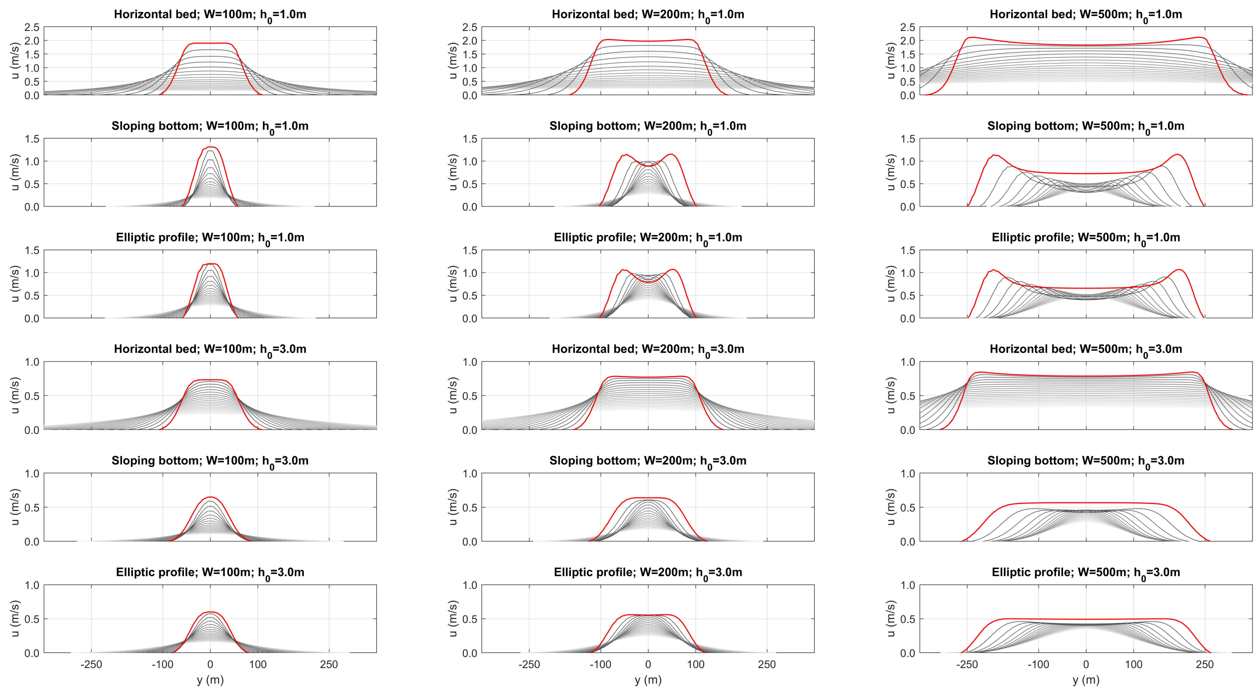

Figure 5. Transverse distribution of the streamwise velocity along the jet. In red, the velocity profile for a section located where the jet enters the nearshore area (x=50 m).

reduces its spreading. The jet contraction observed in simulations with sloping and elliptical profiles is comparable, but there are two key distinctions: i) the jet width is slightly higher in simulations with elliptical profiles, due to the lower slope of the bed profile from a certain distance from the mouth ($x = 100$ m); and ii) the distance over which the jet contraction extends also depends on the bed profile, but the influence of the mouth width is more pronounced. Figure 4 clearly shows that the contraction for a width of 500 m extends over a greater distance than those with smaller widths.

This phenomenon is also illustrated in figure 5, which shows the transverse distribution of the streamwise velocity through a series of cross sections. The maximum velocities for $h_0 = 1$ m are significantly higher (approximately twice) than for $h_0 = 3$ m. Furthermore, simulations with $h_0 = 1$ m and $W = (200, 500)$ m show a velocity profile with two peaks at the edges of the jet, regardless of the nearshore geometry. However, for $W = 100$ m, the velocity profile appears to show a single peak along the jet centre. For $h_0 = 3$ m, simulations with $W = (200, 500)$ m tend to have velocity profiles with a constant value at the top, decreasing towards the jet boundaries, consistent with the jet theory description in the ZOEF region. Simulations with a narrower width ($W = 100$ m) clearly show a velocity profile with a peak velocity along the jet centre. The similarity of the results for sloping and elliptical geometries can be attributed to the value of the longitudinal slope of the nearshore profile, as both profiles have a similar slope for the first 100 m. However, beyond this distance, the slope of the elliptical profile remains lower, implying a shallower bottom depth and leading to a smaller reduction in the streamwise velocity and a larger jet width at these distances.

These results show that W plays a significant role in determining the distance of flow establishment and hence the jet structure. Moreover, $\overline{u_0}$ also has a relevant influence and it is closely related to h_0, with lower values of h_0 associated with higher values of velocity. In particular, shallower outlets result in velocity profiles with two peak velocities along the edges of the jet, whereas deeper outlets are associated with velocity profiles with a single peak velocity along the jet axis.

4.1.3 Transverse component of the velocity

Figure 6 shows the non-dimensional transverse component of the velocity v/u_c at different sections where the flow is clearly established. The velocity trends observed in this figure are consistent with those described in Jiménez-Robles et al. (2016). For the horizontal bed cases, the velocity magnitudes are larger, with maxima in the region of $v/u_c = 0.5$. In contrast, for the sloping and elliptical profiles and $h_0 = 1$ m, v/u_c is below 0.1 at both cross sections.

Figure 6 also shows differences in the flow direction for the horizontal bed simulation on either side of the jet axis, so that the negative values are on the left and the positive values on the right. This sign criterion corresponds to a jet expanding with a transverse velocity that has its maximum at a point located at a distance equal to the half-width of the jet ($\zeta = 1$) for $h_0 = 1$ m and slightly closer the outlet for $h_0 = 3$ m. On the other hand, for the sloping and elliptical profiles, a change of sign is also observed in the velocities on either side of the jet, indicating a contracting jet. The two geometries show a remarkably similar magnitude and shape of the transverse velocity profile for simulations with $h_0 = 1$ m and $h_0 = 3$ m. The magnitude of the transverse velocity with respect to the streamwise velocity indicates that the jet is weakly contracting, resulting in no significant variation in its width. It should be noted that the parameter h_0 only has a relevant influence for geometries with a horizontal bottom.

The analysis of the transverse velocity shows that for sloping bottom geometries there is a value of slope for which the jet width is constant. As stated by Özsoy and Ünlüata (1982), the width of the jet depends, on the balance between the entrainment coefficient, μ and ν. Therefore, it depends, mainly, on the bottom roughness and geometry.

4.2 The effect of the tides

This section presents a detailed analysis of the influence of the tide on the jet velocity profile, employing Type 2 simulations. The analysis is limited to cases with $W = 200$ m, $Q = 500$ m^3/s and geometries corresponding to the sloping bottom and the elliptical profile (Table 3.3). The horizontal bottom profile was excluded from the analysis, as the tidal amplitude is similar to the water depth at the outlet.

Figure 7 shows the streamwise velocity contours at various stages throughout the tidal cycle. As with the results of the Type 1 simulations, the nearshore geometry plays a minor role in the velocity distribution. However, the final jet width is slightly larger for the simulations with an elliptical nearshore profile, which is a consequence of the shallower depth. Conversely, the initial depth of the water column, h_0, is a significant variable. Higher values of h_0 result in a lower mean exit velocity, $\overline{u_0}$, which favours the development of a jet with maximum velocity at the axis and a Gaussian transverse distribution. The tidal conditions emerge as a key factor that plays a significant role in the jet structure at the intratidal scale. Focusing on the simulations with $h_0 = 1$ m, for high tide conditions, maximum velocity values are observed at the outlet along the edges of the jet in sections close to the mouth, although there is a rapid evolution of the jet taking a maximum value along the axis. However, for low tide conditions, the existence of two local maximum velocities for the cross-channel profiles extends over longer distances along the jet path, which means that the development of the jet requires a longer distance, approximately twice as long as for high tide. For ebb and flood conditions, identical velocities are obtained and show a jet structure similar to that for low tide conditions. This means that a jet structure with two peak velocities along the edges is predominant during the tidal cycle for simulations with $h_0 = 1$ m. In contrast, the results

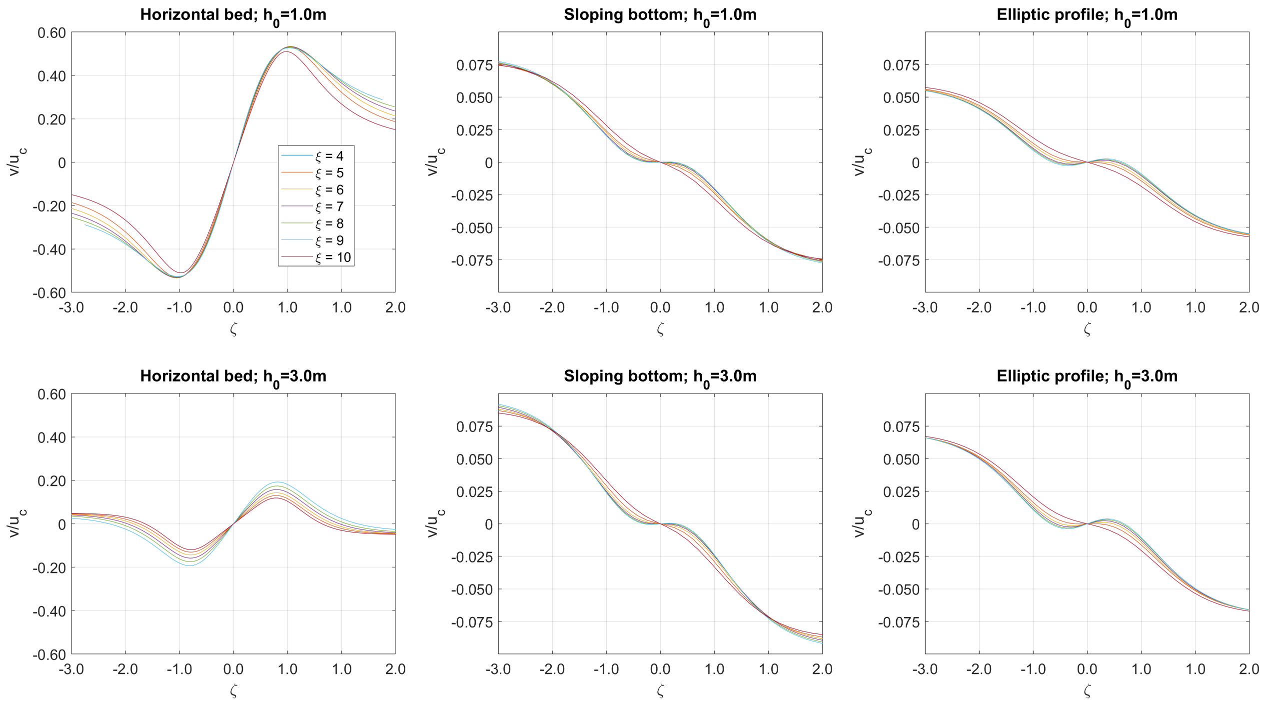

Figure 6. Non-dimensional Transverse component of the velocity at ξ =[4.0-10.0] for simulations with $W = 200$ m. The velocity is non-dimensionalized with the streamwise velocity along the axis, and the X-axis is non-dimensionalized with the half-width of the mouth width.

for $h_0 = 3$ m show a tendency towards a jet structure with a single peak velocity along the axis for the entire tidal cycle, with the exception of a short area around the mouth for low tide conditions. These results emphasise the key role of h_0 in the jet structure near the outlet.

The analysis of the evolution during a tidal cycle of the non-dimensional velocity along the axis is shown in figure 8. The velocity profiles for both nearshore profiles exhibit three distinct phases. First, there is a sharp decrease in velocity at a distance less than $\xi = 1$. Second, there is an increase in velocity and a maximum value located in a section at a distance $\xi = 1.5 - 2.0$. Third, there is a velocity decrease with decreasing ratio. Furthermore, there is a significant variation of the velocity with the tidal phase. For the cases with $h_0 = 1$ m, the maximum difference observed is $u_c/u_0 = 0.4$ at $\xi = 1.2$, which implies a variation of more than 100% between maximum and minimum values. This difference decreases further away from the outlet but maintains a value around $u_c/u_0 = 0.1$ at $\xi > 5$. Furthermore, in low tide conditions, a peak value exceeding $u_c/u_0 = 1.0$ is located downstream of the outlet, which significantly alters the predicted pattern in jet theory. This phenomenon is observed for both geometries, though it is more pronounced in the sloping case.

For $h_0 = 3$ m, lower variabilities are obtained. In addition, in this case the maximum velocity is located at the outlet; after the outlet the velocity decreases smoothly and the profiles are parallel to those of the non-tidal case. In these cases, the maximum difference $u_c/u_0 = 0.15$ is found at $\xi > 0.7$, which remains practically constant along the jet. These results show that the tide has an outstanding influence on the jet structure, with differences in u_c/u_0 above 100%. These differences, and hence the role of the tide, are particularly pronounced in shallow river mouths.

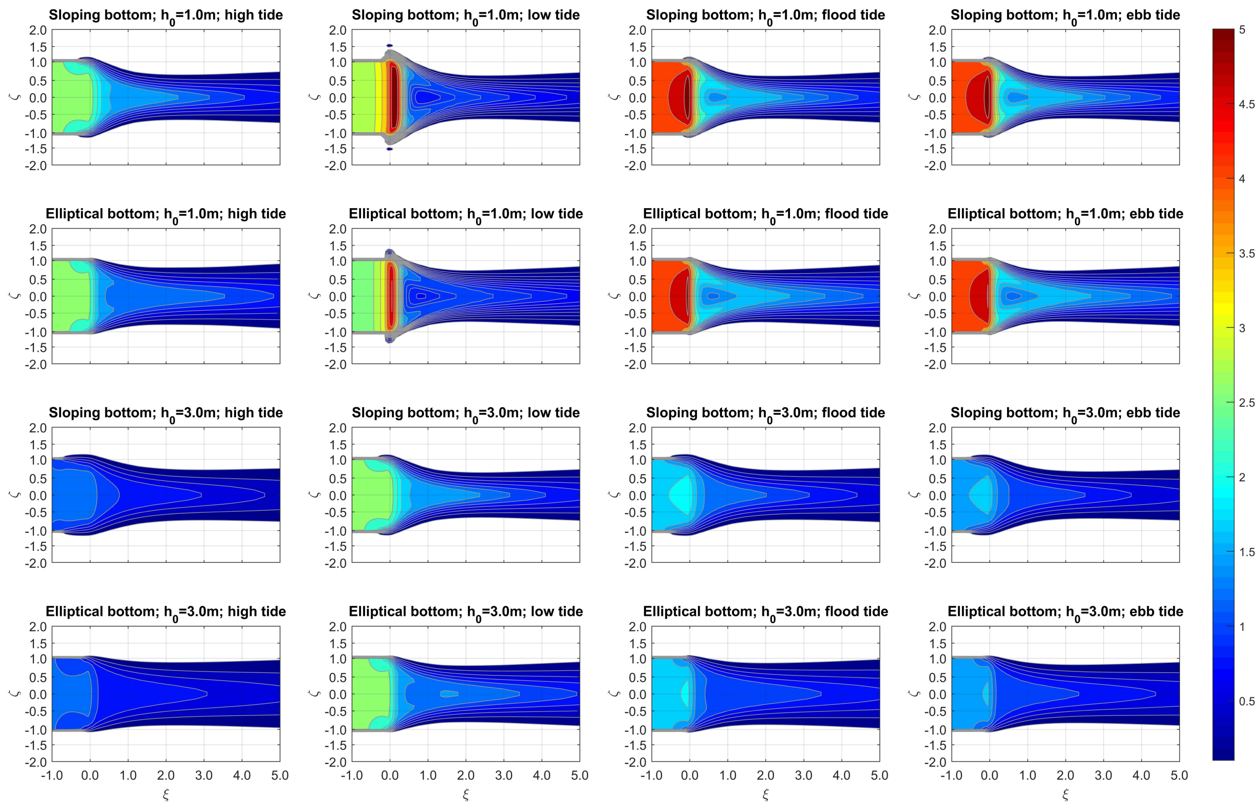

Figure 7. Streamwise velocity for Type 2 simulations at four instant during the tidal cycle: high, low, ebb and flood tide.

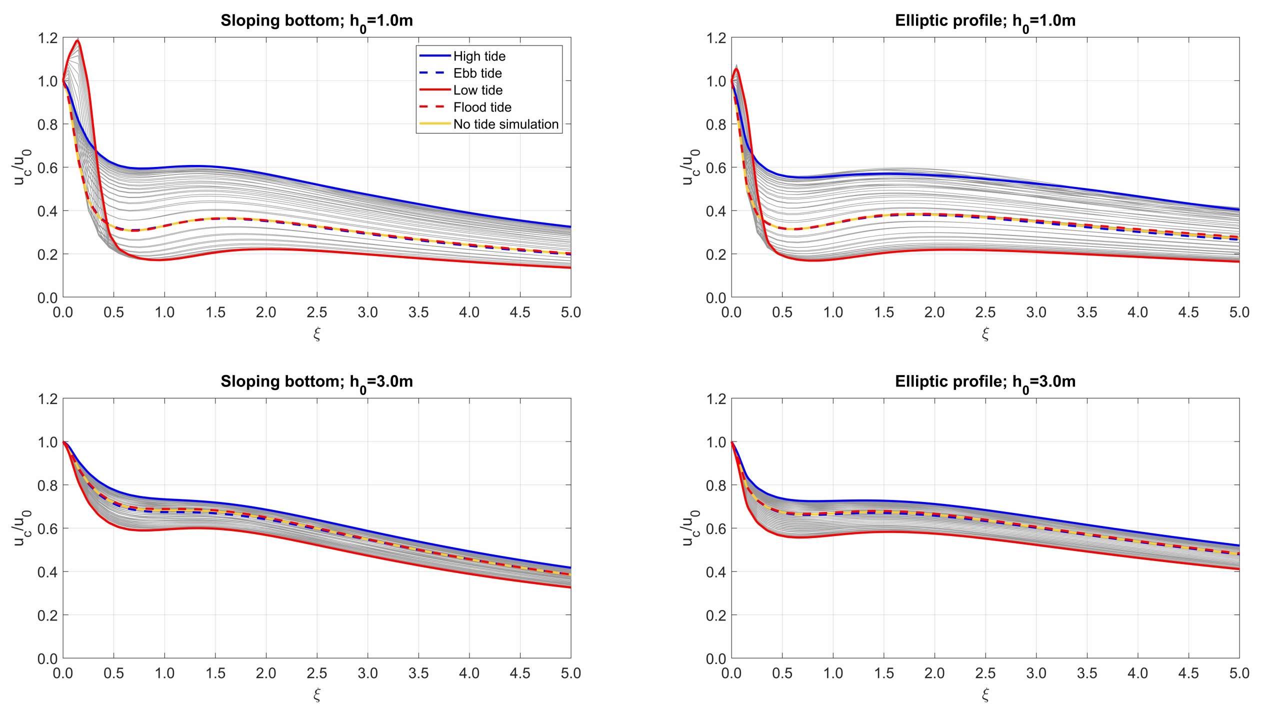

Figure 8. non-dimensional time evolution of the velocity profiles. Yellow line corresponds to the result with constant flow without sea level variation.

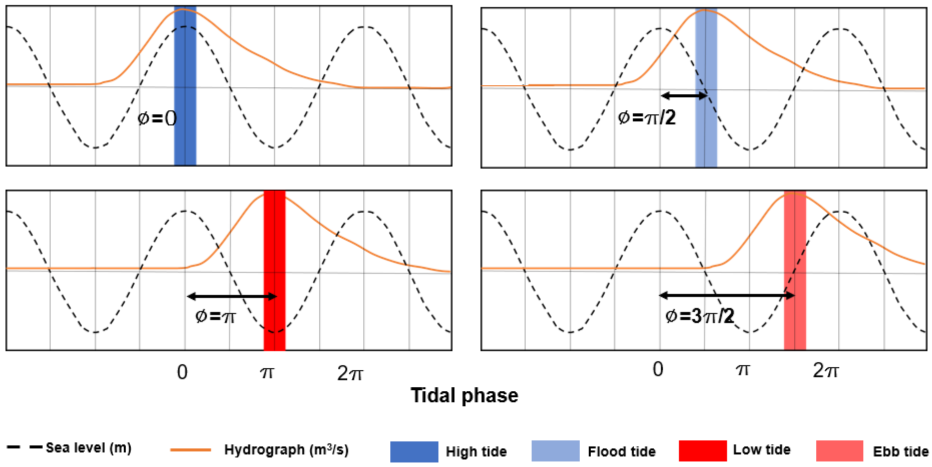

Figure 9. Definition sketch of the phase difference between the peak river discharge and the tidal level for the analysed simulations.

4.3 Transient river discharge: the role of the phase lag between the hydrograph and the tidal conditions

This section analyses the results of Type 3 simulations (table 3.3), where the geometry is restricted to the elliptical profile with $h_0 = 1$ m and $W = 200$ m. A hydrograph with a base time of 18 h and a peak discharge of 500 m^3/s is defined as the upstream boundary condition. Tidal conditions are maintained at the offshore boundary. These forcings introduce a new variable into the analysis of the jet structure: the time lag between the instant of peak discharge and high tide at the offshore boundary ϕ (figure 9). This delay is measured in terms of the phase of the tidal cycle. Analysis of the results showed that the time required for the tidal wave to propagate from the offshore boundary to the outlet is negligible.

The plan view structure of the jet during the peak discharge for the different values of ϕ is shown in figure 10. For $\phi = 0$, the jet contracts and shows a single peak velocity on the axis in close proximity to the outlet. Consequently, the velocity profile rapidly transitions to a transverse distribution with a single peak velocity on the axis. In contrast, for $\phi = \pi$, two maximum velocity peaks are clearly visible at the edges of the jet up to a distance of more than 100 m ($\xi = 0.5$). At a distance beyond this point, the velocity profile evolves to a single maximum on the axis.

These results are consistent with those presented in the previous section. At high water levels the velocity profiles show a single maximum in the centre. Conversely, in the context of low water levels, the velocity profiles show two maximum values at the edges, extending over a length of approximately $\xi = 1.0$. In the high water conditions, the water depth at the outlet (η_0) is greater, resulting in lower mean velocities at the outlet, as observed in the simulations with $h_0 = 3$ m.

To facilitate comparison with previous results, figure 11 shows the non-dimensional velocity profile along the axis. A significant variation can be observed between them, depending on the tidal conditions. When the hydrograph coincides with the high tide, η_0 is higher, leading to a lower value of the outlet velocity (u_0), resulting in velocity profiles similar to those of the jet theory, with a single maximum value at the jet axis. On the other hand, when the peak of the river discharge coincides with low tide conditions, it implies a lower depth (η_0), higher velocity at the outlet (u_0) and velocity profiles with

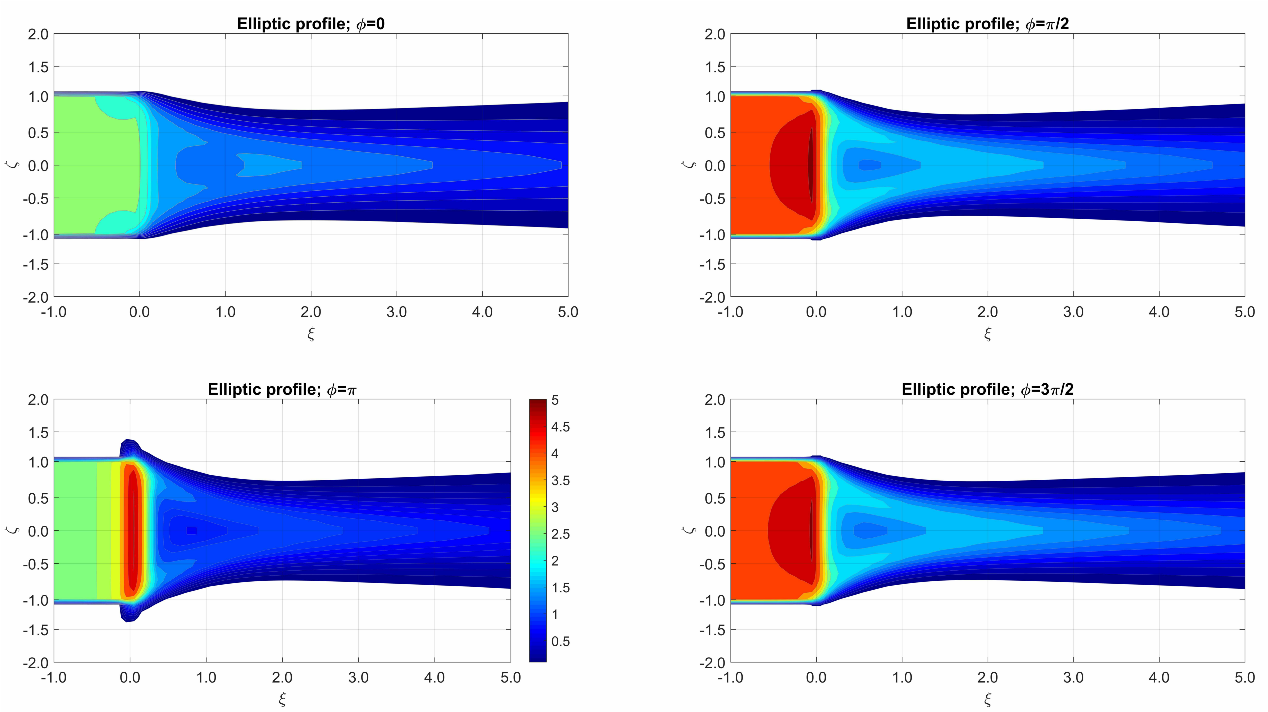

Figure 10. Streamwise velocity for $W = 200$ m, $h_0 = 1$ m, elliptical profile, and $\phi = [0, \pi/2, \pi, 3\pi/2]$ (coincidence between peak flow and high tide, low tide, ebb tide and flood tide conditions, respectively).

two peaks at the jet edges. It is also important to note that the maximum velocity is not at the outlet in every profile. In fact, it is slightly shifted towards the coast for $\phi = \pi$, especially at low tide. In these cases, the profiles are more similar to those with constant river discharge (figure 8), as they are associated with a higher velocity at the outlet. In addition, for $\phi = \pi$ there is also a second relative maximum at $\xi = 20 - 30$ associated with the advance of the river discharge.

The significant variation in the shape of the streamwise velocity profiles is also reflected in their cross-sectional distribution (figure 12). Velocity profiles with a Gaussian distribution are observed for instants corresponding to high tide, regardless of the value of ϕ, whereas two velocity peaks are observed at low tide. In contrast, there are notable differences between the velocity profiles corresponding to the simulations with hydrograph and tide compared to those with constant discharge and still water. The latter show a profile with two maximum velocity values, around 1.0 m/s. For the simulations with $\phi = 0$, all the profiles show velocity values lower than this value and none of them coincide with the case of constant discharge and still water. As for the simulations with $\phi = \pi$, the simulations with hydrograph and tide show greater similarity with those corresponding to constant discharge and still water, although a transverse distribution with more pronounced peak velocity values is observed.

5 Discussion

5.1 Boundaries defining the development of the jet

As mentioned above, jet theory describes the Zone of Flow Establishment (ZOFE) as the part of the jet where the centreline velocity remains constant until momentum dis-

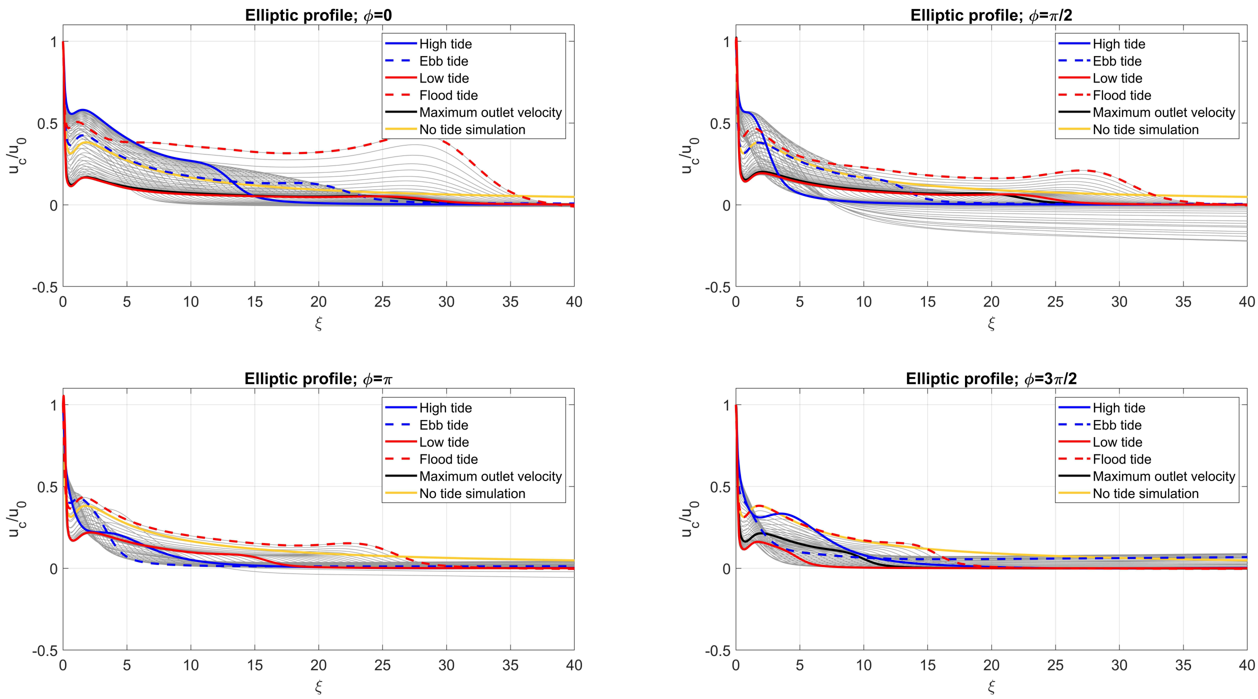

Figure 11. non-dimensional velocity along the axis during the entire tidal cycle ($\phi = [0, \pi/2, \pi, 3\pi/2]$; $W = 200m$; $h_0 = 1m$). Cases with $u_0 < 0.3$ m/s were omitted.

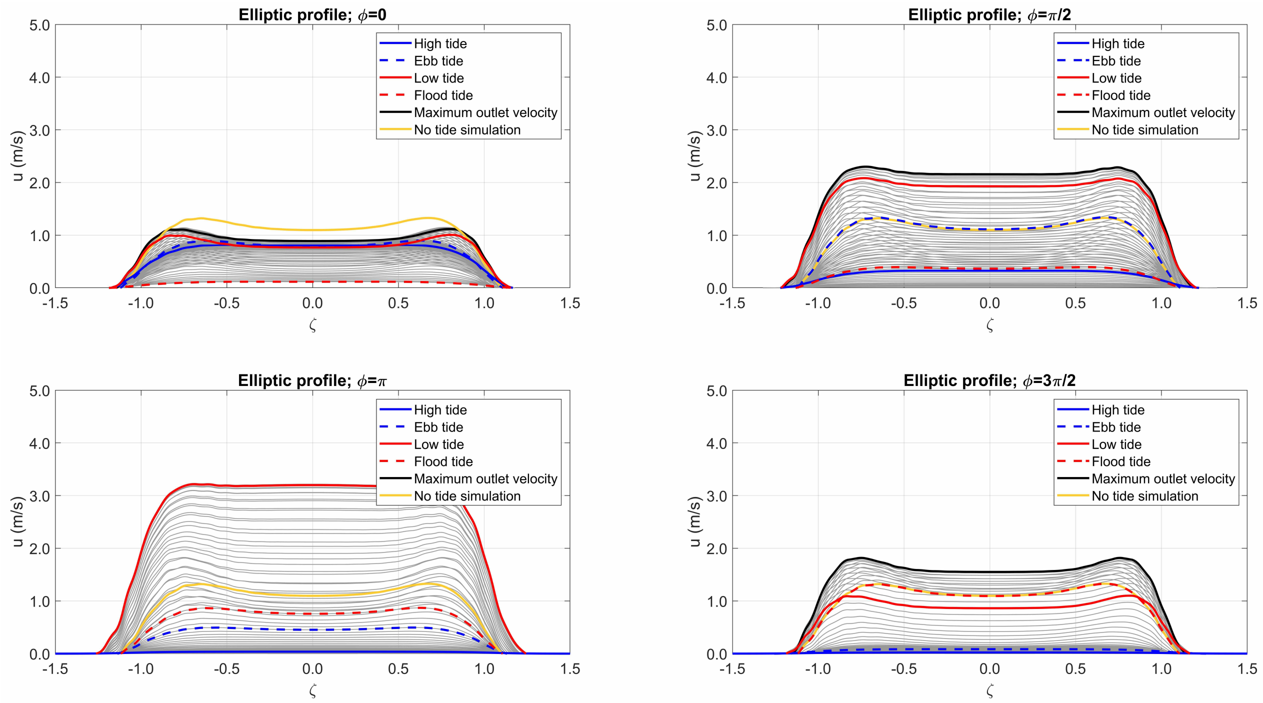

Figure 12. Cross-sectional distribution of velocities at 100 m from the outlet (ξ=0.5), located in the ZOFE region. Yellow line is added showing the result for the same geometry, corresponding to the simulation with constant discharge and still water. Black line corresponds to transverse velocity profile at the instant of maximum velocity at the outlet.

sipation and turbulence generated by edge shear reaches the entire jet (Fagherazzi et al., 2015). From this point on, the jet is dominated by turbulent eddies (Zone of Established Flow, ZOEF) and leads to a Gaussian transverse velocity distribution. According to previous works such as (Ortega-Sánchez et al., 2008), the transition from ZOFE to ZOEF does not occur at a fixed location, but take place within a transition region (ZOT) that depends on factors such as the geometry or the bottom friction. In this transition region, the velocity along the axis begins to decrease and the flow is not completely dominated by turbulence, resulting in an undefined transverse velocity profile with a clear maximum in the centre of the jet.

The analysis of the results presented in the previous section shows that the velocity along the axis does not have a constant value. Its value decreases as soon as it leaves the channel, except in certain scenarios where it is even observed to increase. It can therefore be concluded that the velocity structure of the jet at the outlet itself is in the ZOT region.

Conversely, while the theoretical structure described above is observed in some numerical experiments, the results indicate that a different jet structure can develop depending on the outlet and nearshore geometries. This structure exhibits two velocity peaks at the edge of the jet near the outlet. These two velocity peaks at the edges progress transversely towards the centre until they reach the axis, and from that point on the Gaussian profile is observed, as shown in figure 13. Therefore, the establishment of the flow is beyond this point of maximum velocity where the two peaks at the sides of the jet converge. In addition, these differences in the behaviour of the velocity distribution in the jet are amplified in the case of mouths with a greater width (W), a shallower depth at the outlet (h_0) and a sea profile different from a horizontal plane. In all these cases, the location of the relative maximum velocity along the axis was found between $\xi = 1.5$–2.5. Analogous results are observed when tides are set as the offshore boundary condition, and even when the river discharge is not constant. The velocity profile can be classified into two categories: the first category, which exhibits a single peak at the axis (related to high tide), and the second category, which exhibits two peaks at the jet edges (related to low tide). Therefore, the categorisation is dependent on the tidal conditions.

It is clear that different mouth geometries and hydrodynamic drivers lead to dissimilar jet velocity structures and turbulence progression from the edges to the jet axis, which also influences the location of the beginning of the ZOEF region. Figure 14 shows the results for the location of this initial section for the three types of simulations tested.

As summarised in Fagherazzi et al. (2015), previous works have found that for a plane unbounded jet this transition occurs at a distance of apprimately $\xi = [4.0-6.0]$. Therefore, the findings presented in this paper for horizontal geometries are in accordance with the literature, which demonstrates a considerable degree of variability for the location of the onset of the ZOEF region. The geometries analysed have a very high W/h_0 ratio, with a velocity profile influenced by the upstream section of the channel, which significantly affects the jet structure. This contrasts with the initial conditions of other studies, where the upstream section of the channel exerts a relatively minor effect on the jet structure.

Nevertheless, a comparable pattern of behaviour and tendency is observed in geometries with sloping bottoms and elliptical profiles (i.e. an increase in bottom depth along the axis). The wider mouths result in a further location of the ZOEF region in terms of non-dimensional distance, with all of them falling within the range of $\xi = [1.5-3.0]$. These distances are considerably smaller than those observed for plane unbounded jets.

Figure 14 also shows the results obtained for each time point during the tidal cycle for all simulations with constant river discharge. The parameter h_0 has a significant influence on the outcome. For $h_0 = 3$ m, the ZOEF region remains at the same distance

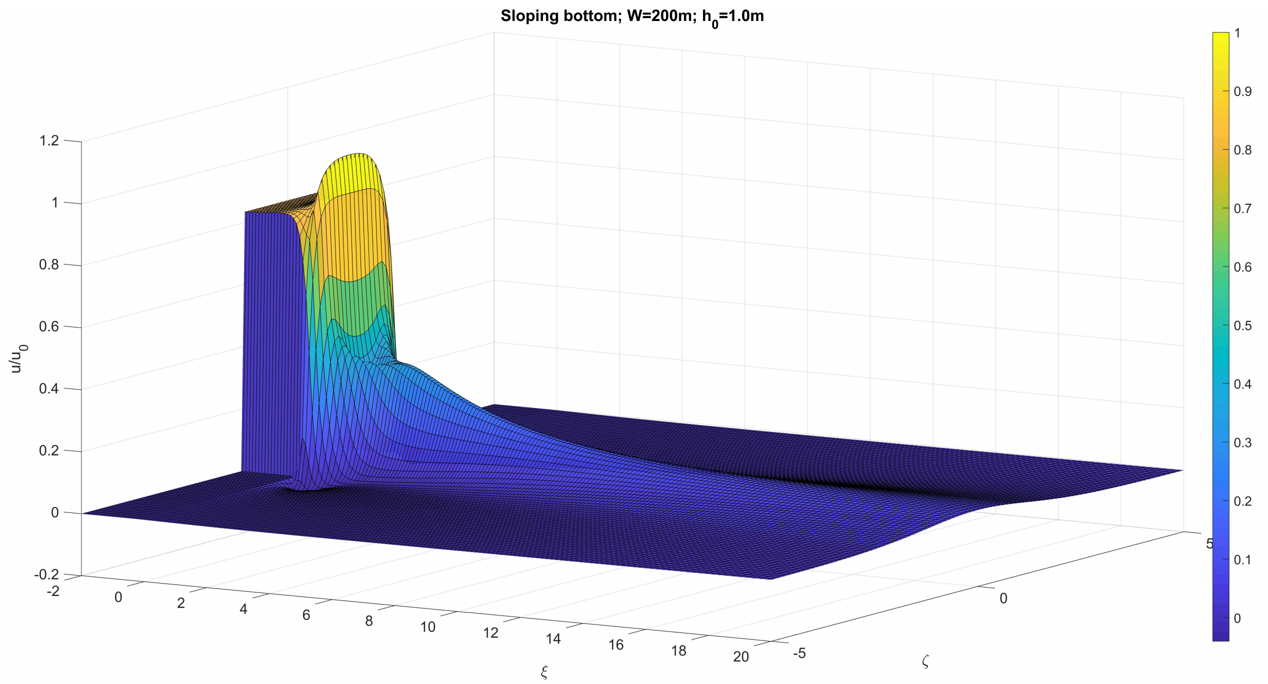

Figure 13. 3D view of the velocity distribution for the case of constant flow, W=200m, $h_0 = 1$ m, and sloping bottom profile. X-axis and Y-axis are non-dimensional distances related to the mouth half-width (b_0).

throughout the tidal cycle. However, for $h_0 = 1$ m, at low tide conditions, this distance is greater, particularly for the elliptical profile simulations. The location of the beginning is in the interval $\xi = [1.5{-}3.0]$. The results of the simulations with tides and transient river discharge demonstrate that at low tide conditions, the distance from the outlet where the ZOEF region is located increases. This phenomenon is more pronounced in the simulation with $\phi = \pi/2$ as this low tide coincides with the peak of the hydrograph. In the case of $\phi = 0$, two instants are observed in which the ZOEF region is located at a greater distance: the first corresponds to the peak of the hydrograph and the second to the low tide. As in the previous group of simulations, the distance for the beginning of the ZOEF region is within the interval $\xi = [1.5 - 3.0]$.

Consequently, the location of the beginning of the ZOEF region with non-horizontal geometries is located at a shorter distance from the outlet than in the cases with horizontal bottom. The reduction in the width of the mouth and the increase in the slope of the seabed in the nearshore area result in a shorter distance for the location of this transition. Conversely, a shallower outlet depth η_0 contributes to increasing this distance during a tidal cycle, with a maximum value observed during low tide conditions. Moreover, the transition and, consequently, the jet structure exhibit considerable variation throughout the tidal cycle, regardless of the outlet geometry.

5.2 Momentum balance and jet expansion/contraction

According to Wright (1977), the main depth-averaged processes that dominate the momentum balance in the spreading of river-dominated jets are: (i) inertia and momentum transport, (ii) turbulent bed friction, and (iii) acceleration due to water level variations (the barotropic term). The momentum balance for the simulations performed with constant discharge is in agreement with Wright (1977), showing that among the terms

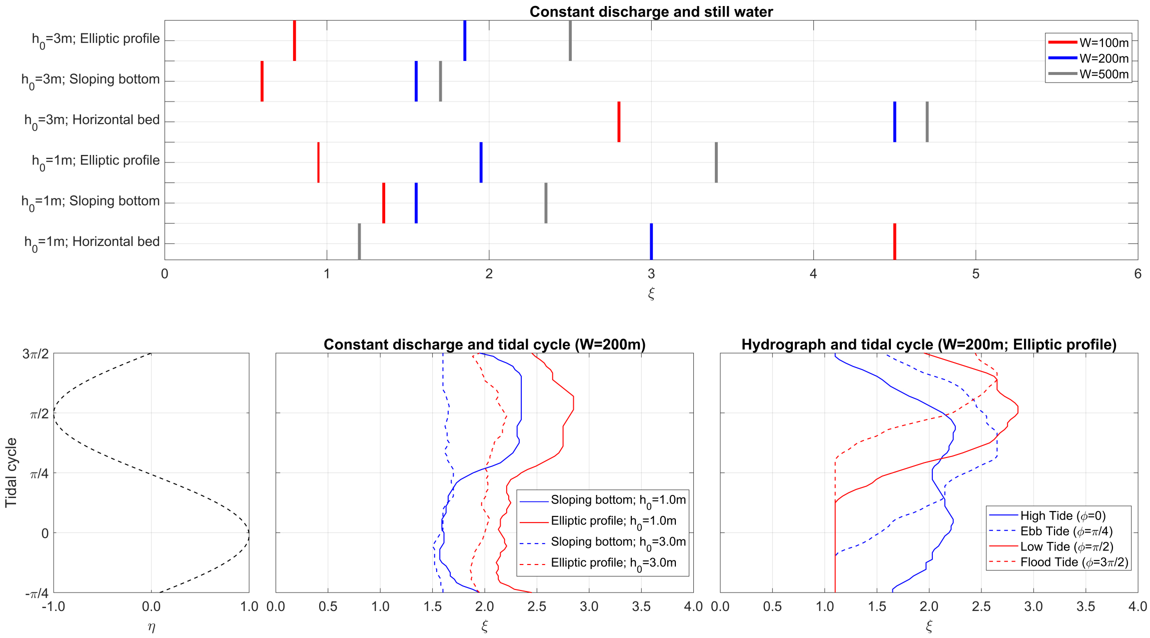

Figure 14. Analysis of the location of the onset of the ZOEF region for the three types of simulations. The top row shows a result for each simulation (Type 1) due to their independence of time. The lower row shows the results for simulations with tidal influence (Type 2 and 3). A plot of the water level in the sea region (η) during a tidal cycle is included to clarify the time at which each result is obtained. This location was determined from a comparison between the non-dimensional simulated streamwise velocity at each cross section and the ODE solutions deduced from the jet theory in the ZOEF region, ensuring that the difference between them in the interval $\zeta = [-1, 1]$ does not exceed 5%.

in equations 9 and 10, these three terms are at least one order of magnitude higher than any other. The following paragraphs are devoted to discussing the relationship between the balance of these terms and the structure of the jet.

The magnitudes of these three main momentum balance terms along the channel are illustrated in figure 15. In the vicinity of $\xi = 0$ (the outlet region), the results are similar for the sloping and elliptical profile geometries, while they show notable differences with the horizontal bed simulation. In the remaining portion of the axis, both within the canal and within the marine zone, the results tend to be similar for all geometries. With regard to the acceleration due to friction (negative values), it can be observed that its influence is limited to a reduced distance in the vicinity of the outlet for non-horizontal geometries. In contrast, it extends up to a distance of $\xi = 4.0$ ($x = 400$ m) for the geometry with a horizontal bed.

Along the flow axis, there is a balance between friction and hydrostatic pressure accelerations for each geometry. This is due to the regular and constant channel geometry, which corresponds to a uniform flow. Consequently, the acceleration due to inertial forces (momentum transport) is negligible. In the outlet area, this balance is disrupted, resulting in the emergence of significant accelerations, particularly those associated with hydrostatic pressure and inertial terms. There are notable differences in the magnitudes of these accelerations between the geometry with a horizontal bottom and those with sloping and elliptical profiles. In this region, the perturbation of the flow caused by the outfall propagates upstream as the flow is subcritical. In the nearshore area, the accelerations tend to decrease to a negligible value. The only exception to this is the acceleration due to friction for the horizontal bed geometry, which is observed to exert influence up to a distance of $\xi = 4.0$ ($x = 400$ m).

With regard to the accelerations resulting from hydrostatic pressure and momentum transport, a pronounced variation in the acceleration is concentrated in a region around the outlet in the interval $\xi = [-2.0, 1.0]$, particularly for geometries with sloping and elliptical profiles. It should be noted that the signs of the accelerations are different. Moreover, the values of these accelerations for the $h_0 = 1$ m cases are approximately one order of magnitude higher than those obtained for the $h_0 = 3$ m simulations. Consequently, for the horizontal bed geometries, friction plays a dominant role over a longer extent in the nearshore, promoting jet expansion, in a manner analogous to the friction-dominated flows described by Wright (1977). Conversely, in the case of variable bed level geometries, the barotropic and momentum transport terms exert a dominant influence on the momentum balance in the vicinity of the outlet, resulting in the contraction of the jet. At approximately $\xi = 1.0$, the balance between barotropic and momentum transport is no longer maintained, resulting in the cessation of jet contraction.

5.3 Jet structure and the development of lateral levees

The jet structure plays an important role in the morphodynamic evolution of river mouths and the development of bars, both at short-term (Ruiz-Reina & López-Ruiz, 2021) and long-term (Jiménez-Robles et al., 2016) scales. The changes in the initial bed geometry would, in a feedback process, alter the jet structure and, consequently, the hydrodynamics of the river mouth. Nevertheless, the findings presented in this work provide some insights that can be employed to establish links with morphodynamic analyses.

For instance, it was observed that the width of the mouth exerts a clear influence on the transverse profile of the flow velocity, which favours the formation of two peaks of maximum velocity at the edges. This phenomenon is more pronounced in cases where the bottom depth at the outlet is shallower ($h_0 = 1$ m). Both Ruiz-Reina and López-Ruiz (2021) and Jiménez-Robles et al. (2016) observed the formation of lateral levees parallel to the channel walls for river mouths with channel widths similar to those consid-

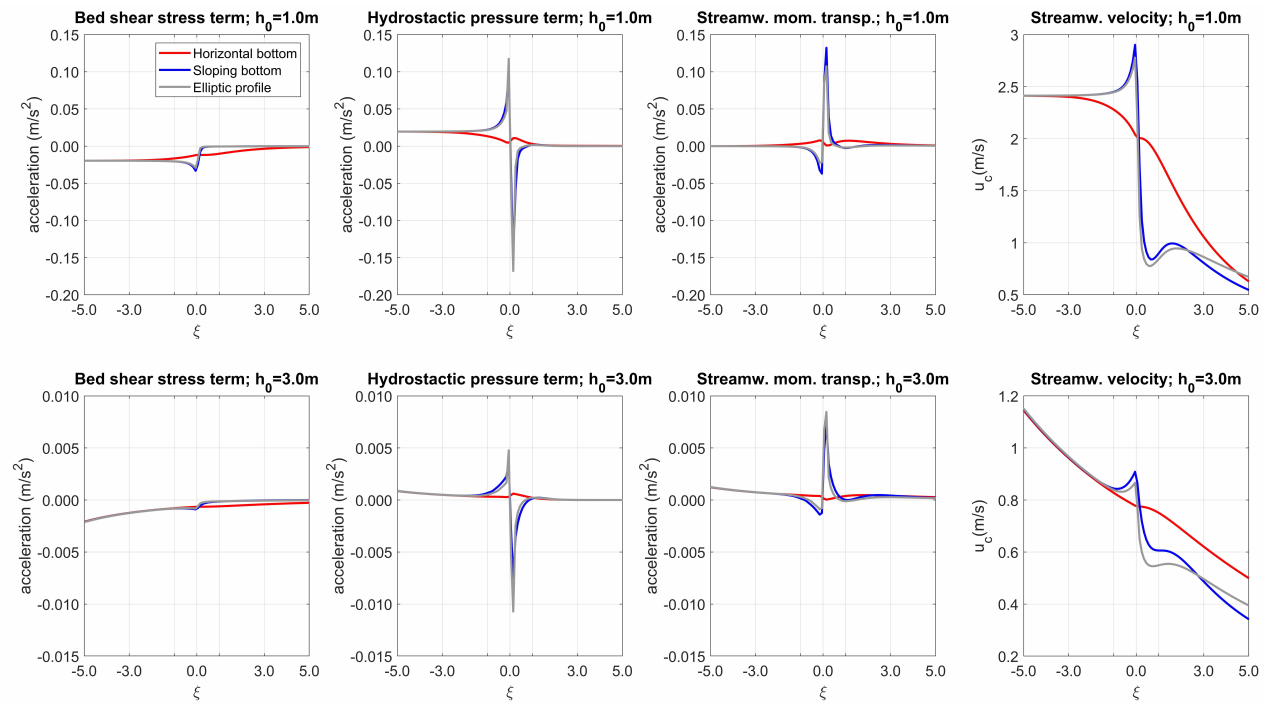

Figure 15. Results obtained for each of the momentum equation terms for the simulation with constant flow, $W = 200m$ and h_0=[1m,3m]: acceleration due to streamwise momentum transport, (inertial term) hydrostatic pressure and bed shear in bottom layer. Each line is associated with a geometry type.In the last column, the result for the streamwise velocity along the axis is added for a better understanding.

ered in this study. This morphodynamic evolution implies a lower bottom depth up to a certain point of the bar, after which a pronounced slope is formed where the levees do not develop. In the case of the simulations presented in the work by Ruiz-Reina and López-Ruiz (2021), the bottom depth reaches values below 2.0 m. On the other hand, the levees are more clearly shown in the simulations where the peak of the hydrograph coincides with the low tide, which implies a higher value of the velocity at the outlet, u_0, in agreement with the results obtained in the present work.

6 Conclusions

The objective of this study was twofold: (1) to analyse the role of mouth and nearshore geometries on the jet structure of river mouths; and (2) to assess the influence of tidal and river discharge conditions on this jet structure. The application of a process-based numerical model to idealised geometries defined with realistic parameters enabled the effect of mouth dimensions and nearshore profile shape to be analysed separately, and the role of river discharge and tidal conditions to be unravelled. The results of the numerical model for simplified geometries were compared with the jet theory solutions obtained by Abramovich and Schindel (1963); Özsoy and Ünlüata (1982), demonstrating that the model accurately reproduces the jet structure. This makes it a highly valuable tool for the analysis of more complex geometries and the effect of time-varying forcings.

Simulations with a constant river discharge and water level demonstrated that the outlet geometry determines the jet structure. In particular, outlets with shallower and wider cross-sections exhibited two velocity peaks at the edges of the jet, in contrast to the single maximum observed in the centre. In outlets where the nearshore profile is horizontal, the beginning of the ZOEF region is located at a greater distance from the outlet, and the jet expands after leaving the outlet. In contrast, for non-horizontal geometries, the jet initially contracts. Furthermore, the hydrodynamics at the mouth are evidently dominated by friction for this horizontal nearshore geometry. However, for sloping and elliptical profiles, the role of inertial and barotropic accelerations is significantly increased in the vicinity of the outlet.

It is observed that the changes in velocity during the tidal cycle may reach up to 100% between extreme values, while the variability of the jet structure during the tidal cycle is also significant when transient river discharges are included. This variability limits the applicability of the analyses carried out for stationary conditions in tidal environments or with a variable hydrological regime. This variability results in a significant variation in the location of the beginning of the ZOEF region. This is dependent on the time lag between the peak of the hydrograph and the tidal conditions. Moreover, the phase of the tidal cycle and the duration of the tidal cycle also determine the geometry of the transverse velocity profile. During low tide conditions, the distance from the outlet to the beginning of the ZOEF region increases, and the velocity profile tends towards a profile with two lateral velocity peaks. During high tide conditions, a shorter distance up to this beginning of the ZOEF region and a velocity profile with a single maximum on the axis is observed. This is consistent with the findings of previous studies on bar formation in analogous river mouths. The results achieved in this study enhance our comprehension of the jet structure in river mouths, providing insights into the complexity of the river-ocean interaction during extreme events and its impact on the morphodynamic evolution of river mouth bars and deltas.

Data availability statement

The model input files are available at the Zenodo repository: `https://zenodo.org/records/11546317`. Delft3D source codes are downloadable from the Deltares model repository (`https://oss.deltares.nl/web/delft3d`).

Acknowledgments

This work has been supported by the Spanish Ministry of Economy and Competitiveness. Grant PID2021-125895OA-I00 (project RESILIENCE) funded by MCIN/AEI/ 10.13039/501100011033 and by ERDF "A way of making Europe".

References

Abramovich, G., & Schindel, L. (1963). *The theory of turbulent jets.* MIT-Press.

Anthony, E. J., Marriner, N., & Morhange, C. (2014). Human influence and the changing geomorphology of Mediterranean deltas and coasts over the last 6000 years: From progradation to destruction phase? *Earth-Science Reviews*, *139*, 336–361. doi: 10.1016/j.earscirev.2014.10.003

Besset, M., Anthony, E. J., & Bouchette, F. (2019). Multi-decadal variations in delta shorelines and their relationship to river sediment supply: An assessment and review. *Earth-Science Reviews*, *193*(March), 199–219. doi: 10.1016/j.earscirev.2019.04.018

Boudet, L., Sabatier, F., & Radakovitch, O. (2017). Modelling of sediment transport pattern in the mouth of the Rhone delta: Role of storm and flood events. *Estuarine, Coastal and Shelf Science*, *198*, 568–582. doi: 10.1016/j.ecss.2016.10.004

Canestrelli, A., Nardin, W., Edmonds, D., Fagherazzi, S., & Slingerland, R. (2014, dec). Importance of frictional effects and jet instability on the morphodynamics of river mouth bars and levees. *Journal of Geophysical Research: Oceans*, *119*(1), 509–522.

Chow, V. T., Maidment, D., & Mays, L. (1988). *Applied hydrology.* McGraw-Hill.

Dean, R., & Dalrymple, R. (2004). *Coastal processes with engineering applications.* Cambridge University Press.

Edmonds, D. A., & Slingerland, R. L. (2007, jun). Mechanics of river mouth bar formation: Implications for the morphodynamics of delta distributary networks. *Journal of Geophysical Research*, *112*(F2), F02034. doi: 10.1029/2006JF000574

Fagherazzi, S., Edmonds, D. A., Nardin, W., Leonardi, N., Canestrelli, A., Falcini, F., … Slingerland, R. L. (2015). Dynamics of river mouth deposits. *Reviews of Geophysics*, *53*, 642-672. doi: 10.1002/2014RG000451

Fan, H., Huang, H., Zeng, T. Q., & Wang, K. (2006). River mouth bar formation, riverbed aggradation and channel migration in the modern Huanghe (Yellow) River delta, China. *Geomorphology*, *74*(1), 124-136. Retrieved from `https://www.sciencedirect.com/science/article/pii/S0169555X0500293X` doi: https://doi.org/10.1016/j.geomorph.2005.08.015

Fernandino, G., Elliff, C. I., & Silva, I. R. (2018). Ecosystem-based management of coastal zones in face of climate change impacts: Challenges and inequalities. *Journal of Environmental Management*, *215*, 32–39. Retrieved from `https://doi.org/10.1016/j.jenvman.2018.03.034` doi: 10.1016/j.jenvman.2018.03.034

Gao, W., Shao, D., Wang, Z. B., Nardin, W., Rajput, P., Yang, W., … Cui, B. (2019). Long-term Cumulative Effects of Intra-annual Variability of Unsteady River Discharge on the Progradation of Delta Lobes: A Modeling Perspective. *Journal of Geophysical Research: Earth Surface*, 1–14. doi: 10.1029/2017JF004584

Giger, M., Dracos, T., & Jirka, G. H. (1991). Entraînement et mélange dans des jets plans turbulents en faible profondeur d'eau. *Journal of Hydraulic Research*, *29*, 615-642. doi: 10.1080/00221689109498980

Jiménez-Robles, A. M., & Ortega-Sánchez, M. (2018). Implications of River Discharge Angle and Basin Slope on Mouth Bar Morphology and Discharge Dynamics of Stable Jets. *Journal of Hydraulic Engineering*, *144*(9), 1–9. doi:

10.1061/(ASCE)HY.1943-7900.0001506
Jiménez-Robles, A. M., Ortega-Sánchez, M., & Losada, M. A. (2016). Effects of basin bottom slope on jet hydrodynamics and river mouth bar formation. *Journal of Geophysical Research: Earth Surface*, *121*(6), 1110–1133. doi: 10.1002/2016JF003871
Jirka, G. H., & Giger, M. (1992). Plane turbulent jets in a bounded fluid layer. *Journal of Fluid Mechanics*, *241*, 587-614. doi: 10.1017/S0022112092002167
Lamb, M. P., Nittrouer, J. A., Mohrig, D., & Shaw, J. (2012). Backwater and river plume controls on scour upstream of river mouths: Implications for fluvio-deltaic morphodynamics. *Journal of Geophysical Research: Earth Surface*, *117*(1), 1–16.
Leonardi, N., Canestrelli, A., Sun, T., & Fagherazzi, S. (2013). Effect of tides on mouth bar morphology and hydrodynamics. *Journal of Geophysical Research: Oceans*, *118*, 4169-4183. doi: 10.1002/jgrc.20302
Leonardi, N., Kolker, A. S., & Fagherazzi, S. (2015). Interplay between river discharge and tides in a delta distributary. *Advances in Water Resources*, *80*, 69–78. doi: 10.1016/j.advwatres.2015.03.005
Lera, S., Nardin, W., Sanford, L., Palinkas, C., & Guercio, R. (2019). The impact of submersed aquatic vegetation on the development of river mouth bars. *Earth Surface Processes and Landforms*, *1506*(February), 1494–1506. doi: 10.1002/esp.4585
Lesser, G., Roelvink, J., Van Kester, J., & Stelling, G. (2004, October). Development and validation of a three-dimensional morphological model. *Coastal Engineering*, *51*(8-9), 883–915.
Nardin, W., Edmonds, D. A., & Fagherazzi, S. (2016). Influence of vegetation on spatial patterns of sediment deposition in deltaic islands during flood. *Advances in Water Resources*, *93*, 236–248. doi: 10.1016/j.advwatres.2016.01.001
Nardin, W., & Fagherazzi, S. (2012). The effect of wind waves on the development of river mouth bars. *Geophysical Research Letters*, *39*(12), 1–6.
Nardin, W., Mariotti, G., Edmonds, D. A., Guercio, R., & Fagherazzi, S. (2013, jun). Growth of river mouth bars in sheltered bays in the presence of frontal waves. *Journal of Geophysical Research: Earth Surface*, *118*(2), 872–886.
Nienhuis, J. H., Ashton, A. D., Nardin, W., Fagherazzi, S., & Giosan, L. (2016). Alongshore sediment bypassing as a control on river mouth morphodynamics. *Journal of Geophical Research: Earth Surface*, *121*, 664–683.
Ortega-Sánchez, M., Losada, M. A. A., & Baquerizo, A. (2008). A global model of a tidal jet including the effects of friction and bottom slope. *Journal of Hydraulic Research*, *46*, 80-86.
Özsoy, E., & Ünlüata, Ü. (1982). Ebb-tidal flow characteristics near inlets. *Estuarine, Coastal and Shelf Science*, *14*(3). doi: 10.1016/S0302-3524(82)80015-7
Roelvink, D., & Walstra, D.-J. (2004). Keeping It Simple By Using Complex Models. *Advances in Hydro-Science and Engineering*, *VI*(August), 1–11.
Romero-Martín, R., Caballero-Leiva, I., Llasat, M. C., Llasat-Botija, M., Rigo, T., Valdemoro, H. I., … Jiménez, J. A. (2024, 12). Mapping cumulative compound hydrometeorological and marine-induced risks on the nw mediterranean coast. *Scientific Reports*, *14*. doi: 10.1038/s41598-024-53899-z
Rowland, J. C., Dietrich, W. E., & Stacey, M. T. (2010). Morphodynamics of subaqueous levee formation: Insights into river mouth morphologies arising from experiments. *Journal of Geophysical Research: Earth Surface*, *115*(4), 1–20. doi: 10.1029/2010JF001684
Ruiz-Reina, A. (2021, February). *River mouth data from major streams in southern Spain.* https://doi.org/10.5281/zenodo.4541878. Zenodo. Retrieved from `https://doi.org/10.5281/zenodo.4541878` doi: 10.5281/zenodo.4541878
Ruiz-Reina, A., & López-Ruiz, A. (2021). Short-term river mouth bar devel-

opment during extreme river discharge events: The role of the phase difference between the peak discharge and the tidal level. *Coastal Engineering*, *170*(August), 103982. Retrieved from https://doi.org/10.1016/j.coastaleng.2021.103982 doi: 10.1016/j.coastaleng.2021.103982

Ruiz-Reina, A., Zarzuelo, C., López-Herrera, J. M., & López-Ruiz, A. (2020). The marine-fluvial frontier at river mouths during extreme events: A hydrodynamic approach. *Journal of Coastal Research*, *95*(sp1), 1525 – 1530. doi: 10.2112/SI95-294.1

van de Lageweg, W. I., & Feldman, H. (2018). Process-based modelling of morphodynamics and bar architecture in confined basins with fluvial and tidal currents. *Marine Geology*, *398*, 35-47. Retrieved from https://doi.org/10.1016/j.margeo.2018.01.002 doi: 10.1016/j.margeo.2018.01.002

Wright, L. D. (1977). Sediment transport and deposition at river mouths : A synthesis sediment transport and deposition at river mouths : A synthesis. *Geological Society of America Bulletin*, *88*, 857-868. doi: 10.1130/0016-7606(1977)88⟨857

River mouth hydrodynamics: the role of the outlet geometry and transient tidal and river discharge conditions on the jet structure

Antonio Ruiz-Reina[1], Alejandro López-Ruiz[1], Miguel Ortega-Sánchez[2]

[1]Departamento de Ingeniería Aeroespacial y Mecánica de Fluidos, Universidad de Sevilla, Camino de los Descubrimientos s/n, 41092, Seville, Spain
[2]Andalusian Institute for Earth System Research, University of Granada, Avda. del Mediterráneo, s/n, 18006, Granada, Spain

Key Points:

- Different outlet dimensions and nearshore depth profiles are tested
- Jet contraction is obtained for non-horizontal nearshore profiles
- Jet structure determined by tidal conditions and outlet geometry

Corresponding author: Alejandro López-Ruiz, alopez50@us.es

Abstract

The hydrodynamics of river mouths are the result of a complex interaction between river flow, tidal conditions and outlet geometry. This complex interaction of factors shapes the jet that flows onto the continental shelf and influences the dynamics of these areas. To gain insight into the response of the jet to different outlet and nearshore geometries and changing river discharge and tidal conditions, the hydrodynamics of idealised river mouths are simulated numerically. Compared to previous work, the model includes transient river discharge and tidal conditions and more realistic nearshore geometries. Comparison with classical jet theory indicates that the model adequately simulates jet hydrodynamics. The results show that both the outlet geometry and the transient river discharge and tidal conditions have a significant influence on the jet structure and evolution along the nearshore. For constant river discharge and water level conditions, the results indicate that the nearshore profile plays a key role in determining the expansion or contraction of the jet. The momentum balance shows that the jet behaviour is related to the momentum transport and the barotropic terms. In cases where the river discharge and tidal conditions are transient, the jet alternates between a structure with two velocity maxima at the edges or a single peak in the centre during the tidal cycle. This alternation occurs as a function of the time along the tidal phase and the time lag between the tidal conditions and the river hydrograph. The morphodynamic consequences of these two different jet structures are also discussed.

Plain Language Summary

The dynamics of river mouths are determined by a very complex interaction between the hydrological characteristics of the basin, the shape of the mouth and continental shelf, and the tidal and other marine conditions. Although these dynamics have been extensively studied for very simple mouth geometries and constant river discharge in the absence of sea level variations, the role of both the geometric parameters of these systems and tidally driven temporal variations in discharge and sea level have not been systematically analysed. This manuscript analyses, using a process-based numerical model, the role played by all these factors in the structure of the jet stream generated at the river mouths. The focus is on small basin river mouths, where the temporal variations in river discharge have a duration similar to that of the tidal period. The results show that the jet structure is mainly determined by the geometry of the continental shelf. In addition, the tides play an important role, as the jet structure varies significantly during the tidal cycle. The morphodynamic implications of the results are also discussed throughout the manuscript.

1 Introduction

River mouths and deltas are areas of significant ecological and socio-economic interest, containing some of the world's most valuable ecosystems and densely populated areas (Lamb et al., 2012). This has led to the development of important industrial and agricultural areas, which often require inland waterways along the river courses that feed these mouths. The processes of transport and mixing of nutrients, salinity and sediments in these environments are of great importance for the biogeochemical evolution of many riverine and marine ecosystems, as well as for the formation of morphologies such as bars and deltas. The development of these features generally follows sediment deposition, which can occur through natural levee growth and channel elongation, or through deposition and vertical aggradation of estuarine bars (Fagherazzi et al., 2015). Furthermore, both river mouths and deltas are susceptible to extreme flooding events caused by river discharge, storm surge or a combination of both (Romero-Martín et al., 2024). The management of these extreme events is becoming increasingly challenging due to changes in their frequency and intensity caused by climate change (Fernandino et al., 2018). Consequently, improving knowledge of the dynamics of river mouths is of fundamental importance from both an environmental and socio-economic perspective.

The hydrodynamics of the river mouth is dominated by a confined turbulent jet that flows into a basin where waves, storm surges and astronomical tides can modify the shape and intensity with which this jet spreads laterally and reduces its seaward velocity. The geometry of the outlet and nearshore region also play a key role in the evolution of this jet, influencing both the flow structure at the outlet and the propagation velocity once it enters the shelf. Consequently, the interaction between hydrodynamics and sediment is a feedback process in which the jet structure determines the sediment deposition, which in turn determines the morphology with the formation of features such as bars, which are crucial for the development of deltas.

To characterise jet hydrodynamics, authors such as Abramovich and Schindel (1963) and Özsoy and Ünlüata (1982) developed time-averaged solutions of the integral jet theory, in which the jet structure is divided into two zones: (1) the zone of flow establishment (ZOFE) near the outlet, where the flow leaves the channel and expands abruptly; and (2) the zone of established flow (ZOEF) far from the outlet, where the flow is stable and similarity hypotheses can be applied (Ortega-Sánchez et al., 2008). From these pioneering works, this theory has been refined to describe a transition zone between the ZOFE and the ZOEF (Ortega-Sánchez et al., 2008), although in the last 15 years the focus has been on the use of process-based models to analyse the effects of jet hydrodynamics on bar development, analysing the effects of sediment size (Edmonds & Slingerland, 2007), levee formation (Rowland et al., 2010), human activities (Anthony et al., 2014; Fan et al., 2006; Besset et al., 2019), bed roughness (Canestrelli et al., 2014) or the presence of vegetation (Nardin et al., 2016; Lera et al., 2019).

In most of these works, simplified outlet geometries were defined using lower channel width-to-outlet depth ratios (Canestrelli et al., 2014). Furthermore, numerous studies have considered channels with no slope or very gentle slopes flowing into horizontal basins (Edmonds & Slingerland, 2007; Leonardi et al., 2015; Nardin et al., 2016). Jiménez-Robles et al. (2016) analysed the influence of shelf slope on jet hydrodynamics, defining the shelf as a surface with a constant slope. Their results show that this slope plays a very important role in the jet structure, and therefore in the formation of bars and their final geometry. Shortly afterwards, Jiménez-Robles and Ortega-Sánchez (2018) also analysed the role of the river-shelf orientation.

Regarding the main fluvial and marine drivers, most of these studies consider constant river discharge conditions and neglect the effect of astronomical tides, storm surges and waves. However, works such as Nardin and Fagherazzi (2012) and Nardin et al. (2013) have analysed the role of waves in the formation and evolution of estuarine bars, concluding that waves play an important role in the timing of bar evolution as well as in their final geometry. Leonardi et al. (2015) focused on the influence of tides in a simplified geometry with a horizontal bottom. They considered two scenarios: one with a constant river discharge (river-dominated) and the other with oscillating discharge (tidal-dominated). In both cases, the impact of the ebb/flood cycles in the channel was replicated. The results obtained show that in the river-dominated case the tide has a wave-like dispersive effect, whereas in the tide-dominated case the effect varies considerably depending on the tidal range and river discharge. More recently, Ruiz-Reina and López-Ruiz (2021) analysed the short-term evolution of the mouth bar during extreme river discharge events, focusing on the role of the phase difference between the peak discharge and the tidal level. In this case, an equilibrium beach profile was used for the nearshore geometry. Their results showed that this phase plays a key role in the final geometry of the river mouth bar developed during the discharge events. Nevertheless, the hydrodynamics and jet structure were not analysed, nor was the role of the outlet geometry.

This literature review suggests that the interactions between fluvial discharge and marine drivers are very complex, although they are crucial for the management of river mouths and deltas. Furthermore, despite all the recent advances described above, there are still important aspects to be analysed in order to describe the jet structure at outlets. In particular, the impact of more realistic geometries, both in terms of outlet dimensions and platform shape, on the hydrodynamics described for simpler geometries remains to be further explored. Additionally, the combined effect of the astronomical tide and the role of the time lag between tidal and flow conditions in short river discharge events (time scale similar to that of the tide) remains to be determined.

The main objective of this work is twofold: on the one hand, to analyse the effect of mouth characteristics (ratio of outlet depth to channel width) and nearshore geometry on the jet structure; on the other hand, to analyse the effect of tides and short fluvial discharge pulses on the jet geometry, where their phase difference with the astronomical tide can influence the jet hydrodynamics. To achieve this goal, a process-based numerical model will be used on idealised but realistic geometries, maintaining the channel and platform slopes, as well as the outlet shapes commonly observed in small river mouths with high seasonal variability and relatively high slopes due to their proximity to mountain ranges. This proximity, which limits the size of the hydrological basins, also causes the fluvial discharge pulses to be short and may have the same time scale as the astronomical tides (Ruiz-Reina et al., 2020; Ruiz-Reina, 2021; Ruiz-Reina & López-Ruiz, 2021). The manuscript is structured as follows: Section 2 outlines the theoretical basis of jet hydrodynamics and how it can be adapted to more complex but more realistic profiles (dynamic equilibrium profile). Section 3 describes the methodology used, while the results obtained are presented and discussed in Sections 4 and 5, respectively. Finally, the main conclusions are presented in section 6.

2 Theoretical framework

Jet theory has been used extensively in recent decades to describe the jet that develops when a river discharges into a still water basin, with fluvial forces dominating over marine forces (Wright, 1977). In particular, the dominant primary force is a combination of inertia and turbulent bed friction, i.e. a river discharges into a still body of water with the same density as the incoming river (Fagherazzi et al., 2015), and no buoyancy effects are considered. At river mouths, the flow can be described by the shallow water equations (Özsoy & Ünlüata, 1982; Leonardi et al., 2013) due to the larger ratio of channel width to outlet depth ($W/h_0 > 4$, see figure 1). The hydrodynamics of such a turbulent jet, also called a shallow bounded plane jet (Fagherazzi et al., 2015), can be divided into two zones: (1) a zone of flow establishment (ZOFE), in the vicinity of the outlet, characterised by a core of constant velocity and rapid momentum dissipation; and (2) the zone of established flow (ZOEF), where the entire jet is dominated by the turbulent eddies and the centreline velocity decreases with a Gaussian transverse distribution of the velocity profile (Özsoy & Ünlüata, 1982; Jirka & Giger, 1992).

Nevertheless, subsequent works (Ortega-Sánchez et al., 2008) contributed to this theory, incorporating an additional zone between the ZOFE and ZOEF regions, in order to explain that the transition between them requires a certain length to occur. Although it has not yet been subjected to a comprehensive research, this transitional zone appears to be primarily dependent on the friction and the longitudinal changes of the bathymetry and momentum balance. Therefore, based on the streamwise velocity and the jet structure, three theoretical regions can be considered: i) ZOFE, with constant velocity along the jet axis; ii) ZOT (zone of transition), with decreasing velocity along the centre line and iii) ZOEF, with a Gaussian transversal velocity distribution, which can be approximated with sufficient accuracy for the purposes of this work by the following expression (see figure 1 for the definition of the variables) (Giger et al., 1991), with

$A = -\ln(0.5) = 0.693$:

$$\frac{u(x,y)}{u_c(x)} = e^{-A\zeta^2} \tag{1}$$

Regarding the ZOFE and ZOEF regions, an extensive body of work has been developed for an integral plane jet theory assumed to be incompressible, stationary, depth-constant and frictionless (Jiménez-Robles et al., 2016). A more complex analysis was developed by Özsoy and Ünlüata (1982) for ebbing flows at microtidal inlets, incorporating the effects of bottom friction to analytically solve the depth-averaged equations of motion under the assumptions of quasi-steadiness and self-similarity. The equations of motion (mass and along channel momentum balance) for the jet are (Özsoy & Ünlüata, 1982):

$$\frac{\partial(hu)}{\partial x} + \frac{\partial(hv)}{\partial y} = 0 \tag{2}$$

$$\frac{\partial(hu^2)}{\partial x} + \frac{\partial(huv)}{\partial y} = -\frac{f}{8}u^2 + \frac{1}{\rho}\frac{F_{xy}}{\partial y} \tag{3}$$

where h is the water depth, u and v are the depth-averaged velocity components in the x and y directions (figure 1), ρ is the water density, F_{xy} is the depth-integrated turbulent shear stress, and f is the friction factor, which can be expressed as a function of the Chezy number ($f = 8g/C_z^2$). To solve equations 2 and 3 along the channel centreline ($y = 0$, figure 1) and obtain $u_c(x) = u(x,0)$, the velocity distribution $u(x,y)$ is assumed to be self-similar with respect to the normalised coordinate $\zeta = y/b(x)$, where $b(x)$ is the half-width of the jet, which facilitates the integration of the equations of motion. According to Abramovich and Schindel (1963), the velocity field is parameterised as follows, where $F(\zeta) = u(x,y)/u_c(x)$:

$$F(\zeta) = \begin{cases} 0 & 1 < \overline{\zeta} \\ \left(1 - \overline{\zeta}^{1.5}\right)^2 & 0 < \overline{\zeta} < 1; \quad \overline{\zeta} = \dfrac{\zeta - r/b}{1 - r/b} \\ 1 & \overline{\zeta} < 0 \end{cases} \tag{4}$$

where $r(x)$ is the core width which vanishes at $x = x_s$, the boundary between ZOFE and ZOEF. The integration of equations 2 and 3 is based on the assumption that $u(x,y)$ and F_{xy} decrease as y increases, but with consideration of a lateral entrainment velocity $v_e = v(x,y)|_{y\to\infty} = au_c$, where a is the entrainment coefficient. When the following normalised variables are introduced (Özsoy & Ünlüata, 1982):

$$\xi = \frac{x}{b_0}; \quad \mu = \frac{fb_0}{8h_0}; \quad H(\xi) = \frac{h}{h_0}; \quad R(\xi) = \frac{r}{b_0}; \quad B(\xi) = \frac{b}{b_0}; \quad U(\xi) = \frac{u_c}{u_0}; \tag{5}$$

two ordinary differential equations are obtained for both regions:

$$\frac{d}{d\xi}(I_1 HBU) = aHU \tag{6}$$

$$\frac{d}{d\xi}(I_2 HBU^2) = -\mu I_2 BU^2 \tag{7}$$

where b_0, h_0, and u_0 are respectively the half-width, depth and velocity at the outlet. The non-dimensional flow establishment distance is expressed as ξ_s.

From this point on, the analysis and subsequent comparisons are limited to the solution for the streamwise velocity along the axis in the ZOEF region. Consequently, the numerical constants I_1 and I_2 can be obtained as 0.450 and 0.316 (Özsoy & Ünlüata, 1982), respectively, after integrating $F^n(\xi)$ between 0 and 1 ($n = 1, 2$). The solution

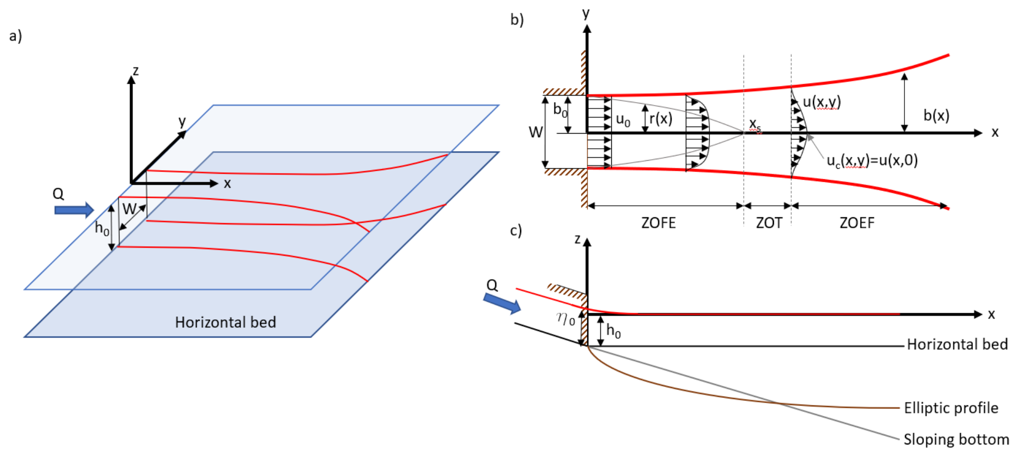

Figure 1. a) Definition sketch of a horizontal bounded jet. b) Zone of Flow Establishment (ZOFE), Zone of Established Flow (ZOEF) and Zone of Transition (ZOT). Q is the river discharge, h_0 is the outlet depth, η_0 is the water level at the outlet, W is the mouth width, b_0 is the mouth half-width, u_0 is the mean outlet velocity, $u_c(x)$ is the jet velocity along the axis, $u(x, y)$ is the streamwise velocity, $b(x)$ is the jet half-width, and x_s is the flow establishment distance. Panel c) shows the three considered nearshore profiles.

of the ODE system for this ZOEF region (equations 6 and 7), and hence the jet structure, is strongly dependent on the nearshore profile geometry $H(\xi)$. Previous works mainly analysed turbulent jet hydrodynamics for horizontal beds, where $H = 1$ (Edmonds & Slingerland, 2007; Nardin & Fagherazzi, 2012; Leonardi et al., 2015), or for sloping beds with constant slope m, where $H = 1 + \nu\xi$ and $\nu = mb_0/h_0$ (Jiménez-Robles et al., 2016). However, these are simplified geometries of the nearshore profile that in nature presents a variable slope with a cross-shore variations of the water depth that can be described by its equilibrium shape $h(x) = Ax^{2/3}$ (Dean & Dalrymple, 2004), where A is the profile scale factor, a dimensional parameter that mainly depends on the sediment size. This elliptical profile, after non-dimensionalisation, is expressed as $H = 1+k\xi^{2/3}$, where $k = Ab_0^{2/3}/h_0$. The solution of the ODE system for the ZOEF region using a finite difference scheme described in the Supporting Information is implemented to obtain u_c for the three geometries described above. These results are used to validate the simulations performed with the depth-averaged 2D hydrodynamic model for steady-state conditions (still water level and constant river discharge) shown in section 4.1.

3 Material and methods

3.1 Physical scenarios

The physical scenario in which the numerical model was implemented represents a straight channel flowing into a basin representing the continental shelf. To analyse the role of the mouth geometry on the jet structure, three parameters were varied: (1) the width of the channel W; (2) the depth of the channel at the outlet with respect to the mean sea level (hereafter MSL) h_0; and (3) the geometry of the continental shelf.

The channel geometry was defined with a rectangular cross section perpendicular to the shoreline orientation. This channel has a width of $W_i = (100, 200, 500)$ m and a longitudinal slope of $S_s = 0.002$. The lateral edges of the section are vertical walls with a height greater than 4 m at each section to prevent overtopping and to ensure mass conservation between the upstream boundary condition and the mouth. The depth of the outlet is h_{0i}=(1, 3) m. The length of the channel is 2.5 km, which ensures that the tidal excursion can be simulated correctly while avoiding the numerical effects of the upstream boundary condition (figure 2).

The shoreline is straight and the geometry of the beach profile was defined as (1) a horizontal bottom with depth h_{0i}; (2) a bottom with constant slope $S = 0.05$; and (3) a bottom with the equilibrium elliptical shape defined by Dean and Dalrymple (2004) (see Ruiz-Reina and López-Ruiz (2021) for further details). This elliptical shape is concave and therefore more realistic in the shallower part of the continental shelf. Finally, the platform is extended to the offshore boundary of the domain (figure 2) with maximum depths above 50 m. The combination of W_i, h_{0i} and platform geometries configures a set of 18 physical scenarios (see table 3.3).

3.2 Model description

The numerical model implemented to solve the hydrodynamics of the jet is Delft3D (Lesser et al., 2004), which is widely used to analyse the hydrodynamics of river mouths (Edmonds & Slingerland, 2007; Nardin & Fagherazzi, 2012; Nardin et al., 2013; Nienhuis et al., 2016; Boudet et al., 2017; van de Lageweg & Feldman, 2018; Gao et al., 2019). This model is capable of solving transient flows using the shallow water equations. In this case, buoyancy, ocean waves, Coriolis and wind effects are neglected using a depth-averaged version of the model in agreement with previous theoretical, experimental and numerical works (Lamb et al., 2012; Jiménez-Robles et al., 2016).

The model solves the shallow water equations for unsteady, incompressible, turbulent flow using a finite difference scheme. The continuity and horizontal momentum equations are:

$$\frac{\partial \eta}{\partial t} + \frac{\partial hu}{\partial x} + \frac{\partial hv}{\partial y} = S \tag{8}$$

$$\frac{\partial u}{\partial t} + u\frac{\partial u}{\partial x} + v\frac{\partial u}{\partial y} = -g\frac{\partial \eta}{\partial x} + M_x + g\frac{u\sqrt{u^2+v^2}}{C_{z,u}^2 h} + \epsilon_H\left(\frac{\partial^2 u}{\partial x^2} + \frac{\partial^2 u}{\partial y^2}\right) \tag{9}$$

$$\frac{\partial v}{\partial t} + u\frac{\partial v}{\partial x} + v\frac{\partial v}{\partial y} = -g\frac{\partial \eta}{\partial y} + M_y + g\frac{v\sqrt{u^2+v^2}}{C_{z,v}^2 h} + \epsilon_H\left(\frac{\partial^2 v}{\partial x^2} + \frac{\partial^2 v}{\partial y^2}\right) \tag{10}$$

where η is the water level with respect to MSL, t is time, S represents the sources/sinks of water, and g stands for the gravitational acceleration. $C_{f,u}$ and $C_{f,y}$ are the Chézy roughness coefficients in the x and y directions, respectively. The left-hand side terms in equations 9 and 10 represent the local acceleration and the advective (momentum transport) terms, whereas the first, second, third and fourth terms in the right-hand side represent the pressure gradient acceleration (barotropic), the external sources or sinks of momentum, friction and horizontal Reynolds stresses, respectively, where ϵ_H is the horizontal eddy viscosity. For a detailed description of the model the reader is referred to Lesser et al. (2004) and Ruiz-Reina and López-Ruiz (2021).

3.3 Model setup and numerical scenarios

The physical scenarios described in Section 3.1 were implemented using a regular grid of quadrangular cells aligned with the channel axis and the shoreline. To improve the efficiency of the simulations, the cell size varies from 100×100 m^2 at the offshore boundary to 10×10 m^2 at the outlet and the river channel. This grid was previously used by Ruiz-Reina and López-Ruiz (2021), where a sensitivity analysis was conducted

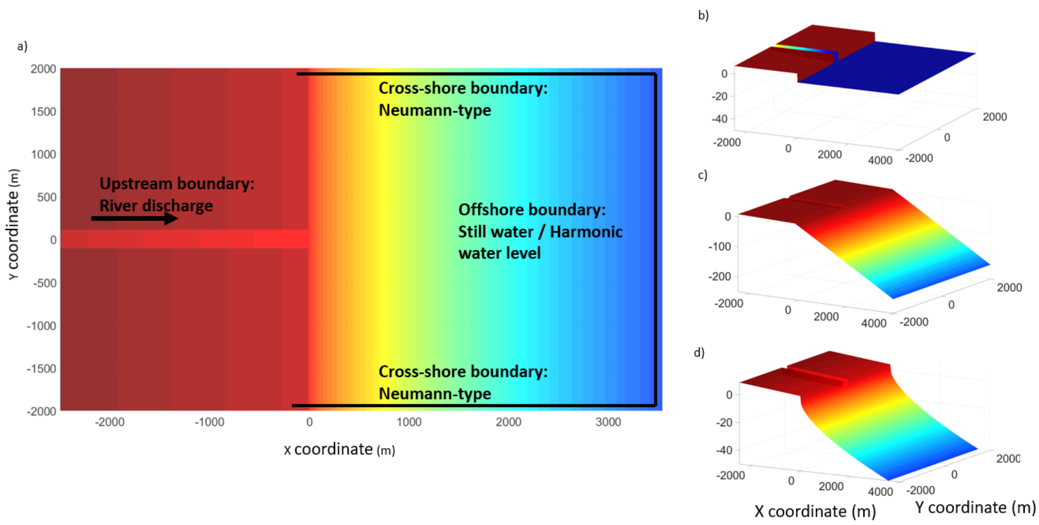

Figure 2. Physical scenarios: a) Plan view of the domain and boundary conditions used; and 3D plots including the bathymetry and the river channel for b) horizontal bottom, c) sloping bottom and d) elliptical profile.

to ascertain the optimal cell size. In order to meet the stability and accuracy requirements of the numerical scheme, a time step of 1.5 s was used. As in Ruiz-Reina and López-Ruiz (2021), constant coefficients were used for the bed roughness ($C_z = 55$) and the background horizontal eddy viscosity ($\epsilon_H^{back} = 1$ m^2/s) over the computational grid.

Three types of open boundaries were defined (figure 2): (1) the offshore boundary, with water level conditions; (2) the upstream boundary, located in the very upstream part of the channel, with river discharge conditions; and (3) two cross-shore boundaries, where Neumann-type conditions were used, imposing a zero water level gradient in the direction perpendicular to the boundary (Roelvink & Walstra, 2004).

Depending on the upstream and offshore boundary conditions, three types of simulations were defined. The first (Type 1, table 3.3) uses constant river discharge and no tides to analyse the role of the outlet and nearshore geometry in the jet structure under conditions equivalent to those used to define the plane-turbulent jet theory described in section 2. In this case, the offshore boundary condition is set to $\eta = 0$ throughout simulation. The river discharge is defined with a constant discharge rate per unit channel width $q = Q_i/W_i = 2.5$ m^2/s. As there are three values of W_i among the defined physical scenarios, three discharge values $Q_i = (250, 500, 1250)$ m^3/s were used. Keeping q constant allows the effect of channel geometry and W/h_0 ratio to be analysed without the results being affected by the different averaged velocities at the outlet section.

The second type of simulation (Type 2, table 3.3) is used to assess the impact of the tide and how it modifies the jet structure. In this case, the river discharge conditions are maintained, but at the offshore boundary the water level varies with the astronomical forcing defined by a single semi-diurnal harmonic with an amplitude of 1 m. Finally, in the third type of simulation (Type 3, table 3.3), the role of the river discharge pulses in the jet structure is analysed by defining different hydrographs at the upstream boundary, while at the offshore boundary the conditions defined for Type 2 simulations are maintained. The hydrographs were defined using the SCS (US Soil Conservation Service) method for the Chow et al. (1988) shape with a duration of 18 hours, corresponding to one and a half complete tidal cycles, and a peak discharge of $q_p = 2.5$ m^2/s. According to (Ruiz-

Type	Id	Profile	W (m)	h_0 (m)	Q_p (m^3/s)	Offshore	ϕ (rad)
1	111 121 151	Horizontal	100 200 500	1.0	250 (C) 500 (C) 1250 (C)	Still water	-
1	211 221 251	Sloping	100 200 500	1.0	250 (C) 500 (C) 1250 (C)	Still water	-
1	311 321 351	Elliptical	100 200 500	1.0	250 (C) 500 (C) 1250 (C)	Still water	-
1	113 123 153	Horizontal	100 200 500	3.0	250 (C) 500 (C) 1250 (C)	Still water	-
1	213 223 253	Sloping	100 200 500	3.0	250 (C) 500 (C) 1250 (C)	Still water	-
1	313 323 353	Elliptical	100 200 500	3.0	250 (C) 500 (C) 1250 (C)	Still water	-
2	221-T 321-T 223-T 323-T	Sloping Elliptical Sloping Elliptical	200	1.0 1.0 3.0 3.0	500 (C)	Tide	-
3	321-HT 321-ET 321-LT 321-FT	Elliptical	200	1.0	500 (hyd)	Tide	0 $\pi/2$ π $3\pi/2$

Table 1. Numerical scenarios: main characteristics. For the river discharge conditions, C means constant discharge whereas hyd means variable discharge (hydrograph)

Reina & López-Ruiz, 2021), the base time of the hydrographs was the same regardless of the peak discharge value. Furthermore, to analyse the importance of the phase between the peak discharge at the upstream boundary and the tide at the offshore boundary, the beginning of the hydrograph was defined at 4 different times, corresponding to the peak discharge at high tide, MSL to low tide (ebb tide), low tide and MSL to high tide (flood tide). The combination of such different boundary conditions and physical scenarios results in a total of 26 simulations (table 3.3). The total duration of each simulation is 48 hours, including an initial minimum spin-up interval of 24 hours to limit the effects of the prescribed still water initial conditions.

4 Results

4.1 Still water and constant discharge: analysis of the influence of outlet geometry and nearshore profile

4.1.1 Comparison to jet theory

The numerical modelling was validated by comparing its results in the ZOEF region with those obtained with the numerical solution of the Özsoy and Ünlüata (1982) equations (jet theory) for Type 1 simulations (Table 3.3), assuming entrainment coefficients similar to those used by Jiménez-Robles et al. (2016). A first examination of each simulation (figure 3) shows that the centreline velocity begins to decrease as soon as the jet enters the nearshore region. This observation is consistent with the results of Jiménez-Robles et al. (2016) and Nardin et al. (2013), who claimed that the ZOFE region can be neglected in such cases. Consequently, for each simulation, there exists an initial length of decreasing velocity and changing jet structure from the edges to the axis, which can be considered as an evidence of the existence of a transition region (ZOT).

The first row in figure 3 shows the results of the simulations performed with $h_0 =$ 1 m. For those with a horizontal bottom geometry, it can be observed that there is a poor fit between the model results and the values predicted by the jet theory, especially for larger widths (W). These differences may be due to the decrease in the predicted role of friction as W/h_0 increases. In fact, it has been found that by reducing the parameter μ (eq. 5) in the Özsoy and Ünlüata (1982) equations by a certain percentage (85%, 70%, 40% for $W = [100, 200, 500]$ m, respectively) both results converge.

In the case of sloping bottom simulations there are notable differences with respect to those with a horizontal bed. For cases with $h_0 = 1$ m, the velocity profile obtained with the numerical model has a local maximum at about $\xi = 2.0$, from which the velocities decrease, highlighting the development of the ZOT in the initial part of the jet as it enters the nearshore. This maximum is related to the length of transition required for the jet to fully develop as a consequence of the balance between jet contraction and its energy dissipation as it advances along the nearshore profile, as shown in the next section. This shape of the velocity profile is more pronounced for simulations with $W =$ $(200, 500)$ m, showing the influence of W on the jet structure in the ZOT region. In comparison with the jet theory solutions, a good fit can be observed from $\xi = 4.0$. The simulations with sloping bottom and $h_0 = 3$ m agree with these results, although in these cases the velocity profile is constantly decreasing for $W = 100$ m, while it shows a slight increase for $W = 200$ m, and for $W = 500$ m a relative maximum of the velocity is observed in the vicinity of $\xi = 1.5$.

The elliptical profile simulations show velocities very similar to the previous sloping bottom results, with a local maximum velocity observed at $\xi = 1.5{-}2.5$. The similarity of these results shows that the variable slope of the elliptical nearshore profile does not affect the shape of the velocity profile at distances close to the outlet. However, it can be observed that u_c/u_0 is higher for the elliptical profile simulations than for those with a sloping bottom.

Regarding the simulations with $h_0 = 3$ m and horizontal geometry, the μ parameter has to be reduced less in the theoretical results to obtain a good fit (about 80% for $W = 500$ m), highlighting a more relevant role of the bottom friction. On the other hand, for the sloping and elliptical bottom profiles the fit between the numerical models and the jet theory is particularly good from $\xi = 4.0{-}5.0$ offshore. Therefore, for the W/h_0 ratios for which the jet theory solution was developed, the numerical model satisfactorily reproduces the jet behaviour that has been extensively analysed in the literature (Abramovich & Schindel, 1963; Özsoy & Ünlüata, 1982; Jirka & Giger, 1992; Fagherazzi et al., 2015).

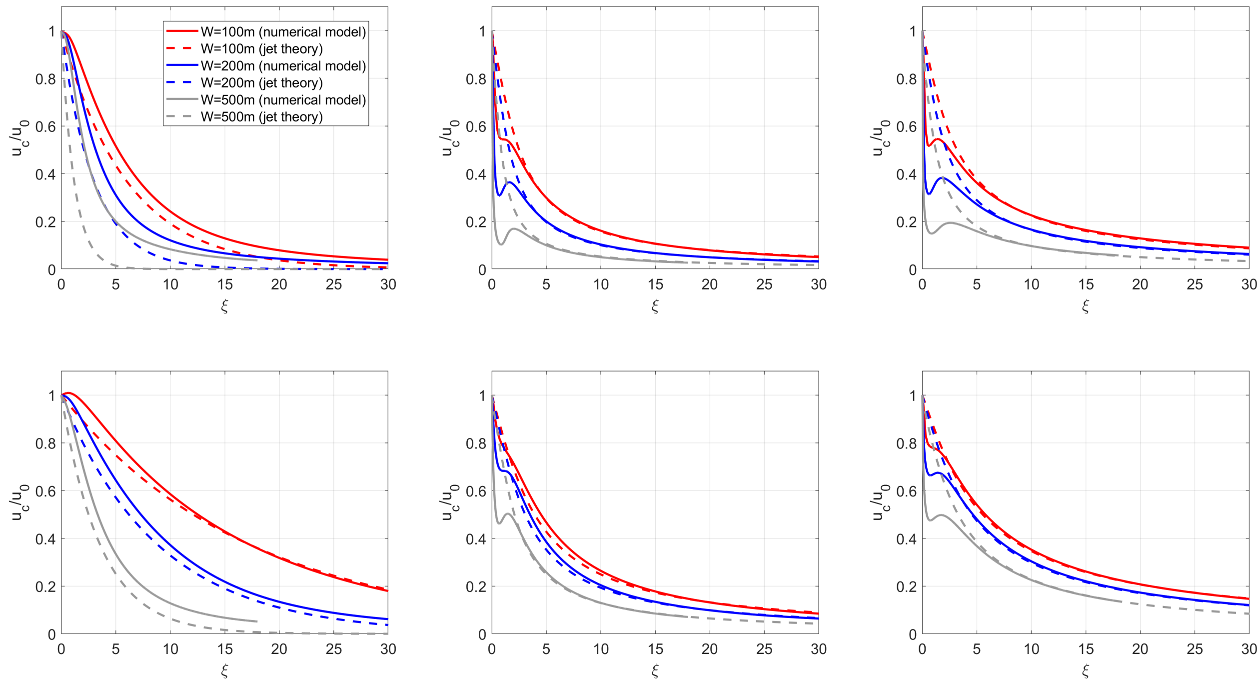

Figure 3. Velocity profiles obtained with the numerical model (solid line) and the jet theory (dashed line) for $h_0 = 1$ m (first row) and $h_0 = 3$ m (second row) and the horizontal, sloping and elliptical profiles (first, second and third columns, respectively). The X axis represents the non-dimensional distance to the outlet, whereas the Y axis represent the non-dimensional streamwise velocity.

Considering the above results, the numerical model is a valuable and reliable tool for the analysis of the jet structure and the hydrodynamics of the river mouth. However, its applicability goes beyond that of jet theory, as it can be extended to more complex and realistic geometries with higher W/h_0 ratios. Furthermore, the results presented in figure 3 show that the varying local maximum observed in the velocity profile is associated with the transition of the jet hydrodynamics to full development.

4.1.2 Streamwise velocity of the jet

Figure 4 illustrates the depth-averaged velocity contours in the vicinity of the outlet for the 18 numerical experiments with a constant river discharge (Type 1). In this figure, the distances from the outlet are not non-dimensional to show the velocity isolines in a more realistic way. The results show that the profile geometry controls the shape of the jet: while the horizontal bed shows an expanding jet throughout the domain with velocity contours extending away from the jet axis, the sloping and elliptical profiles show a jet that contracts near the outlet until it begins to expand at a certain distance. This phenomenon was already identified by Özsoy and Ünlüata (1982), who pointed out that with increasing depth the jet contracts due to mass conservation. The numerical results demonstrate the same behaviour for more complex geometries. Consequently, the impact of a nearshore environment with increasing depth is to suppress the expansion of the jet due to bottom friction, which becomes less dominant.

For $h_0 = 1$ m and horizontal bed the jet is wider because bottom friction dominates. In contrast, for $h_0 = 3$ m, the effect of bottom friction diminishes and the jet

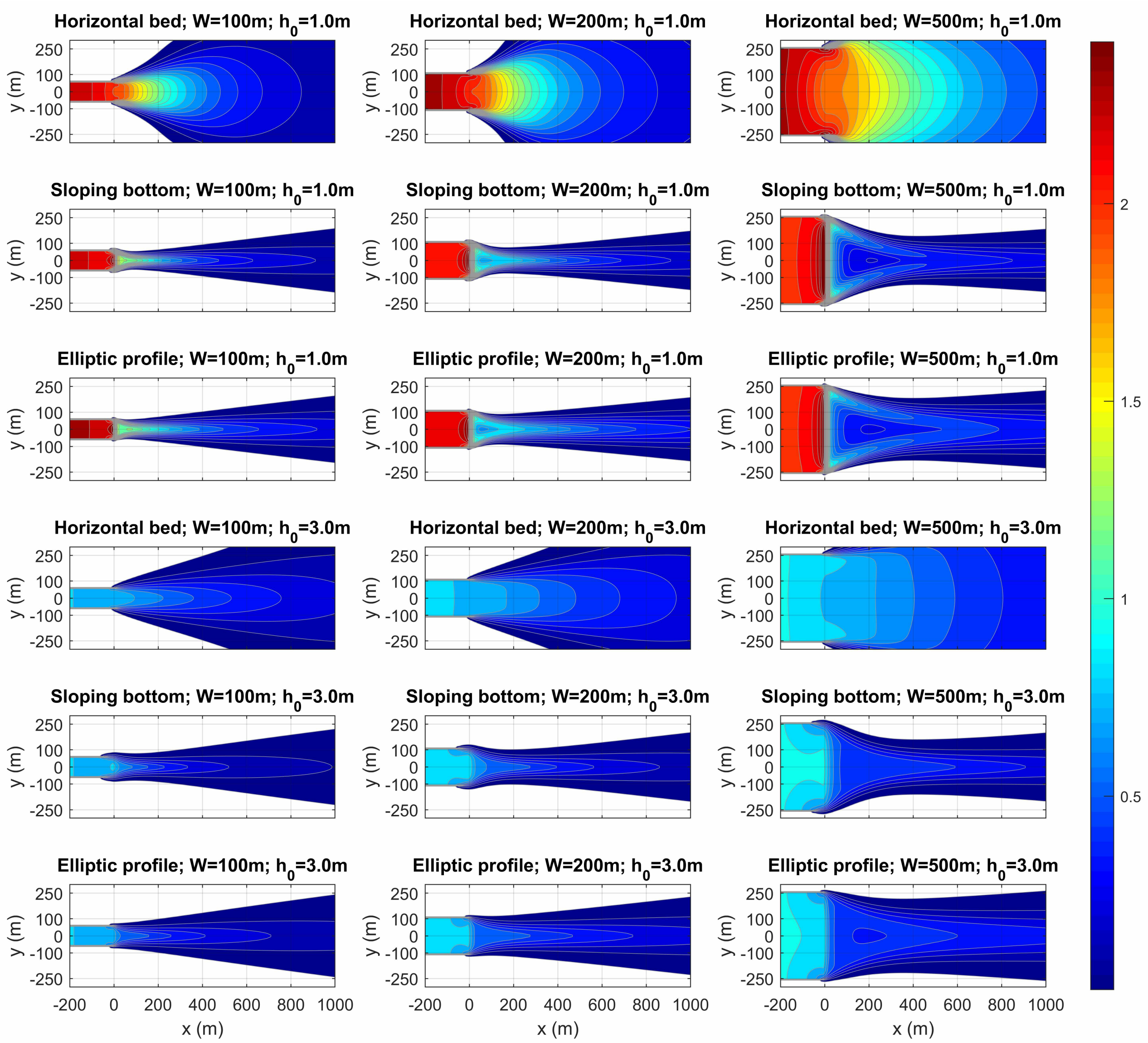

Figure 4. Streamwise velocity isolines for simulations with constant discharge and still water in the nearshore region (Type 1 in Table 3.3).

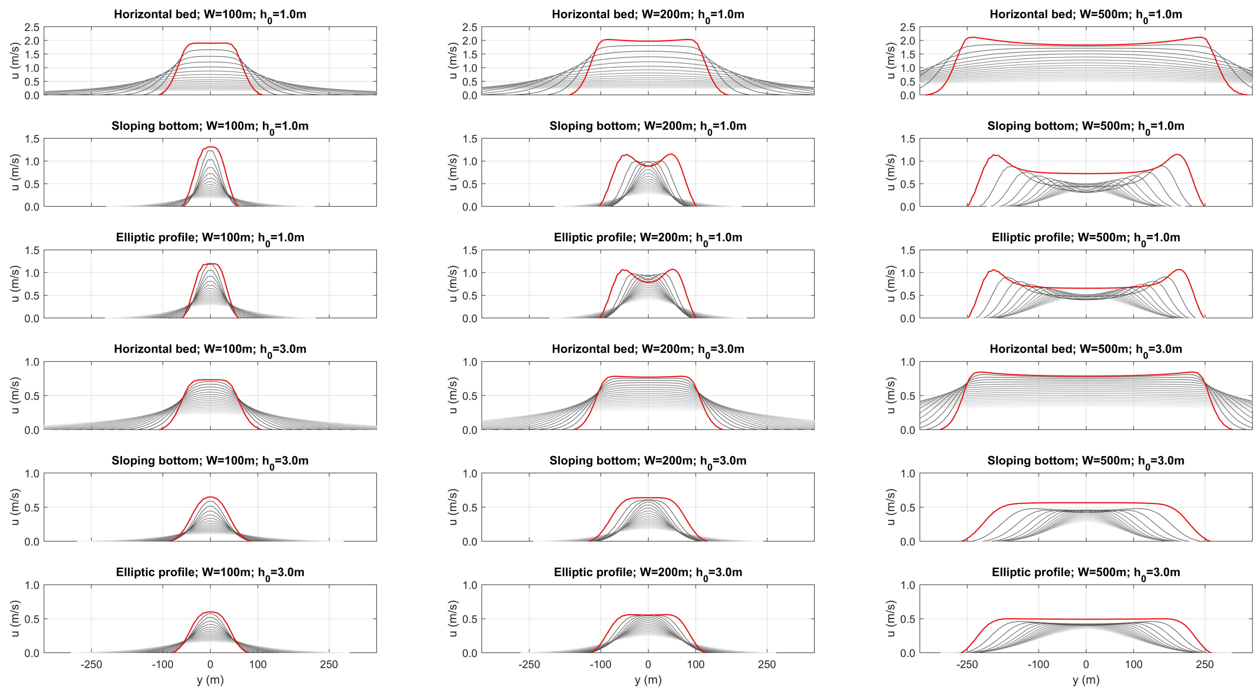

Figure 5. Transverse distribution of the streamwise velocity along the jet. In red, the velocity profile for a section located where the jet enters the nearshore area (x=50 m).

reduces its spreading. The jet contraction observed in simulations with sloping and elliptical profiles is comparable, but there are two key distinctions: i) the jet width is slightly higher in simulations with elliptical profiles, due to the lower slope of the bed profile from a certain distance from the mouth ($x = 100$ m); and ii) the distance over which the jet contraction extends also depends on the bed profile, but the influence of the mouth width is more pronounced. Figure 4 clearly shows that the contraction for a width of 500 m extends over a greater distance than those with smaller widths.

This phenomenon is also illustrated in figure 5, which shows the transverse distribution of the streamwise velocity through a series of cross sections. The maximum velocities for $h_0 = 1$ m are significantly higher (approximately twice) than for $h_0 = 3$ m. Furthermore, simulations with $h_0 = 1$ m and $W = (200, 500)$ m show a velocity profile with two peaks at the edges of the jet, regardless of the nearshore geometry. However, for $W = 100$ m, the velocity profile appears to show a single peak along the jet centre. For $h_0 = 3$ m, simulations with $W = (200, 500)$ m tend to have velocity profiles with a constant value at the top, decreasing towards the jet boundaries, consistent with the jet theory description in the ZOEF region. Simulations with a narrower width ($W = 100$ m) clearly show a velocity profile with a peak velocity along the jet centre. The similarity of the results for sloping and elliptical geometries can be attributed to the value of the longitudinal slope of the nearshore profile, as both profiles have a similar slope for the first 100 m. However, beyond this distance, the slope of the elliptical profile remains lower, implying a shallower bottom depth and leading to a smaller reduction in the streamwise velocity and a larger jet width at these distances.

These results show that W plays a significant role in determining the distance of flow establishment and hence the jet structure. Moreover, $\overline{u_0}$ also has a relevant influence and it is closely related to h_0, with lower values of h_0 associated with higher values of velocity. In particular, shallower outlets result in velocity profiles with two peak velocities along the edges of the jet, whereas deeper outlets are associated with velocity profiles with a single peak velocity along the jet axis.

4.1.3 Transverse component of the velocity

Figure 6 shows the non-dimensional transverse component of the velocity v/u_c at different sections where the flow is clearly established. The velocity trends observed in this figure are consistent with those described in Jiménez-Robles et al. (2016). For the horizontal bed cases, the velocity magnitudes are larger, with maxima in the region of $v/u_c = 0.5$. In contrast, for the sloping and elliptical profiles and $h_0 = 1$ m, v/u_c is below 0.1 at both cross sections.

Figure 6 also shows differences in the flow direction for the horizontal bed simulation on either side of the jet axis, so that the negative values are on the left and the positive values on the right. This sign criterion corresponds to a jet expanding with a transverse velocity that has its maximum at a point located at a distance equal to the half-width of the jet ($\zeta = 1$) for $h_0 = 1$ m and slightly closer the outlet for $h_0 = 3$ m. On the other hand, for the sloping and elliptical profiles, a change of sign is also observed in the velocities on either side of the jet, indicating a contracting jet. The two geometries show a remarkably similar magnitude and shape of the transverse velocity profile for simulations with $h_0 = 1$ m and $h_0 = 3$ m. The magnitude of the transverse velocity with respect to the streamwise velocity indicates that the jet is weakly contracting, resulting in no significant variation in its width. It should be noted that the parameter h_0 only has a relevant influence for geometries with a horizontal bottom.

The analysis of the transverse velocity shows that for sloping bottom geometries there is a value of slope for which the jet width is constant. As stated by Özsoy and Ünlüata (1982), the width of the jet depends, on the balance between the entrainment coefficient, μ and ν. Therefore, it depends, mainly, on the bottom roughness and geometry.

4.2 The effect of the tides

This section presents a detailed analysis of the influence of the tide on the jet velocity profile, employing Type 2 simulations. The analysis is limited to cases with $W =$ 200 m, $Q = 500$ m$^3/s$ and geometries corresponding to the sloping bottom and the elliptical profile (Table 3.3). The horizontal bottom profile was excluded from the analysis, as the tidal amplitude is similar to the water depth at the outlet.

Figure 7 shows the streamwise velocity contours at various stages throughout the tidal cycle. As with the results of the Type 1 simulations, the nearshore geometry plays a minor role in the velocity distribution. However, the final jet width is slightly larger for the simulations with an elliptical nearshore profile, which is a consequence of the shallower depth. Conversely, the initial depth of the water column, h_0, is a significant variable. Higher values of h_0 result in a lower mean exit velocity, $\overline{u_0}$, which favours the development of a jet with maximum velocity at the axis and a Gaussian transverse distribution. The tidal conditions emerge as a key factor that plays a significant role in the jet structure at the intratidal scale. Focusing on the simulations with $h_0 = 1$ m, for high tide conditions, maximum velocity values are observed at the outlet along the edges of the jet in sections close to the mouth, although there is a rapid evolution of the jet taking a maximum value along the axis. However, for low tide conditions, the existence of two local maximum velocities for the cross-channel profiles extends over longer distances along the jet path, which means that the development of the jet requires a longer distance, approximately twice as long as for high tide. For ebb and flood conditions, identical velocities are obtained and show a jet structure similar to that for low tide conditions. This means that a jet structure with two peak velocities along the edges is predominant during the tidal cycle for simulations with $h_0 = 1$ m. In contrast, the results

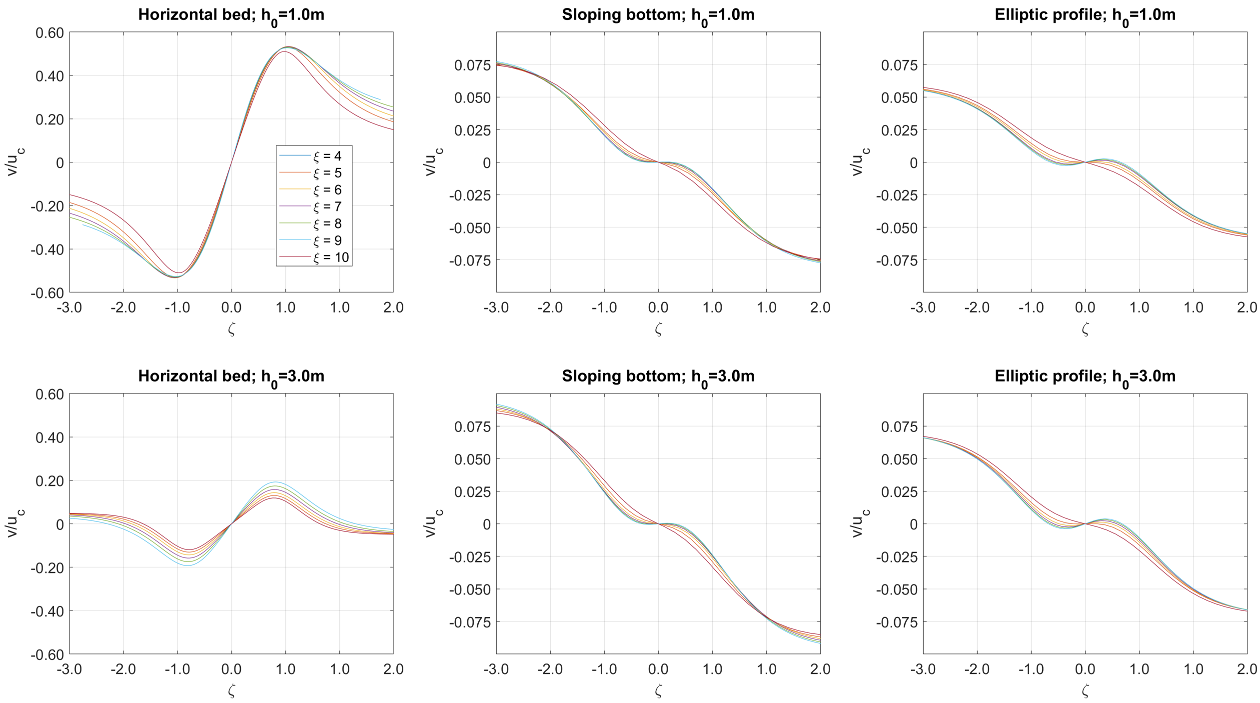

Figure 6. Non-dimensional Transverse component of the velocity at ξ =[4.0-10.0] for simulations with $W = 200$ m. The velocity is non-dimensionalized with the streamwise velocity along the axis, and the X-axis is non-dimensionalized with the half-width of the mouth width.

for $h_0 = 3$ m show a tendency towards a jet structure with a single peak velocity along the axis for the entire tidal cycle, with the exception of a short area around the mouth for low tide conditions. These results emphasise the key role of h_0 in the jet structure near the outlet.

The analysis of the evolution during a tidal cycle of the non-dimensional velocity along the axis is shown in figure 8. The velocity profiles for both nearshore profiles exhibit three distinct phases. First, there is a sharp decrease in velocity at a distance less than $\xi = 1$. Second, there is an increase in velocity and a maximum value located in a section at a distance $\xi = 1.5 - 2.0$. Third, there is a velocity decrease with decreasing ratio. Furthermore, there is a significant variation of the velocity with the tidal phase. For the cases with $h_0 = 1$ m, the maximum difference observed is $u_c/u_0 = 0.4$ at $\xi = 1.2$, which implies a variation of more than 100% between maximum and minimum values. This difference decreases further away from the outlet but maintains a value around $u_c/u_0 = 0.1$ at $\xi > 5$. Furthermore, in low tide conditions, a peak value exceeding $u_c/u_0 = 1.0$ is located downstream of the outlet, which significantly alters the predicted pattern in jet theory. This phenomenon is observed for both geometries, though it is more pronounced in the sloping case.

For $h_0 = 3$ m, lower variabilities are obtained. In addition, in this case the maximum velocity is located at the outlet; after the outlet the velocity decreases smoothly and the profiles are parallel to those of the non-tidal case. In these cases, the maximum difference $u_c/u_0 = 0.15$ is found at $\xi > 0.7$, which remains practically constant along the jet. These results show that the tide has an outstanding influence on the jet structure, with differences in u_c/u_0 above 100%. These differences, and hence the role of the tide, are particularly pronounced in shallow river mouths.

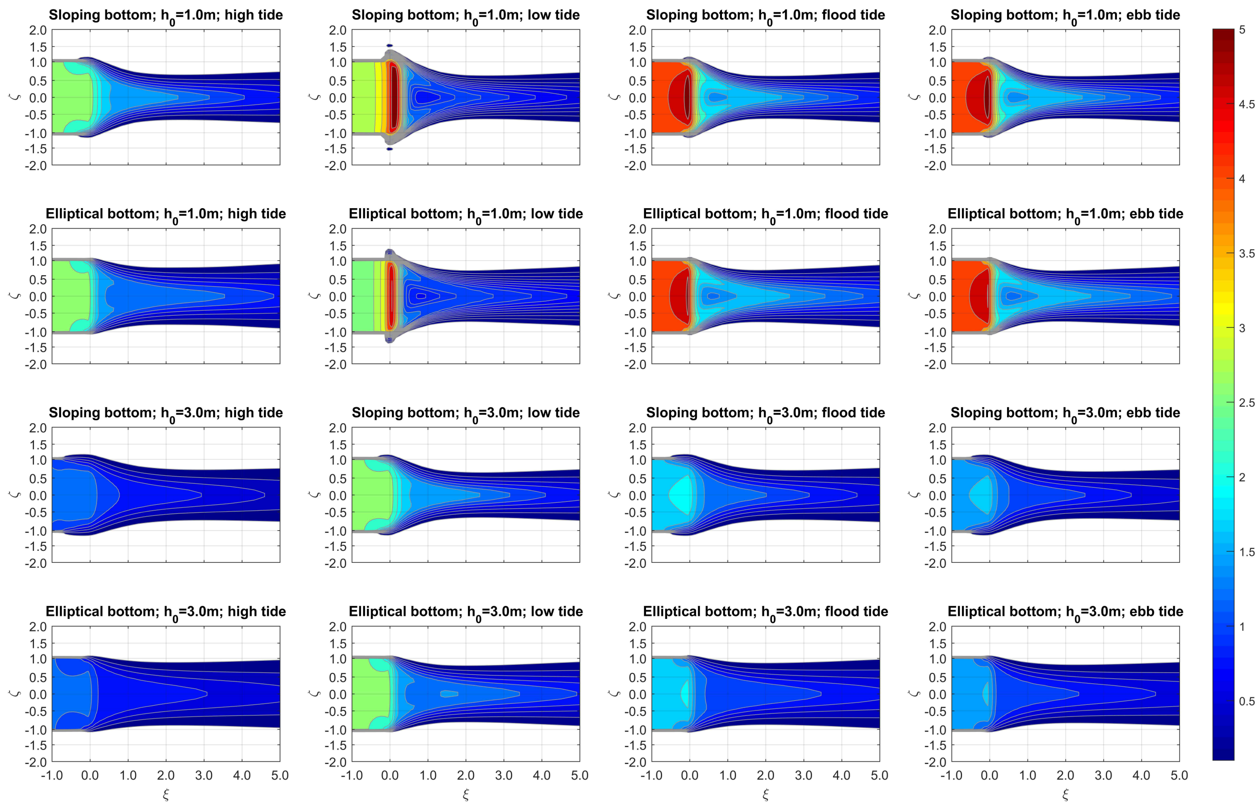

Figure 7. Streamwise velocity for Type 2 simulations at four instant during the tidal cycle: high, low, ebb and flood tide.

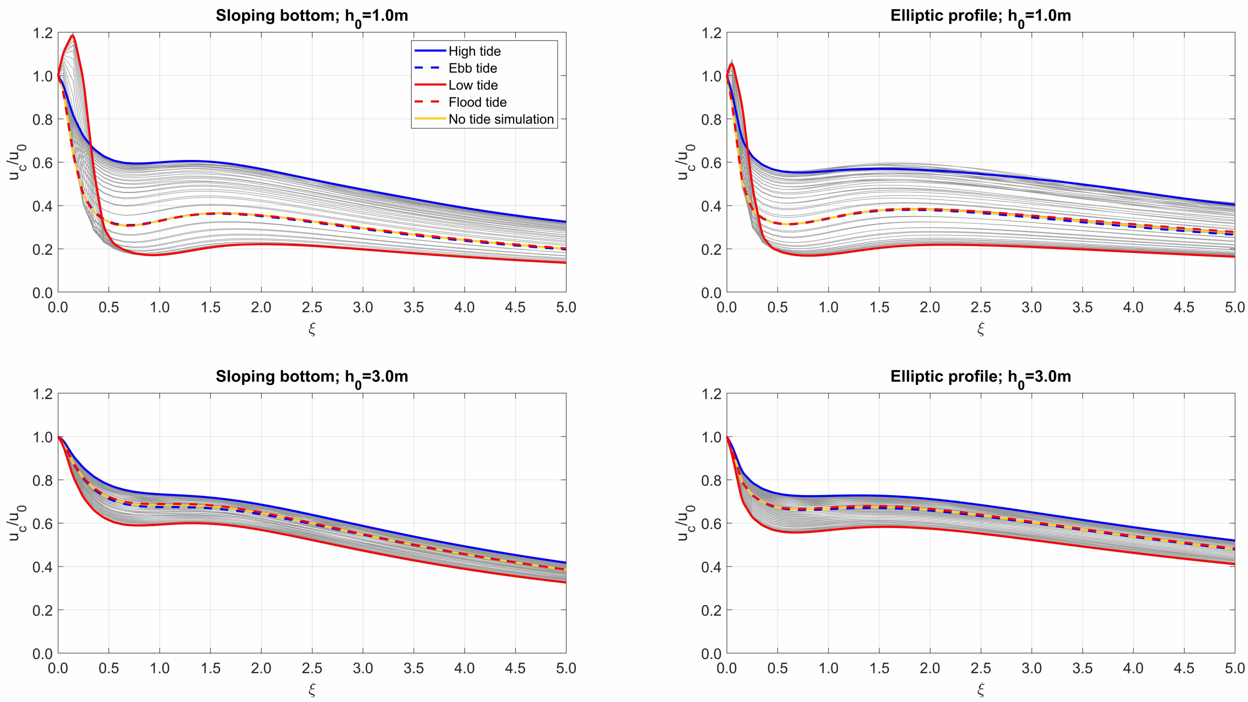

Figure 8. non-dimensional time evolution of the velocity profiles. Yellow line corresponds to the result with constant flow without sea level variation.

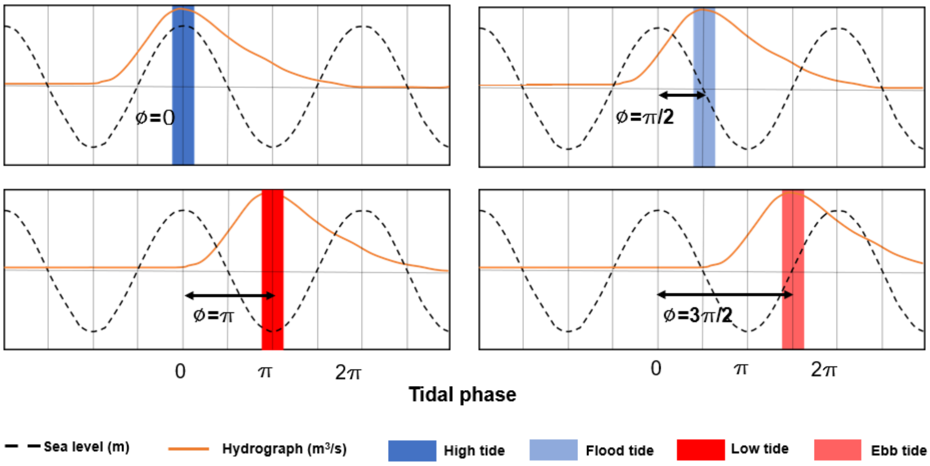

Figure 9. Definition sketch of the phase difference between the peak river discharge and the tidal level for the analysed simulations.

4.3 Transient river discharge: the role of the phase lag between the hydrograph and the tidal conditions

This section analyses the results of Type 3 simulations (table 3.3), where the geometry is restricted to the elliptical profile with $h_0 = 1$ m and $W = 200$ m. A hydrograph with a base time of 18 h and a peak discharge of 500 m^3/s is defined as the upstream boundary condition. Tidal conditions are maintained at the offshore boundary. These forcings introduce a new variable into the analysis of the jet structure: the time lag between the instant of peak discharge and high tide at the offshore boundary ϕ (figure 9). This delay is measured in terms of the phase of the tidal cycle. Analysis of the results showed that the time required for the tidal wave to propagate from the offshore boundary to the outlet is negligible.

The plan view structure of the jet during the peak discharge for the different values of ϕ is shown in figure 10. For $\phi = 0$, the jet contracts and shows a single peak velocity on the axis in close proximity to the outlet. Consequently, the velocity profile rapidly transitions to a transverse distribution with a single peak velocity on the axis. In contrast, for $\phi = \pi$, two maximum velocity peaks are clearly visible at the edges of the jet up to a distance of more than 100 m ($\xi = 0.5$). At a distance beyond this point, the velocity profile evolves to a single maximum on the axis.

These results are consistent with those presented in the previous section. At high water levels the velocity profiles show a single maximum in the centre. Conversely, in the context of low water levels, the velocity profiles show two maximum values at the edges, extending over a length of approximately $\xi = 1.0$. In the high water conditions, the water depth at the outlet (η_0) is greater, resulting in lower mean velocities at the outlet, as observed in the simulations with $h_0 = 3$ m.

To facilitate comparison with previous results, figure 11 shows the non-dimensional velocity profile along the axis. A significant variation can be observed between them, depending on the tidal conditions. When the hydrograph coincides with the high tide, η_0 is higher, leading to a lower value of the outlet velocity (u_0), resulting in velocity profiles similar to those of the jet theory, with a single maximum value at the jet axis. On the other hand, when the peak of the river discharge coincides with low tide conditions, it implies a lower depth (η_0), higher velocity at the outlet (u_0) and velocity profiles with

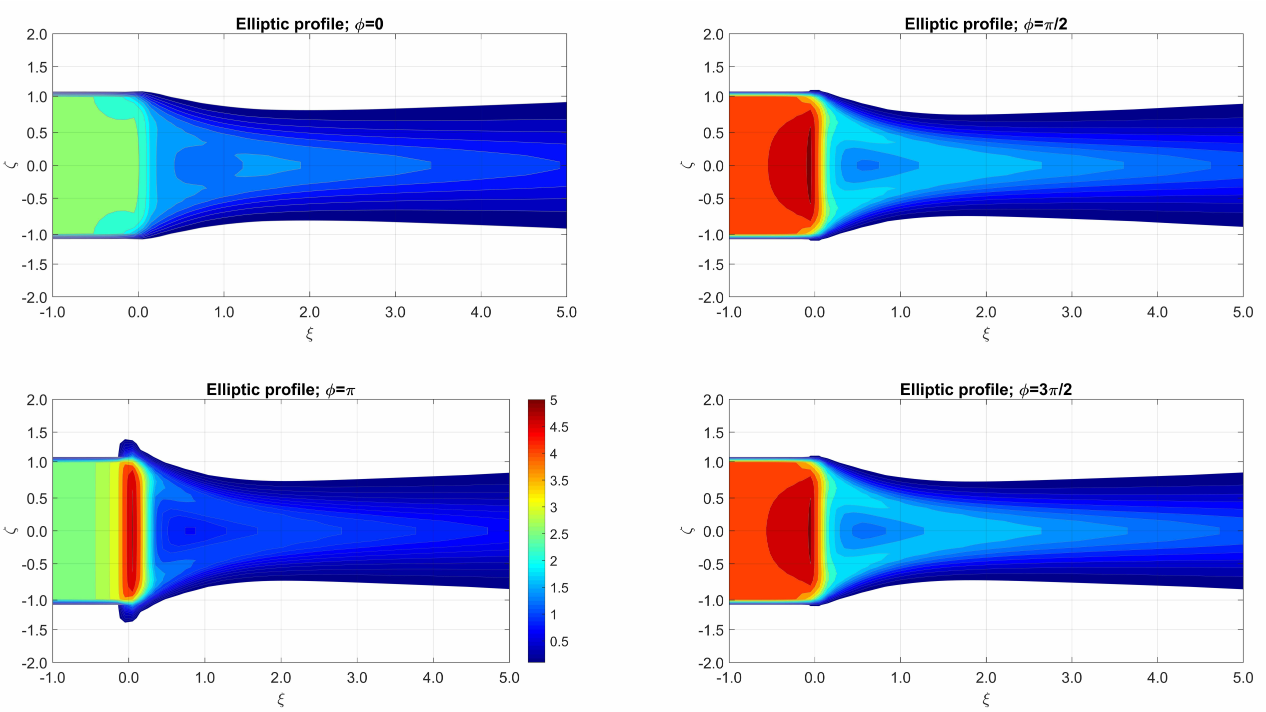

Figure 10. Streamwise velocity for $W = 200$ m, $h_0 = 1$ m, elliptical profile, and $\phi = [0, \pi/2, \pi, 3\pi/2]$ (coincidence between peak flow and high tide, low tide, ebb tide and flood tide conditions, respectively).

two peaks at the jet edges. It is also important to note that the maximum velocity is not at the outlet in every profile. In fact, it is slightly shifted towards the coast for $\phi = \pi$, especially at low tide. In these cases, the profiles are more similar to those with constant river discharge (figure 8), as they are associated with a higher velocity at the outlet. In addition, for $\phi = \pi$ there is also a second relative maximum at $\xi = 20 - 30$ associated with the advance of the river discharge.

The significant variation in the shape of the streamwise velocity profiles is also reflected in their cross-sectional distribution (figure 12). Velocity profiles with a Gaussian distribution are observed for instants corresponding to high tide, regardless of the value of ϕ, whereas two velocity peaks are observed at low tide. In contrast, there are notable differences between the velocity profiles corresponding to the simulations with hydrograph and tide compared to those with constant discharge and still water. The latter show a profile with two maximum velocity values, around 1.0 m/s. For the simulations with $\phi = 0$, all the profiles show velocity values lower than this value and none of them coincide with the case of constant discharge and still water. As for the simulations with $\phi = \pi$, the simulations with hydrograph and tide show greater similarity with those corresponding to constant discharge and still water, although a transverse distribution with more pronounced peak velocity values is observed.

5 Discussion

5.1 Boundaries defining the development of the jet

As mentioned above, jet theory describes the Zone of Flow Establishment (ZOFE) as the part of the jet where the centreline velocity remains constant until momentum dis-

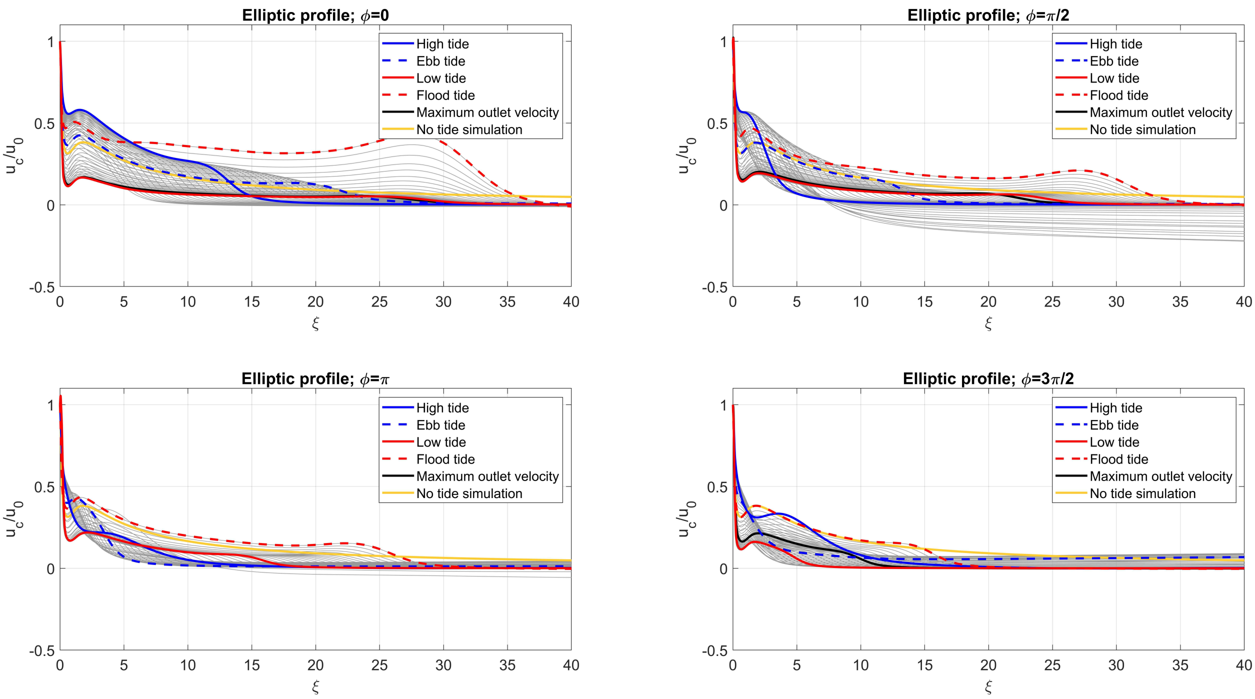

Figure 11. non-dimensional velocity along the axis during the entire tidal cycle ($\phi = [0, \pi/2, \pi, 3\pi/2]$; $W = 200m$; $h_0 = 1m$). Cases with $u_0 < 0.3$ m/s were omitted.

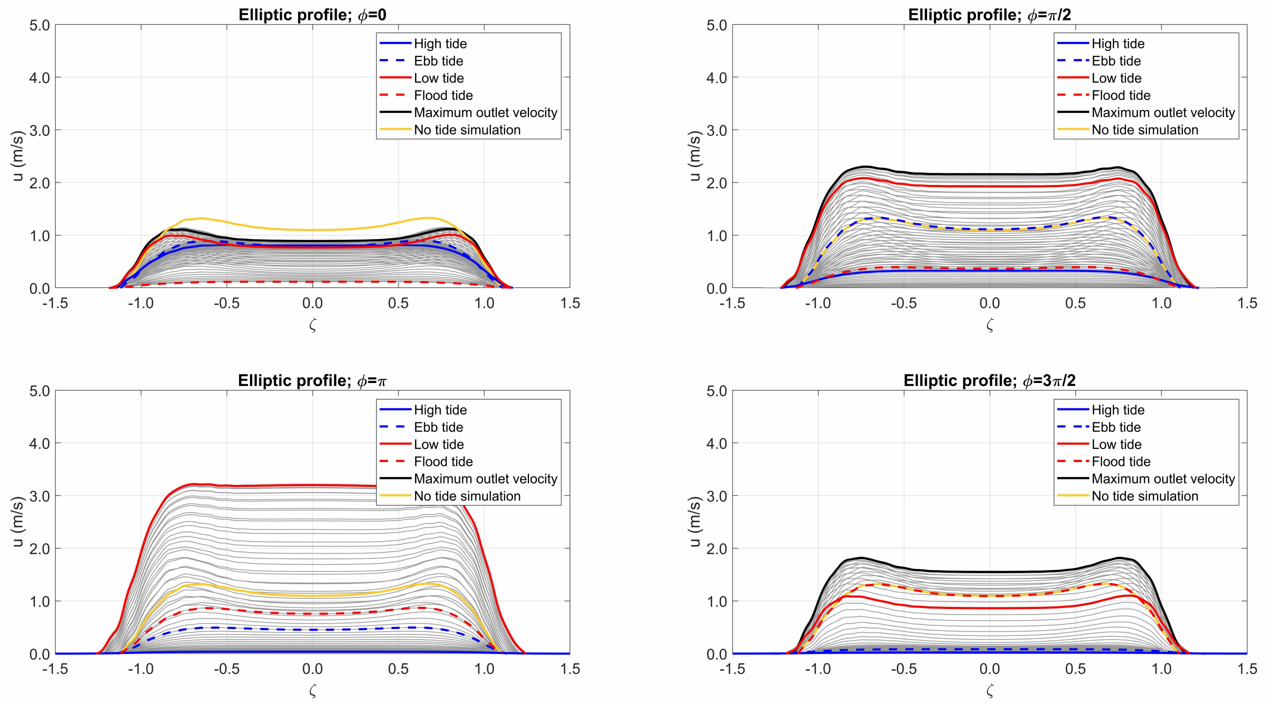

Figure 12. Cross-sectional distribution of velocities at 100 m from the outlet (ξ=0.5), located in the ZOFE region. Yellow line is added showing the result for the same geometry, corresponding to the simulation with constant discharge and still water. Black line corresponds to transverse velocity profile at the instant of maximum velocity at the outlet.

sipation and turbulence generated by edge shear reaches the entire jet (Fagherazzi et al., 2015). From this point on, the jet is dominated by turbulent eddies (Zone of Established Flow, ZOEF) and leads to a Gaussian transverse velocity distribution. According to previous works such as (Ortega-Sánchez et al., 2008), the transition from ZOFE to ZOEF does not occur at a fixed location, but take place within a transition region (ZOT) that depends on factors such as the geometry or the bottom friction. In this transition region, the velocity along the axis begins to decrease and the flow is not completely dominated by turbulence, resulting in an undefined transverse velocity profile with a clear maximum in the centre of the jet.

The analysis of the results presented in the previous section shows that the velocity along the axis does not have a constant value. Its value decreases as soon as it leaves the channel, except in certain scenarios where it is even observed to increase. It can therefore be concluded that the velocity structure of the jet at the outlet itself is in the ZOT region.

Conversely, while the theoretical structure described above is observed in some numerical experiments, the results indicate that a different jet structure can develop depending on the outlet and nearshore geometries. This structure exhibits two velocity peaks at the edge of the jet near the outlet. These two velocity peaks at the edges progress transversely towards the centre until they reach the axis, and from that point on the Gaussian profile is observed, as shown in figure 13. Therefore, the establishment of the flow is beyond this point of maximum velocity where the two peaks at the sides of the jet converge. In addition, these differences in the behaviour of the velocity distribution in the jet are amplified in the case of mouths with a greater width (W), a shallower depth at the outlet (h_0) and a sea profile different from a horizontal plane. In all these cases, the location of the relative maximum velocity along the axis was found between $\xi = 1.5-2.5$. Analogous results are observed when tides are set as the offshore boundary condition, and even when the river discharge is not constant. The velocity profile can be classified into two categories: the first category, which exhibits a single peak at the axis (related to high tide), and the second category, which exhibits two peaks at the jet edges (related to low tide). Therefore, the categorisation is dependent on the tidal conditions.

It is clear that different mouth geometries and hydrodynamic drivers lead to dissimilar jet velocity structures and turbulence progression from the edges to the jet axis, which also influences the location of the beginning of the ZOEF region. Figure 14 shows the results for the location of this initial section for the three types of simulations tested.

As summarised in Fagherazzi et al. (2015), previous works have found that for a plane unbounded jet this transition occurs at a distance of apprimately $\xi = [4.0-6.0]$. Therefore, the findings presented in this paper for horizontal geometries are in accordance with the literature, which demonstrates a considerable degree of variability for the location of the onset of the ZOEF region. The geometries analysed have a very high W/h_0 ratio, with a velocity profile influenced by the upstream section of the channel, which significantly affects the jet structure. This contrasts with the initial conditions of other studies, where the upstream section of the channel exerts a relatively minor effect on the jet structure.

Nevertheless, a comparable pattern of behaviour and tendency is observed in geometries with sloping bottoms and elliptical profiles (i.e. an increase in bottom depth along the axis). The wider mouths result in a further location of the ZOEF region in terms of non-dimensional distance, with all of them falling within the range of $\xi = [1.5-3.0]$. These distances are considerably smaller than those observed for plane unbounded jets.

Figure 14 also shows the results obtained for each time point during the tidal cycle for all simulations with constant river discharge. The parameter h_0 has a significant influence on the outcome. For $h_0 = 3$ m, the ZOEF region remains at the same distance

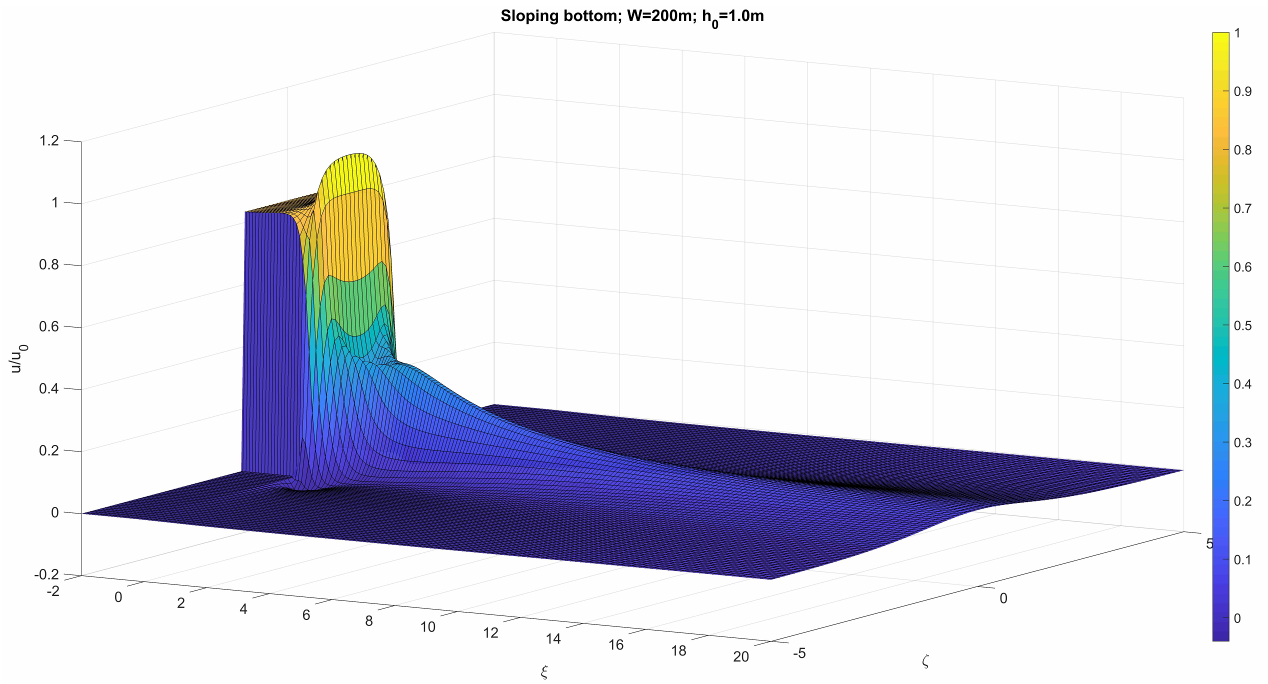

Figure 13. 3D view of the velocity distribution for the case of constant flow, W=200m, $h_0 = 1$ m, and sloping bottom profile. X-axis and Y-axis are non-dimensional distances related to the mouth half-width (b_0).

throughout the tidal cycle. However, for $h_0 = 1$ m, at low tide conditions, this distance is greater, particularly for the elliptical profile simulations. The location of the beginning is in the interval $\xi = [1.5–3.0]$. The results of the simulations with tides and transient river discharge demonstrate that at low tide conditions, the distance from the outlet where the ZOEF region is located increases. This phenomenon is more pronounced in the simulation with $\phi = \pi/2$ as this low tide coincides with the peak of the hydrograph. In the case of $\phi = 0$, two instants are observed in which the ZOEF region is located at a greater distance: the first corresponds to the peak of the hydrograph and the second to the low tide. As in the previous group of simulations, the distance for the beginning of the ZOEF region is within the interval $\xi = [1.5 - 3.0]$.

Consequently, the location of the beginning of the ZOEF region with non-horizontal geometries is located at a shorter distance from the outlet than in the cases with horizontal bottom. The reduction in the width of the mouth and the increase in the slope of the seabed in the nearshore area result in a shorter distance for the location of this transition. Conversely, a shallower outlet depth η_0 contributes to increasing this distance during a tidal cycle, with a maximum value observed during low tide conditions. Moreover, the transition and, consequently, the jet structure exhibit considerable variation throughout the tidal cycle, regardless of the outlet geometry.

5.2 Momentum balance and jet expansion/contraction

According to Wright (1977), the main depth-averaged processes that dominate the momentum balance in the spreading of river-dominated jets are: (i) inertia and momentum transport, (ii) turbulent bed friction, and (iii) acceleration due to water level variations (the barotropic term). The momentum balance for the simulations performed with constant discharge is in agreement with Wright (1977), showing that among the terms

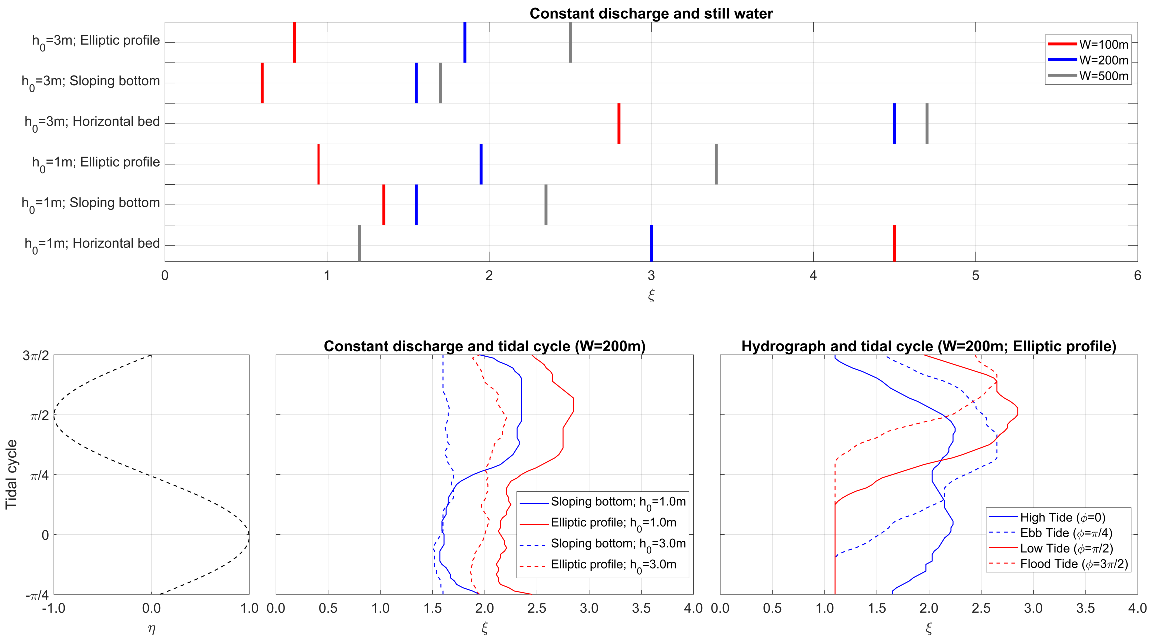

Figure 14. Analysis of the location of the onset of the ZOEF region for the three types of simulations. The top row shows a result for each simulation (Type 1) due to their independence of time. The lower row shows the results for simulations with tidal influence (Type 2 and 3). A plot of the water level in the sea region (η) during a tidal cycle is included to clarify the time at which each result is obtained. This location was determined from a comparison between the non-dimensional simulated streamwise velocity at each cross section and the ODE solutions deduced from the jet theory in the ZOEF region, ensuring that the difference between them in the interval $\zeta = [-1, 1]$ does not exceed 5%.

in equations 9 and 10, these three terms are at least one order of magnitude higher than any other. The following paragraphs are devoted to discussing the relationship between the balance of these terms and the structure of the jet.

The magnitudes of these three main momentum balance terms along the channel are illustrated in figure 15. In the vicinity of $\xi = 0$ (the outlet region), the results are similar for the sloping and elliptical profile geometries, while they show notable differences with the horizontal bed simulation. In the remaining portion of the axis, both within the canal and within the marine zone, the results tend to be similar for all geometries. With regard to the acceleration due to friction (negative values), it can be observed that its influence is limited to a reduced distance in the vicinity of the outlet for non-horizontal geometries. In contrast, it extends up to a distance of $\xi = 4.0$ ($x = 400$ m) for the geometry with a horizontal bed.

Along the flow axis, there is a balance between friction and hydrostatic pressure accelerations for each geometry. This is due to the regular and constant channel geometry, which corresponds to a uniform flow. Consequently, the acceleration due to inertial forces (momentum transport) is negligible. In the outlet area, this balance is disrupted, resulting in the emergence of significant accelerations, particularly those associated with hydrostatic pressure and inertial terms. There are notable differences in the magnitudes of these accelerations between the geometry with a horizontal bottom and those with sloping and elliptical profiles. In this region, the perturbation of the flow caused by the outfall propagates upstream as the flow is subcritical. In the nearshore area, the accelerations tend to decrease to a negligible value. The only exception to this is the acceleration due to friction for the horizontal bed geometry, which is observed to exert influence up to a distance of $\xi = 4.0$ ($x = 400$ m).

With regard to the accelerations resulting from hydrostatic pressure and momentum transport, a pronounced variation in the acceleration is concentrated in a region around the outlet in the interval $\xi = [-2.0, 1.0]$, particularly for geometries with sloping and elliptical profiles. It should be noted that the signs of the accelerations are different. Moreover, the values of these accelerations for the $h_0 = 1$ m cases are approximately one order of magnitude higher than those obtained for the $h_0 = 3$ m simulations. Consequently, for the horizontal bed geometries, friction plays a dominant role over a longer extent in the nearshore, promoting jet expansion, in a manner analogous to the friction-dominated flows described by Wright (1977). Conversely, in the case of variable bed level geometries, the barotropic and momentum transport terms exert a dominant influence on the momentum balance in the vicinity of the outlet, resulting in the contraction of the jet. At approximately $\xi = 1.0$, the balance between barotropic and momentum transport is no longer maintained, resulting in the cessation of jet contraction.

5.3 Jet structure and the development of lateral levees

The jet structure plays an important role in the morphodynamic evolution of river mouths and the development of bars, both at short-term (Ruiz-Reina & López-Ruiz, 2021) and long-term (Jiménez-Robles et al., 2016) scales. The changes in the initial bed geometry would, in a feedback process, alter the jet structure and, consequently, the hydrodynamics of the river mouth. Nevertheless, the findings presented in this work provide some insights that can be employed to establish links with morphodynamic analyses.

For instance, it was observed that the width of the mouth exerts a clear influence on the transverse profile of the flow velocity, which favours the formation of two peaks of maximum velocity at the edges. This phenomenon is more pronounced in cases where the bottom depth at the outlet is shallower ($h_0 = 1$ m). Both Ruiz-Reina and López-Ruiz (2021) and Jiménez-Robles et al. (2016) observed the formation of lateral levees parallel to the channel walls for river mouths with channel widths similar to those consid-

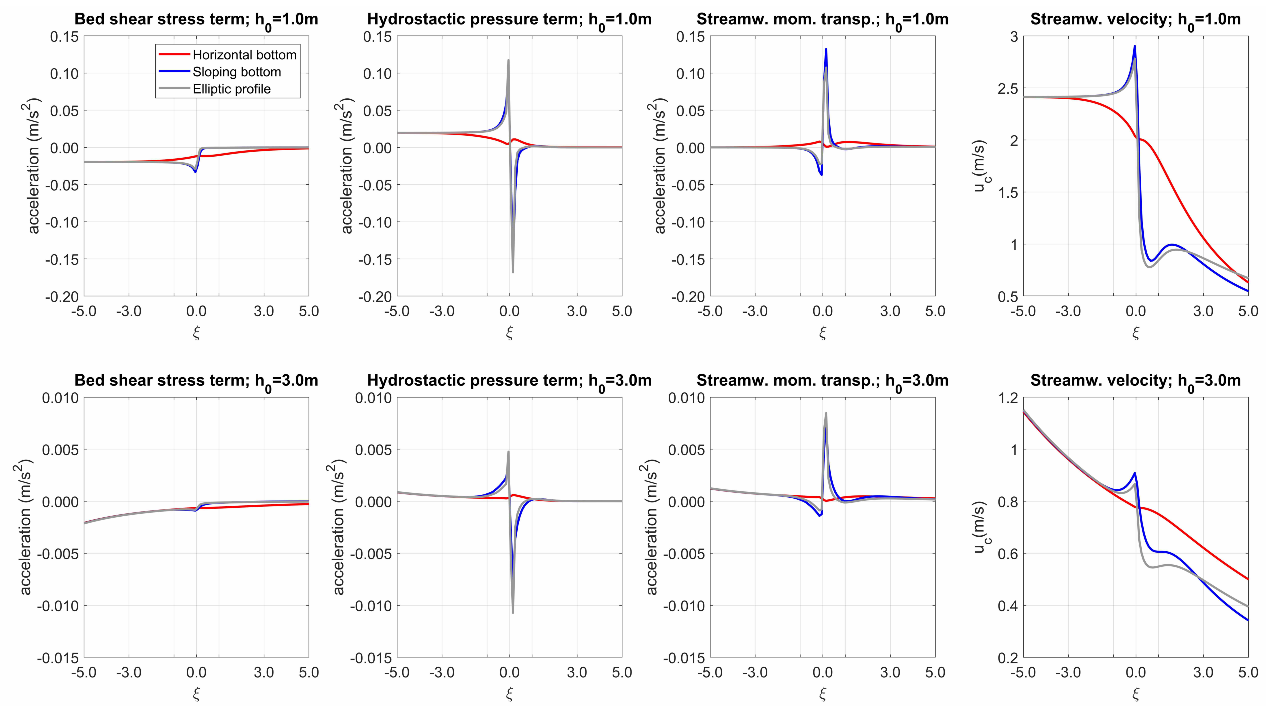

Figure 15. Results obtained for each of the momentum equation terms for the simulation with constant flow, $W = 200m$ and h_0=[1m,3m]: acceleration due to streamwise momentum transport, (inertial term) hydrostatic pressure and bed shear in bottom layer. Each line is associated with a geometry type.In the last column, the result for the streamwise velocity along the axis is added for a better understanding.

ered in this study. This morphodynamic evolution implies a lower bottom depth up to a certain point of the bar, after which a pronounced slope is formed where the levees do not develop. In the case of the simulations presented in the work by Ruiz-Reina and López-Ruiz (2021), the bottom depth reaches values below 2.0 m. On the other hand, the levees are more clearly shown in the simulations where the peak of the hydrograph coincides with the low tide, which implies a higher value of the velocity at the outlet, u_0, in agreement with the results obtained in the present work.

6 Conclusions

The objective of this study was twofold: (1) to analyse the role of mouth and nearshore geometries on the jet structure of river mouths; and (2) to assess the influence of tidal and river discharge conditions on this jet structure. The application of a process-based numerical model to idealised geometries defined with realistic parameters enabled the effect of mouth dimensions and nearshore profile shape to be analysed separately, and the role of river discharge and tidal conditions to be unravelled. The results of the numerical model for simplified geometries were compared with the jet theory solutions obtained by Abramovich and Schindel (1963); Özsoy and Ünlüata (1982), demonstrating that the model accurately reproduces the jet structure. This makes it a highly valuable tool for the analysis of more complex geometries and the effect of time-varying forcings.

Simulations with a constant river discharge and water level demonstrated that the outlet geometry determines the jet structure. In particular, outlets with shallower and wider cross-sections exhibited two velocity peaks at the edges of the jet, in contrast to the single maximum observed in the centre. In outlets where the nearshore profile is horizontal, the beginning of the ZOEF region is located at a greater distance from the outlet, and the jet expands after leaving the outlet. In contrast, for non-horizontal geometries, the jet initially contracts. Furthermore, the hydrodynamics at the mouth are evidently dominated by friction for this horizontal nearshore geometry. However, for sloping and elliptical profiles, the role of inertial and barotropic accelerations is significantly increased in the vicinity of the outlet.

It is observed that the changes in velocity during the tidal cycle may reach up to 100% between extreme values, while the variability of the jet structure during the tidal cycle is also significant when transient river discharges are included. This variability limits the applicability of the analyses carried out for stationary conditions in tidal environments or with a variable hydrological regime. This variability results in a significant variation in the location of the beginning of the ZOEF region. This is dependent on the time lag between the peak of the hydrograph and the tidal conditions. Moreover, the phase of the tidal cycle and the duration of the tidal cycle also determine the geometry of the transverse velocity profile. During low tide conditions, the distance from the outlet to the beginning of the ZOEF region increases, and the velocity profile tends towards a profile with two lateral velocity peaks. During high tide conditions, a shorter distance up to this beginning of the ZOEF region and a velocity profile with a single maximum on the axis is observed. This is consistent with the findings of previous studies on bar formation in analogous river mouths. The results achieved in this study enhance our comprehension of the jet structure in river mouths, providing insights into the complexity of the river-ocean interaction during extreme events and its impact on the morphodynamic evolution of river mouth bars and deltas.

Data availability statement

The model input files are available at the Zenodo repository: `https://zenodo.org/records/11546317`. Delft3D source codes are downloadable from the Deltares model repository (`https://oss.deltares.nl/web/delft3d`).

Acknowledgments

This work has been supported by the Spanish Ministry of Economy and Competitiveness. Grant PID2021-125895OA-I00 (project RESILIENCE) funded by MCIN/AEI/ 10.13039/501100011033 and by ERDF "A way of making Europe".

References

Abramovich, G., & Schindel, L. (1963). *The theory of turbulent jets.* MIT-Press.

Anthony, E. J., Marriner, N., & Morhange, C. (2014). Human influence and the changing geomorphology of Mediterranean deltas and coasts over the last 6000 years: From progradation to destruction phase? *Earth-Science Reviews*, *139*, 336–361. doi: 10.1016/j.earscirev.2014.10.003

Besset, M., Anthony, E. J., & Bouchette, F. (2019). Multi-decadal variations in delta shorelines and their relationship to river sediment supply: An assessment and review. *Earth-Science Reviews*, *193*(March), 199–219. doi: 10.1016/j.earscirev.2019.04.018

Boudet, L., Sabatier, F., & Radakovitch, O. (2017). Modelling of sediment transport pattern in the mouth of the Rhone delta: Role of storm and flood events. *Estuarine, Coastal and Shelf Science*, *198*, 568–582. doi: 10.1016/j.ecss.2016.10.004

Canestrelli, A., Nardin, W., Edmonds, D., Fagherazzi, S., & Slingerland, R. (2014, dec). Importance of frictional effects and jet instability on the morphodynamics of river mouth bars and levees. *Journal of Geophysical Research: Oceans*, *119*(1), 509–522.

Chow, V. T., Maidment, D., & Mays, L. (1988). *Applied hydrology.* McGraw-Hill.

Dean, R., & Dalrymple, R. (2004). *Coastal processes with engineering applications.* Cambridge University Press.

Edmonds, D. A., & Slingerland, R. L. (2007, jun). Mechanics of river mouth bar formation: Implications for the morphodynamics of delta distributary networks. *Journal of Geophysical Research*, *112*(F2), F02034. doi: 10.1029/2006JF000574

Fagherazzi, S., Edmonds, D. A., Nardin, W., Leonardi, N., Canestrelli, A., Falcini, F., ... Slingerland, R. L. (2015). Dynamics of river mouth deposits. *Reviews of Geophysics*, *53*, 642-672. doi: 10.1002/2014RG000451

Fan, H., Huang, H., Zeng, T. Q., & Wang, K. (2006). River mouth bar formation, riverbed aggradation and channel migration in the modern Huanghe (Yellow) River delta, China. *Geomorphology*, *74*(1), 124-136. Retrieved from `https://www.sciencedirect.com/science/article/pii/S0169555X0500293X` doi: https://doi.org/10.1016/j.geomorph.2005.08.015

Fernandino, G., Elliff, C. I., & Silva, I. R. (2018). Ecosystem-based management of coastal zones in face of climate change impacts: Challenges and inequalities. *Journal of Environmental Management*, *215*, 32–39. Retrieved from `https://doi.org/10.1016/j.jenvman.2018.03.034` doi: 10.1016/j.jenvman.2018.03.034

Gao, W., Shao, D., Wang, Z. B., Nardin, W., Rajput, P., Yang, W., ... Cui, B. (2019). Long-term Cumulative Effects of Intra-annual Variability of Unsteady River Discharge on the Progradation of Delta Lobes: A Modeling Perspective. *Journal of Geophysical Research: Earth Surface*, 1–14. doi: 10.1029/2017JF004584

Giger, M., Dracos, T., & Jirka, G. H. (1991). Entraînement et mélange dans des jets plans turbulents en faible profondeur d'eau. *Journal of Hydraulic Research*, *29*, 615-642. doi: 10.1080/00221689109498980

Jiménez-Robles, A. M., & Ortega-Sánchez, M. (2018). Implications of River Discharge Angle and Basin Slope on Mouth Bar Morphology and Discharge Dynamics of Stable Jets. *Journal of Hydraulic Engineering*, *144*(9), 1–9. doi:

10.1061/(ASCE)HY.1943-7900.0001506

Jiménez-Robles, A. M., Ortega-Sánchez, M., & Losada, M. A. (2016). Effects of basin bottom slope on jet hydrodynamics and river mouth bar formation. *Journal of Geophysical Research: Earth Surface*, *121*(6), 1110–1133. doi: 10.1002/2016JF003871

Jirka, G. H., & Giger, M. (1992). Plane turbulent jets in a bounded fluid layer. *Journal of Fluid Mechanics*, *241*, 587-614. doi: 10.1017/S0022112092002167

Lamb, M. P., Nittrouer, J. A., Mohrig, D., & Shaw, J. (2012). Backwater and river plume controls on scour upstream of river mouths: Implications for fluvio-deltaic morphodynamics. *Journal of Geophysical Research: Earth Surface*, *117*(1), 1–16.

Leonardi, N., Canestrelli, A., Sun, T., & Fagherazzi, S. (2013). Effect of tides on mouth bar morphology and hydrodynamics. *Journal of Geophysical Research: Oceans*, *118*, 4169-4183. doi: 10.1002/jgrc.20302

Leonardi, N., Kolker, A. S., & Fagherazzi, S. (2015). Interplay between river discharge and tides in a delta distributary. *Advances in Water Resources*, *80*, 69–78. doi: 10.1016/j.advwatres.2015.03.005

Lera, S., Nardin, W., Sanford, L., Palinkas, C., & Guercio, R. (2019). The impact of submersed aquatic vegetation on the development of river mouth bars. *Earth Surface Processes and Landforms*, *1506*(February), 1494–1506. doi: 10.1002/esp.4585

Lesser, G., Roelvink, J., Van Kester, J., & Stelling, G. (2004, October). Development and validation of a three-dimensional morphological model. *Coastal Engineering*, *51*(8-9), 883–915.

Nardin, W., Edmonds, D. A., & Fagherazzi, S. (2016). Influence of vegetation on spatial patterns of sediment deposition in deltaic islands during flood. *Advances in Water Resources*, *93*, 236–248. doi: 10.1016/j.advwatres.2016.01.001

Nardin, W., & Fagherazzi, S. (2012). The effect of wind waves on the development of river mouth bars. *Geophysical Research Letters*, *39*(12), 1–6.

Nardin, W., Mariotti, G., Edmonds, D. A., Guercio, R., & Fagherazzi, S. (2013, jun). Growth of river mouth bars in sheltered bays in the presence of frontal waves. *Journal of Geophysical Research: Earth Surface*, *118*(2), 872–886.

Nienhuis, J. H., Ashton, A. D., Nardin, W., Fagherazzi, S., & Giosan, L. (2016). Alongshore sediment bypassing as a control on river mouth morphodynamics. *Journal of Geophical Research: Earth Surface*, *121*, 664–683.

Ortega-Sánchez, M., Losada, M. A. A., & Baquerizo, A. (2008). A global model of a tidal jet including the effects of friction and bottom slope. *Journal of Hydraulic Research*, *46*, 80-86.

Özsoy, E., & Ünlüata, Ü. (1982). Ebb-tidal flow characteristics near inlets. *Estuarine, Coastal and Shelf Science*, *14*(3). doi: 10.1016/S0302-3524(82)80015-7

Roelvink, D., & Walstra, D.-J. (2004). Keeping It Simple By Using Complex Models. *Advances in Hydro-Science and Engineering*, *VI*(August), 1–11.

Romero-Martín, R., Caballero-Leiva, I., Llasat, M. C., Llasat-Botija, M., Rigo, T., Valdemoro, H. I., … Jiménez, J. A. (2024, 12). Mapping cumulative compound hydrometeorological and marine-induced risks on the nw mediterranean coast. *Scientific Reports*, *14*. doi: 10.1038/s41598-024-53899-z

Rowland, J. C., Dietrich, W. E., & Stacey, M. T. (2010). Morphodynamics of subaqueous levee formation: Insights into river mouth morphologies arising from experiments. *Journal of Geophysical Research: Earth Surface*, *115*(4), 1–20. doi: 10.1029/2010JF001684

Ruiz-Reina, A. (2021, February). *River mouth data from major streams in southern Spain.* https://doi.org/10.5281/zenodo.4541878. Zenodo. Retrieved from `https://doi.org/10.5281/zenodo.4541878` doi: 10.5281/zenodo.4541878

Ruiz-Reina, A., & López-Ruiz, A. (2021). Short-term river mouth bar development during extreme river discharge events: The role of the phase difference between the peak discharge and the tidal level. *Coastal Engineering*, *170*(August), 103982. Retrieved from https://doi.org/10.1016/j.coastaleng.2021.103982 doi: 10.1016/j.coastaleng.2021.103982

Ruiz-Reina, A., Zarzuelo, C., López-Herrera, J. M., & López-Ruiz, A. (2020). The marine-fluvial frontier at river mouths during extreme events: A hydrodynamic approach. *Journal of Coastal Research*, *95*(sp1), 1525 – 1530. doi: 10.2112/SI95-294.1

van de Lageweg, W. I., & Feldman, H. (2018). Process-based modelling of morphodynamics and bar architecture in confined basins with fluvial and tidal currents. *Marine Geology*, *398*, 35-47. Retrieved from https://doi.org/10.1016/j.margeo.2018.01.002 doi: 10.1016/j.margeo.2018.01.002

Wright, L. D. (1977). Sediment transport and deposition at river mouths : A synthesis sediment transport and deposition at river mouths : A synthesis. *Geological Society of America Bulletin*, *88*, 857-868. doi: 10.1130/0016-7606(1977)88⟨857

Supporting Information for "River mouth hydrodynamics: the role of the outlet geometry and transient tidal and river discharge conditions on the jet structure"

Antonio Ruiz-Reina[1], Alejandro López-Ruiz[1], Miguel Ortega-Sánchez[2]

[1]Departamento de Ingeniería Aeroespacial y Mecánica de Fluidos, Universidad de Sevilla, Camino de los Descubrimientos s/n, 41092, Seville, Spain

[2]Andalusian Institute for Earth System Research, University of Granada, Avda. del Mediterráneo, s/n, 18006, Granada, Spain

Numerical solution of the Özsoy and Ünlüata equations for the turbulent jet theory

The numerical solution for the turbulent jet theory in the ZOEF region was obtained using a simple finite difference scheme for the ODE system defined by equations 6 and 7 of the manuscript. If the nondimensional along channel coordinate ξ is discretised into $i = 1, 2, ...N$ points equally spaced by the distance $\Delta\xi$, the use of an explicit forward difference for ξ reads as follows:

$$U_{i+1}B_{i+1} = \frac{1}{I_1 H_{i+1}} \left(I_1 H_i U_i B_i + a\Delta\xi H_i U_i \right) \tag{1}$$

$$U_{i+1}^2 B_{i+1} = \frac{1}{H_{i+1}} \left(H_i U_i^2 B_i - \mu\Delta\xi B_i U_i^2 \right) \tag{2}$$

Equations 1 and 2 define a system of two equations with U_{i+1} and B_{i+1} as unknowns, which can be solved at any point along the jet axis using $U_{i=1} = 1$ and $B_{i=1} = 1$ as boundary conditions at the outlet $x = 0$.

To validate this numerical scheme, the results for simple geometries (horizontal and sloping beds) were compared with the analytical solutions obtained by Özsoy and Ünlüata (1982), who obtained the following expression for $U(\xi)$ along the ZOEF using the functions $J(\xi)$ and $L(\xi)$:

$$J(\xi) = \exp\left(-\mu \int_0^{\xi} \frac{d\xi'}{H(\xi')}\right) \tag{3}$$

$$L(\xi) = \frac{2aI_2}{I_1} \int_{\xi_s}^{\xi} H(\xi')J(\xi')d\xi' + J^2(\xi_s) \tag{4}$$

$$U(\xi) = J(\xi)L(\xi)^{-1/2} \tag{5}$$

being $\xi_s = x_s/b_0$. The solution for an horizontal bed ($H = 1$) is Özsoy and Ünlüata (1982):

$$U(\xi) = e^{-\mu\xi}\left[e^{-2\mu\xi_s} + \frac{2aI_2}{\mu I_1}\left(e^{-\mu\xi_s} - e^{-\mu\xi}\right)\right]^{-1/2} \tag{6}$$

For a sloping bottom with constant slope m, considering $H = 1 + \nu\xi$ and $\nu = mb_0/h_0$, the solution is:

$$U(\xi) = H^{-\mu/\nu}\left[H_s^{-2\mu/\nu} + \frac{2aI_2}{I_1\left(2 - \mu/\nu\right)}\left(H^{2-\mu/\nu} - H_s^{2-\mu/\nu}\right)\right]^{-1/2} \tag{7}$$

Figure S1 compares the results for the two proposed geometries for which the analytical solution is known: i) horizontal bed; ii) flat bed with a slope of m =0.05 and iii) bed with an elliptical profile, for which only the numerical solution is shown. For these calculations the following parameters were used: C_z=55; h_0=1 m; a=0.05, which are realistic values. A good fit is observed for the horizontal bed case as well as for the sloped bottom case, although the latter gives maximum differences around 20% for ξ =9.0, which are considered acceptable since they are punctual. Thus, from this theoretical basis and with the support of the numerical resolution of the three proposed cases, a solution derived from the jet theory is available to compare the results of the simulations carried out throughout the manuscript.

References

Özsoy, E., & Ünlüata, Ü. (1982). Ebb-tidal flow characteristics near inlets. *Estuarine, Coastal and Shelf Science*, *14*(3). doi: 10.1016/S0302-3524(82)80015-7

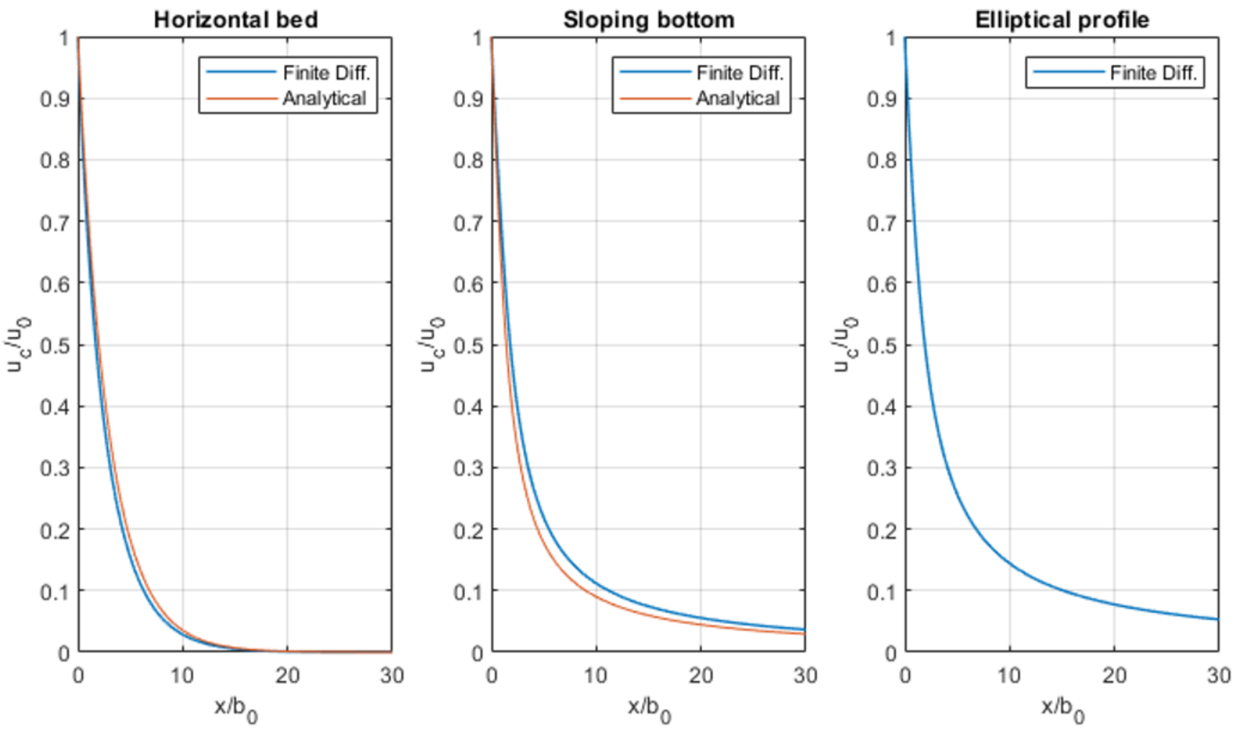

Figure S1. Dimensionless solutions for the streamwise velocity of a bounded jet along the axis (u_c) for horizontal, sloping bottom and elliptical profiles (from left to right) obtained with the analytical and numerical solutions derived from the solution of the jet theory ODE equations (orange and blue lines, respectively).